

ISSN:2349-6495(P) | 2456-1908 (O)



# International Journal of Advanced Engineering Research and Science

(IJAERS)

An Open Access Peer-Reviewed International Journal



Journal DOI: 10.22161/ijaers

Issue DOI: 10.22161/ijaers.111

AI PUBLICATIONS

Vol.- 11 | Issue - 1 | Jan 2024

editor.ijaers@gmail.com | editor@ijaers.com | <https://www.ijaers.com/>

# International Journal of Advanced Engineering Research and Science (IJAERS)

(ISSN: 2349-6495(P)| 2456-1908(O))

DOI: 10.22161/ijaers

Vol-11, Issue-1

January, 2024

*Editor in Chief*

Dr. Swapnesh Taterh

*Chief Executive Editor*

S. Suman Rajest

---

Copyright © 2024 International Journal of Advanced Engineering Research and Science

Publisher

*AI Publication*

Email: [editor.ijaers@gmail.com](mailto:editor.ijaers@gmail.com); [editor@ijaers.com](mailto:editor@ijaers.com)

Web: [www.ijaers.com](http://www.ijaers.com)

## **International Editorial/ Reviewer Board**

### **Editor in Chief**

- **Dr. Swapnesh Taterh (Chief-Editor)**, Amity University, Jaipur, India

### **Chief Executive Editor**

- **S. Suman Rajest**, Vels Institute of Science, Technology & Advanced Studies, India  
chief-executive-editor@ijaers.com

### **Associate Editors**

- **Dr. Ram Karan Singh**, King Khalid University, Guraiger, Abha 62529, Saudi Arabia
- **Dr. Shuai Li**, University of Cambridge, England, Great Britain









### **Editorial Member**

- **Behrouz Takabi**, PhD, Texas A&M University, Texas, USA
- **Dr. Gamal Abd El-Nasser Ahmed Mohamed Said**, Port Training Institute (PTI), Arab Academy For Science, Technology and Maritime Transport, Egypt
- **Dr. Hou, Cheng-I**, Chung Hua University, Hsinchu Taiwan
- **Dr. Ebrahim Nohani**, Islamic Azad University, Dezful, IRAN.
- **Dr. Ahmadad Nabih Zaki Rashed**, Menoufia University, EGYPT
- **Dr. Rabindra Kayastha**, Kathmandu University, Nepal
- **Dr. Dinh Tran Ngoc Huy**, Banking and Finance, HCM, Viet Nam
- **Dr. Engin NAS**, Duzce University, Turkey
- **Dr. A. Heidari**, California South University (CSU), Irvine, California, USA
- **Dr. Uma Choudhary**, Mody University, Lakshmangarh, India
- **Dr. Varun Gupta**, National Informatic Center, Delhi, India
- **Dr. Ahmed Kadhim Hussein**, University of Babylon, Republic of Iraq
- **Dr. Vibhash Yadav**, Rajkiya Engineering College, Banda. UP, India
- **Dr. M. Kannan**, SCSVMV University, Kanchipuram, Tamil Nadu, India
- **José G. Vargas-Hernández**, University of Guadalajara Periférico Norte 799 Edif. G201-7, Núcleo Universitario Los Belenes, Zapopan, Jalisco, 45100, México
- **Dr. Sambit Kumar Mishra**, Gandhi Institute for Education and Technology, Baniatangi, Bhubaneswar, India
- **DR. C. M. Velu**, Datta Kala Group of Institutions, Pune, India
- **Dr. Deependra Pandey**, Amity University, Uttar Pradesh, India
- **Dr. K Ashok Reddy**, MLR Institute of Technology, Dundigal, Hyderabad, India
- **Dr. S.R.Boselin Prabhu**, SVS College of Engineering, Coimbatore, India
- **N. Balakumar**, Tamilnadu College of Engineering, Karumathampatti, Coimbatore, India
- **R. Poorvadevi**, SCSVMV University, Enathur, Kanchipuram, Tamil Nadu, India
- **Dr. Subha Ganguly**, Arawali Veterinary College, Sikar, India
- **Dr. P. Murali Krishna Prasad**, GVP College of Engineering for Women, Visakhapatnam, Andhra Pradesh, India
- **Anshul Singhal**, Bio Instrumentation Lab, MIT, USA
- **Mr. Lusekelo Kibona**, Ruaha Catholic University, Iringa, Tanzania
- **Sina Mahdavi**, Urmia Graduate Institute, Urmia, Iran
- **Dr. N. S. Mohan**, Manipal Institute of Technology, Manipal, India
- **Dr. Zafer Omer Ozdemir**, University of Health Sciences, Haydarpara, Uskudar, Istanbul, TURKIYE
- **Bingxu Wang**, 2721 Patrick Henry St Apt 510, Auburn Hills, Michigan, United States

- **Dr. Jayashree Patil-Dake**, KPB Hinduja College of Commerce, Mumbai, India
- **Dr. Neel Kamal Purohit**, S.S. Jain Subodh P.G. College, Rambagh, Jaipur, India
- **Mohd Muntjir**, Taif University, Kingdom of Saudi Arabia
- **Xian Ming Meng**, China Automotive Technology & Research Center No.68, East Xianfeng Road, Dongli District, Tianjin, China
- **Herlandi de Souza Andrade**, FATEC Guaratingueta, State Center for Technological Education Paula Souza - CEETEPS
- **Dr. Payal Chadha**, University of Maryland University College Europe, Kuwait
- **Ahmed Moustafa Abd El-hamid Elmahalawy**, Menoufia University, Al Minufya, Egypt
- **Prof. Mark H. Rummeli**, University & Head of the characterisation center, Soochow Institute for Energy Materials Innovations (SIEMES), Suzhou, Jiangsu Province, China
- **Dr. Eman Yaser Daraghmi**, Ptuk, Tulkarm, Palestine
- **Holmes Rajagukguk**, State University of Medan, Lecturer in Sisingamangaraja University North Tapanuli, Indonesia
- **Dr. Menderes KAM**, Dr. Engin PAK Cumayeri Vocational School, DÜZCE UNIVERSITY (University in Turkey), Turkey
- **Dr. Jatin Goyal**, Punjabi University, Patiala, Punjab, India | International Collaborator of GEITEC / UNIR / CNPq, Brazil
- **Ahmet İPEKÇİ**, Dr. Engin PAK Cumayeri Vocational School, DÜZCE UNIVERSITY, Turkey
- **Baarimah Abdullah Omar**, Universiti Malaysia Pahang (UMP), Gambang, 26300, Malaysia
- **Sabri UZUNER**, Dr. Engin PAK Cumayeri Vocational School Cumayeri/Duzce/Turkey
- **Ümit AĞBULUT**, Düzce University, Turkey
- **Dr. Mustafa ÖZKAN**, Trakya University, Edirne/ TURKEY
- **Dr. Indrani Bhattacharyya**, Dr. B.C. Roy College of Pharmacy and Allied Health Sciences, Durgapur, West Bengal, India
- **Egnon Kouakouc**, Nutrition/Health at University Felix Houphouet Boigny Abidjan, Ivory Coast
- **Dr. Suat SARIDEMİR**, Düzce University, Faculty of Technology, Turkey
- **Dr. Manvinder Singh Pahwa**, Director, Alumni Relations at Manipal University Jaipur, India
- **Omid Habibzadeh Bigdarvish**, University of Texas at Arlington, Texas, USA
- **Professor Dr. Ho Soon Min**, INTI International University, Jln BBN 12/1, Bandar, Baru Nilai, 71800 Negeri Sembilan, Malaysia
- **Ahmed Mohammed Morsy Hassan**, South Egypt Cancer Institute, Assiut University, Assiut, Egypt
- **Xian Ming Meng (Ph.D)**, China Automotive Technology & Research Center, No.68, East Xianfeng Road, Tianjin, China
- **Ömer Erkan**, Konuralp Campus, Düzce-Turkey
- **Dr. Yousef Daradkeh**, Prince Sattam bin Abdulaziz University) PSAU), KSA
- **Peter JO**, IPB University, Indonesia
- **Nazmi Liana Binti Azmi**, Raja Perempuan Zainab II Hospital, 15586 Kota Bharu, Kelantan, Malaysia
- **Mr. Sagar Jamle**, Oriental University, Indore, India
- **Professor Grazione de Souza**, Applied Mathematics, Rio de Janeiro State University, Brazil
- **Kim Edward S. Santos**, Nueva Ecija University of Science and Technology, Philippines.

# Vol-11, Issue-1, January 2024

(10.22161/ijaers.111)

| <b>Detail with DOI (CrossRef)</b>   |                  |
|---|------------------|
| <b><i>Fabrication of pure porous CuO from microwave-synthesized MOF-199 by calcination in ambient air</i></b><br>Nam Ho Phung Khac<br> DOI: <a href="https://doi.org/10.22161/ijaers.11.1">10.22161/ijaers.11.1</a>  | Page No: 001-006 |
| <b><i>Performance Evaluation of Neural Networks in Road Sign Recognition</i></b><br>Sanjit Kumar Saha<br> DOI: <a href="https://doi.org/10.22161/ijaers.11.2">10.22161/ijaers.11.2</a>   | Page No: 007-012 |
| <b><i>Computational analysis of the transition of a system between two non-equilibrium stationary states through two-dimensional laminar natural convection in a cylindrical cavity</i></b><br>Herimiah Rakotondranja Stelarijao Eloi, Raminosoa Andrianary Lala, Ramanantsoa Ravo Mparany, Randrianandraina Hery Zo, Rakotomalala Minoson, Razafinjato Victor Albert<br> DOI: <a href="https://doi.org/10.22161/ijaers.11.3">10.22161/ijaers.11.3</a> | Page No: 013-017 |
| <b><i>Particle Swarm Algorithm Applied to Image Reconstruction on Multiphase Flows</i></b><br>B. C. B. N. Souza, R. A. M. Junior, M. G. Nascimento, C. S. Gonçalves, D. V. B. Siqueira, R. A. Câmara<br> DOI: <a href="https://doi.org/10.22161/ijaers.11.4">10.22161/ijaers.11.4</a>   | Page No: 018-024 |
| <b><i>Effect of Calcium Carbonate on the Properties of Acid Soluble Cement Slurry</i></b><br>Catherine Ijeoma Miete-Ileberi, John Vitus Anaele, Samuel Mofunlewi<br> DOI: <a href="https://doi.org/10.22161/ijaers.11.5">10.22161/ijaers.11.5</a>  | Page No: 025-033 |
| <b><i>Breaking Index Study on Weighted Laplace Equation</i></b><br>Syawaluddin Hutahaean<br> DOI: <a href="https://doi.org/10.22161/ijaers.11.6">10.22161/ijaers.11.6</a>  | Page No: 034-043 |
| <b><i>A Comprehensive Review on Intelligence Control for Complex System</i></b><br>Md Jubair, Hossain MD Sabbir, Ngulube Lazarous, Hantosh Ali Hasan Abdulkarem, Shimul Paul, Muhammad Sabeeh khan, Mohammed Arfan, Abdullah al Rakib<br> DOI: <a href="https://doi.org/10.22161/ijaers.11.7">10.22161/ijaers.11.7</a>   | Page No: 044-049 |
| <b><i>Technical and Economic Assessment of the Integration of Refrigeration Concepts into the Proceeding Extension of Solar Energy Systems in Brazil</i></b><br>Christopher Wiencke, Giovani Ávila, Katja Biek<br> DOI: <a href="https://doi.org/10.22161/ijaers.11.8">10.22161/ijaers.11.8</a>  | Page No: 050-066 |

# Fabrication of pure porous CuO from microwave-synthesized MOF-199 by calcination in ambient air

Nam Ho Phung Khac

Institute of Chemistry and Materials, No. 17 Hoang Sam Street, Cau Giay District, Ha Noi, Vietnam

\*Email: homyhu@gmail.com

Received: 17 Nov 2023,

Receive in revised form: 25 Dec 2023,

Accepted: 02 Jan 2024,

Available online: 08 Jan 2024

©2024 The Author(s). Published by AI Publication. This is an open access article under the CC BY license

(<https://creativecommons.org/licenses/by/4.0/>).

**Keywords—** Copper (II) oxide, MOF-199, calcination process, oxidation catalysis.

**Abstract—** Metal-organic frameworks with porous characteristics are applied in many fields. This study used it as a superior raw material source for making transition metal oxides. By calcining the copper 1,3,5-benzene tricarboxylate framework in ambient air, copper(II) oxide was produced. The calcination temperature was investigated in the range of 250 to 700 °C. At a calcination temperature of 550 °C, the resultant CuO has a homogeneous size and shape within the 1-2 μm range. CuO's surface area of 33.16 m<sup>2</sup>/g is more excellent than several other materials and technologies used in CuO manufacture. Utilizing CuO generated by the MOF-199 calcination process for enhanced oxidation catalysis in treating organic gases and vapors is based on the research findings.

## I. INTRODUCTION

Metal-organic framework materials are formed from metal ions or clusters and organic ligands, so they are diverse in structure, quantity, and type. This combination has brought many superior properties to the material, such as porosity, flexibility, combination ability, and applicability. With unique features, metal-organic framework materials have been applied in many fields, such as gas production [1-4], environmental treatment [5-7], energy storage and conversion [8-10], medicine [11-13], etc. Copper(II) benzene tricarboxylate is a metal-organic framework material formed from Cu<sup>2+</sup> ions with 1,3,5-benzene tricarboxylate ligands. Cu-BTC has a regular octahedral structure and changes size according to synthesis conditions. Its' surface area ranges from 350 m<sup>2</sup>/g to 1,800 m<sup>2</sup>/g [14-17]. Pure and composite materials based on Cu-BTC are applied in fields such as CO<sub>2</sub> capture [16], H<sub>2</sub> adsorption [15], waste treatment [18], chemical catalysis [14, 19], sensors [20], etc. Cu-BTC is also used as a raw material to manufacture CuO<sub>x</sub> as a catalyst for metabolic reactions such as selective reduction reactions [21] and electrochemical decomposition [22]. CuO<sub>x</sub> made

from Cu-BTC is also used as a NO<sub>2</sub> sensor [23], an electrochemical sensor [24], and a supercapacitor [25].

## II. EXPERIMENTS

### 2.1. Chemical

1,3,5-Trimesic Acid (≥99%, H<sub>3</sub>BTC), Copper (II) chloride dihydrate (≥99%, CuCl<sub>2</sub>·2H<sub>2</sub>O), ethanol (≥98%, C<sub>2</sub>H<sub>5</sub>OH), Dimethylformamide (≥99%, DMF) were purchased from Macklin Co. Ltd.

### 2.2. Preparation of MOF-199 and CuO

In a typical procedure, 1.7 g of CuCl<sub>2</sub>·2H<sub>2</sub>O was dissolved in 150 ml of water/ethanol/DMF solvent mixture (1/1/1 ratio) under ultrasound for 30 min. Next, 2.8 g of H<sub>3</sub>BTC was added to the copper salt solution, and the mixture was sonicated for 10 min. The intermittent microwave reaction was carried out for 60 minutes (20 seconds running, 10 seconds off) with a temperature control of 60 °C. MOF-199 was collected after centrifugation, washing, and drying at 60 °C overnight. Microwave-synthesized Cu-BTC is calcined in ambient air at a temperature range of 200 - 700 °C. The heating time was set to 2 hours with a heating rate of 10 °C/min.

2.3. Characterization of materials

The phase structure of the sample was examined by X-ray diffraction (XRD PANalytical X' Pert Powder, Netherlands) using Cu K $\alpha$  radiation. The scanning electron microscope characterized the microstructure and morphology (SEM HITACHI S-4800). The chemical states and compositions of the sample were performed by energy-dispersive X-ray spectroscopy with mapping (EDX, HITACHI S-4800). The Brunauer–Emmett–Teller (BET) specific surface area and porosity of the samples were determined by nitrogen adsorption-desorption (NOVATouch LX2, QUANTACHROME, USA) at 77 K. Thermal gravimetric analysis (TGA/DTG NETZSCH STA 409 PC/PG, Germani) investigated the sample's thermodynamic property.

III. RESULT AND DISCUSSION

3.1. Characteristics of Cu-BTC

The morphology and structure of microwave-synthesized Cu-BTC were characterized by scanning electron microscopy imaging. The SEM image (Fig. 1 a&b) shows that the obtained Cu-BTC has an octahedral shape with 20-30 nm dimensions.

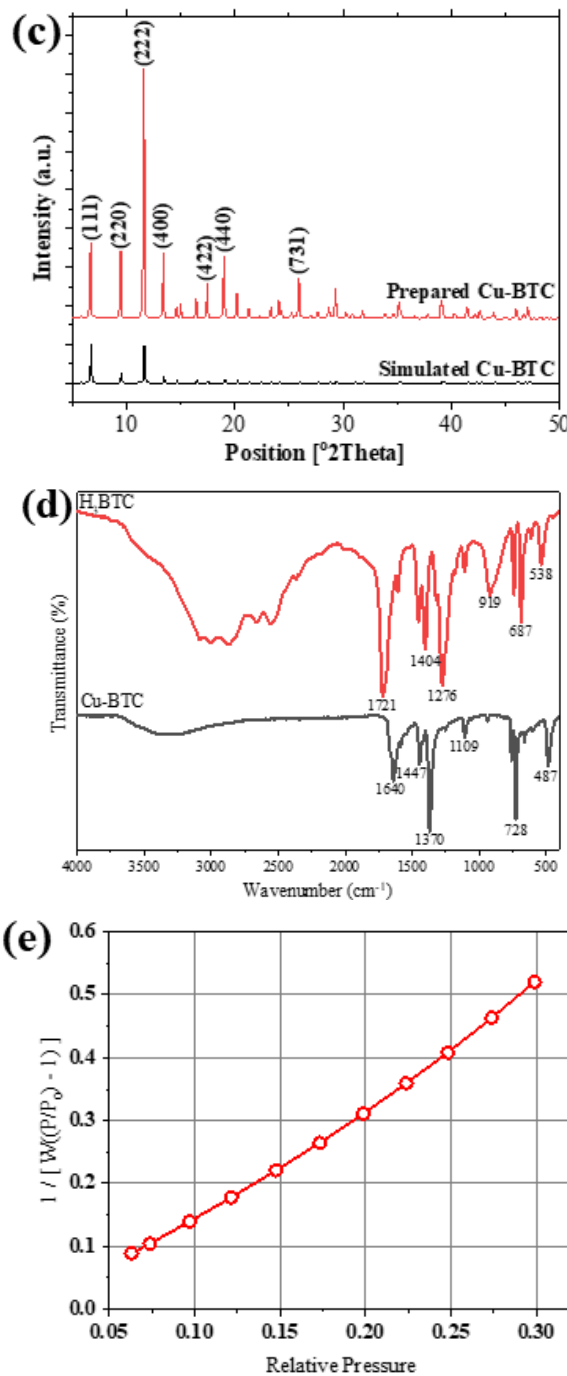
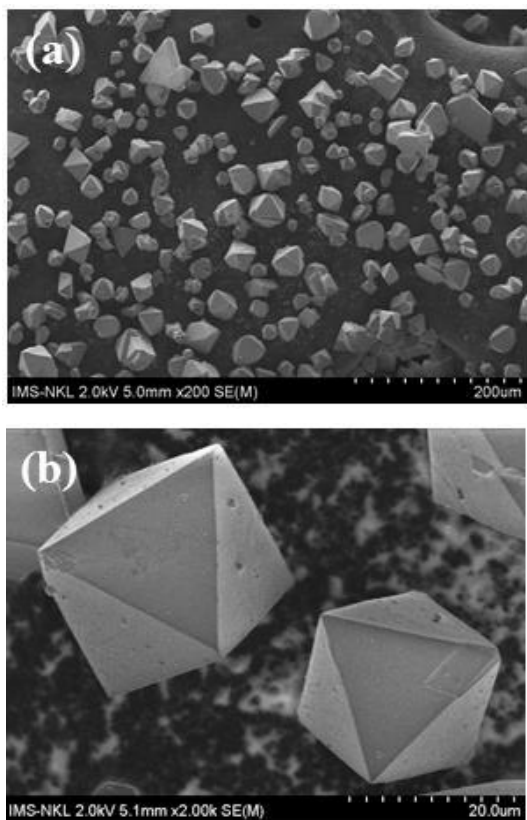


Fig. 1: SEM images of the prepared Cu-BTC (a, b); XRD pattern of simulated and prepared Cu-BTC (c); FTIR spectrum of H3BTC and Cu-BTC (d); the BET diagram of the prepared Cu-BTC (e).

The BET surface area of the material was found to be 1,059 m<sup>2</sup>/g. XRD test was performed (Fig 1c), and the diffraction pattern of the prepared sample was in good agreement with the simulated ones, indicating the formation of high-purity Cu-BTC [42]. FTIR was used to study the Cu-BTC bond properties further. As shown in Fig. 1d, the absorption band at 1721 cm<sup>-1</sup> corresponding to

protonated ligands disappeared in the spectrum of Cu-BTC, indicating complete deprotonation of H3BTC after the reaction. On the other hand, two characteristic bands at 1404 cm<sup>-1</sup> and 1276 cm<sup>-1</sup> assigned to the stretching vibrations of carboxylate groups were observed in Cu-BTC. At 728 cm<sup>-1</sup>, it is assigned the CH bond of the benzene ring, and the Cu-O bond forms between the carboxylic groups of H<sub>3</sub>BTC and Cu(II) [42].

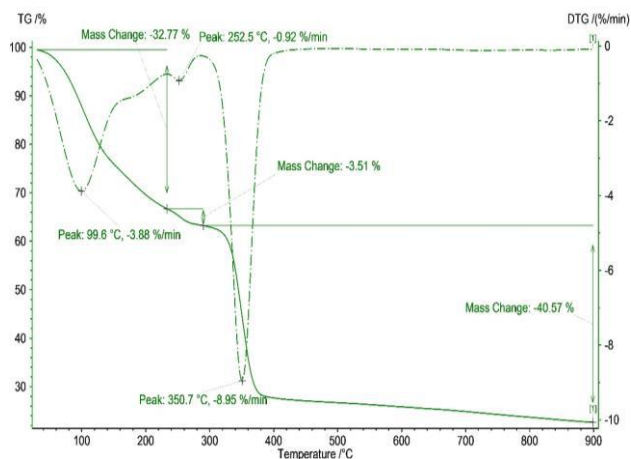


Fig. 2: The TG/DTG curve of the prepared Cu-BTC.

TG/DTG was used to test the microwave-synthesized Cu-BTC framework's thermal stability and thermal decomposition limit. As seen in Fig. 2, CuBTC begins to lose weight below 250 °C due to the evaporation of guest H<sub>2</sub>O molecules physically adsorbed in the MOF. The minimum of the DTG diagram appearing at 99.6 °C is assigned to the phase transition point of H<sub>2</sub>O. After that, a stable temperature occurs in the range of 250-350 °C, corresponding to two minima on the DTG diagram at 252.5 °C and 350.7 °C of the organic junction transformation in the framework. Next, the TG pattern increases sharply as the temperature rises due to the thermal decomposition of the BTC ligands in the frameworks. After 400 °C, the organic ligand has been wholly oxidized, and the resulting product is the remaining inorganic part. Thermal analysis results are the basis for choosing the calcination temperature for creating pure porous CuO.

### 3.2. Characteristics of pure porous CuO

Based on the TG thermal analysis results, the calcination temperature was selected from 250 °C to 700 °C. As shown in Figure 3, the sample calcined at 250 °C still retains the diffraction peaks of MOF-199. Diffraction peaks of CuO appear in calcined MOF-199 samples at calcination temperatures of 300 °C or higher. At different calcination temperatures, the peak intensities in the samples are different. Among the investigated temperatures, the diffraction pattern of the sample calcined

at 550 °C has the highest peak intensity. The results show that CuO produced from MOF-199 at this temperature has the best crystallinity.

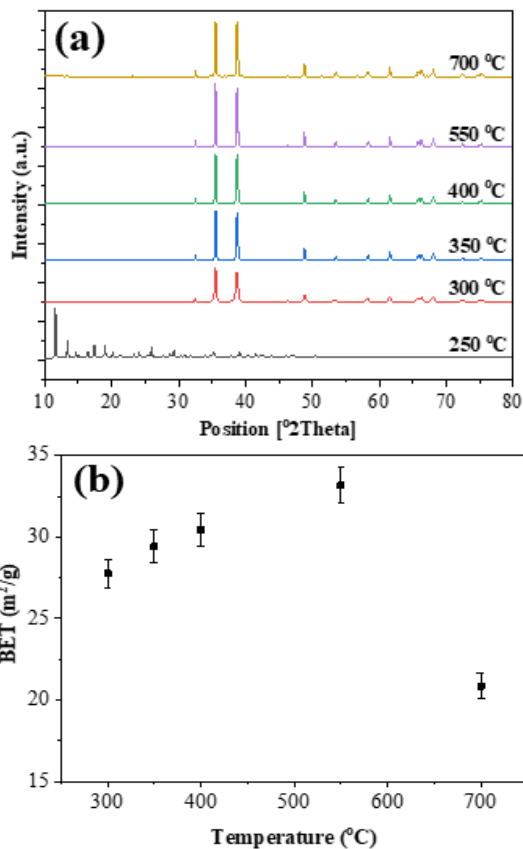


Fig.3: XRD patterns (a) and BET (b) values of calcined MOF-199 samples.

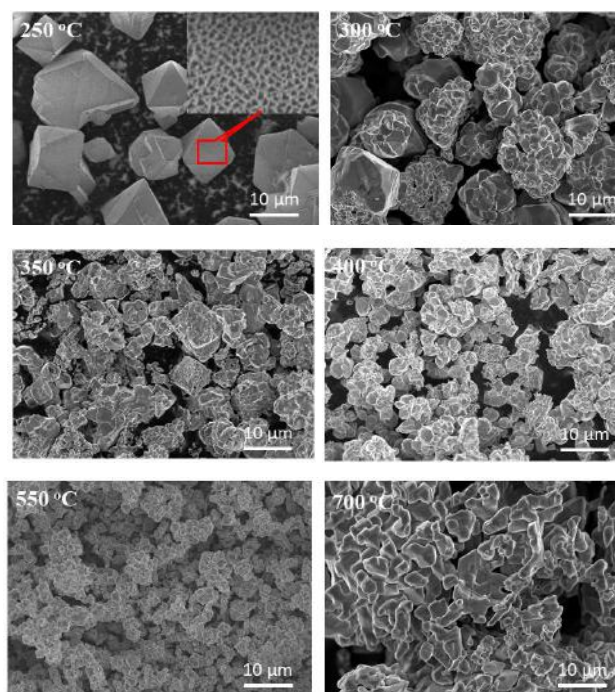


Fig. 4: The SEM of calcined MOF-199 samples.



The surface area of the prepared CuO samples was determined by N<sub>2</sub> isotherm adsorption measurement and is shown in Fig. 3b. The BET value showed a slight increase when the calcination temperature was increased. Still, it decreased suddenly when the calcination temperature rose to 700 °C. The hypothesis is that the porous framework collapses when the temperature increases and the crystal structure of CuO is also poorer.

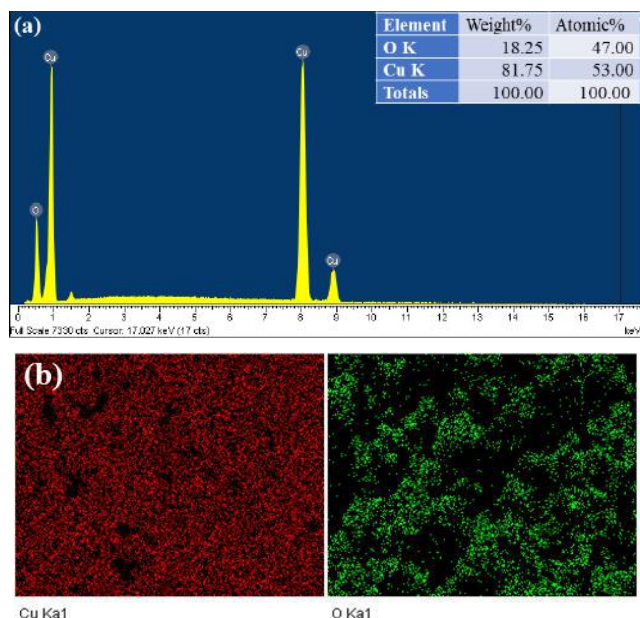


Fig. 5: EDX spectra (a) and mapping images (b) of CuO-derivated MOF-199 at 550 °C.

The morphology and size of MOF-199 calcined at different temperatures are shown in Figure 4. SEM images show an evident change in the crystal structure of Cu-BTC according to calcination temperature. At 250 °C, the metal-organic framework structure remained intact. However, there were signs of thermal impact on the bond framework, leading to the destruction of the crystal surface. Samples calcined at 300 °C showed separation of grains from the framework but retained the original framework's morphology. Some particles have not been effectively affected by heat on their structures. When increasing the calcination temperature to 350 °C and 400 °C, CuO particles begin to form and leave the frame structure. The sample calcined at a higher temperature (550 °C) produced particles of uniformly small size. According to the calculation results, this sample has the highest surface area (Fig. 3b) and sharpest crystallinity (Fig. 3a). However, when the calcination temperature reaches 700 °C, CuO particles tend to agglomerate to create more giant cubes. Although the melting temperature of CuO is more than 1300 °C, CuO formed from the heating process of MOF-199, which breaks the framework at a temperature lower than the melting temperature, can still solidify. This

phenomenon affects the crystalline properties and other characteristics of CuO produced at this temperature. This result coincides with published research on the recrystallization annealing temperature for CuO [27].

The EDX spectrum and mapping image of CuO prepared at 550 °C, shown in Figure 5 (a&b), show that only two elements in the sample (Cu and O) are uniformly distributed. This result demonstrates the purity of CuO when made from MOF-199 by calcination in air. The atomic ratio in the compound also shows nCu/nO ~ 1/1, consistent with the molecular formula of CuO.

#### IV. CONCLUSION

Copper(II) oxide was prepared from the copper 1,3,5-benzene tricarboxylate framework by calcination in ambient air. The resulting CuO has uniform size and morphology within the 1-2 um range at a calcination temperature of 550 °C. The surface area of CuO reaches 33.16 m<sup>2</sup>/g, higher than some results of manufacturing CuO by methods and other materials. The research results are the basis for applying CuO produced by the MOF-199 calcination method for advanced oxidation catalysis in treating organic gases and vapors.

#### ACKNOWLEDGEMENTS

This research is funded by the Department of Inorganic Materials, Institute of Chemistry and Materials.

#### REFERENCES

- [1] Liu, K.-G.; Bigdeli, F.; Panjehpour, A.; Hwa Jhung, S.; Al Lawati, H. A. J.; Morsali, A. (2023). Potential applications of MOF composites as selective membranes for separation of gases. *Coordination Chemistry Reviews*, 496, 215413. doi: 10.1016/j.ccr.2023.215413
- [2] Mehri Lighvan, Z.; Hosseini, S. R.; Norouzbahari, S.; Sadatnia, B.; Ghadimi, A. (2023). Synthesis, characterization, and selective gas adsorption performance of hybrid NH<sub>2</sub>-MIL-101(Fe)/ZIF-8 metal organic framework (MOF). *Fuel*, 351(5), 128991. doi: 10.1016/j.fuel.2023.128991
- [3] Tao, Y. R.; Xu, H. J. (2024). A critical review on potential applications of Metal-Organic frameworks (MOFs) in adsorptive carbon capture technologies. *Applied Thermal Engineering*, 236(Part A), 121504. doi: 10.1016/j.applthermaleng.2023.121504
- [4] Shi, X.; Lee, G. A.; Liu, S.; Kim, D.; Alahmed, A.; Jamal, A.; Wang, L.; Park, A.-H. A. (2023). Water-stable MOFs and hydrophobically encapsulated MOFs for CO<sub>2</sub> capture from ambient air and wet flue gas. *Materials Today*, 65, 207-226. doi: 10.1016/j.mattod.2023.03.004.
- [5] Zhang, Y.; Liu, H.; Gao, F.; Tan, X.; Cai, Y.; Hu, B.; Huang, Q.; Fang, M.; Wang, X. (2022). Application of

- MOFs and COFs for photocatalysis in CO<sub>2</sub> reduction, H<sub>2</sub> generation, and environmental treatment. *EnergyChem*, 4 (4), 100078. doi: 10.1016/j.enchem.2022.100078.
- [6] Poonia, K.; Patial, S.; Raizada, P.; Ahamad, T.; Parwaz Khan, A. A.; Van Le, Q.; Nguyen, V. H.; Hussain, C. M.; Singh, P. (2023). Recent advances in Metal Organic Framework (MOF)-based hierarchical composites for water treatment by adsorptional photocatalysis: A review. *Environ Res*, 222, 115349. doi: 10.1016/j.envres.2023.115349
- [7] Liu, X.; Shan, Y.; Zhang, S.; Kong, Q.; Pang, H. (2023). Application of metal organic framework in wastewater treatment. *Green Energy & Environment*, 8 (3), 698-721. doi: 10.1016/j.gee.2022.03.005
- [8] Yan, D.; Li, M. (2023). Stearic acid-modified MOF-based composite phase change materials for solar-thermal energy conversion and storage. *Solar Energy*, 262, 111843. doi: 10.1016/j.solener.2023.111843
- [9] Dai, Y.; Zhang, G.; Peng, Y.; Li, Y.; Chi, H.; Pang, H. (2023). Recent progress in 1D MOFs and their applications in energy and environmental fields. *Advances in Colloid and Interface Science*, 321, 103022. doi: 10.1016/j.cis.2023.103022
- [10] Hu, X.; Zheng, W.; Wu, M.; Chen, L.; Chen, S. (2023). Composites of metal-organic frameworks (MOFs) and LDHs for energy storage and environmental applications: Fundamentals, progress, and perspectives. *Sustainable Materials and Technologies*, 37, e00691. doi: 10.1016/j.susmat.2023.e00691
- [11] Sun, Y.; Jiang, X.; Liu, Y.; Liu, D.; Chen, C.; Lu, C.; Zhuang, S.; Kumar, A.; Liu, J. (2021). Recent advances in Cu(II)/Cu(I)-MOFs based nano-platforms for developing new nano-medicines. *J Inorg Biochem*, 225, 111599. doi: 10.1016/j.jinorgbio.2021.111599
- [12] Le Thanh, B.; Nguyen Thi, H. P.; La Duc, D.; Nguyen Thi, P. (2021). Green synthesis of MIL-100(Fe) metal-organic frameworks as a carrier for chloroquine delivery. *Journal of Military Science and Technology*, 76 (12), 61-67. doi: 10.54939/1859-1043.j.mst.76.2021.61-67
- [13] Le B. T.; Nguyen C. Q.; Nguyen P. T.; Ninh H. D.; Le T. M.; Nguyen P. T. H.; D., L. D. (2022). Fabrication of Porous Fe-Based Metal-Organic Complex for the Enhanced Delivery of 5-Fluorouracil in In Vitro Treatment of Cancer Cells. *ACS Omega*, 7(50), 46674-46681. doi: 10.1021/acsomega.2c05614
- [14] Patel, N. B.; Vala, N.; Shukla, A.; Neogi, S.; Mishra, M. K. (2023). Catalytic activity of Cu-BTC metal organic framework for borrowing hydrogen and tandem reactions of an alcohol under solvent and base free condition. *Inorganica Chimica Acta*, 554, 121546. doi: 10.1016/j.ica.2023.121546
- [15] Peedikakkal, A. M. P.; Aljundi, I. H. (2020). Mixed-Metal Cu-BTC Metal-Organic Frameworks as a Strong Adsorbent for Molecular Hydrogen at Low Temperatures. *ACS Omega*, 5 (44), 28493-28499. doi: 10.1021/acsomega.0c02810
- [16] Ho, P. S.; Chong, K. C.; Lai, S. O.; Lee, S. S.; Lau, W. J.; Lu, S.-Y.; Ooi, B. S. (2022). Synthesis of Cu-BTC Metal-Organic Framework for CO<sub>2</sub> Capture via Solvent-free Method: Effect of Metal Precursor and Molar Ratio. *Aerosol and Air Quality Research*, 22 (12). 220135. doi: 10.4209/aaqr.220235
- [17] Zhao, T.; Nie, S.; Luo, M.; Xiao, P.; Zou, M.; Chen, Y. (2024). Research progress in structural regulation and applications of HKUST-1 and HKUST-1 based materials. *Journal of Alloys and Compounds*, 974, 172897. doi: 10.1016/j.jallcom.2023.172897
- [18] Mazani, M.; Aghapour Aktij, S.; Rahimpour, A.; Tavajohi Hassan Kiadeh, N. (2019). Cu-BTC Metal-Organic Framework Modified Membranes for Landfill Leachate Treatment. *Water*, 12 (1). 91. doi: 10.3390/w12010091
- [19] Venu, B.; Shirisha, V.; Vishali, B.; Naresh, G.; Kishore, R.; Sreedhar, I. (2020). Venugopal, A., A Cu-BTC metal-organic framework (MOF) as an efficient heterogeneous catalyst for the aerobic oxidative synthesis of imines from primary amines under solvent free conditions. *New Journal of Chemistry*, 44 (15), 5972-5979. doi: 10.1039/C9NJ05997K
- [20] Li, C.; Wu, K. (2021). Cu-BTC frameworks based electrochemical sensor for hazardous malachite green in aquaculture. *Anal Chim Acta*, 1162, 338473. doi: 10.1016/j.aca.2021.338473
- [21] Yang, J.; Yuling, L.; Penghe, Z.; Hao, S.; Chuanchuan, D.; Ruihao, S.; Feifei, L. (2022). Chemical thermodynamic and catalytic mechanism analysis of Cu-BTC-derived CuOx/C catalyst for selective catalytic reduction (SCR). *Molecular Catalysis*, 531, 112710. doi: 10.1016/j.mcat.2022.112710
- [22] Huang, P.; Lei, J.; Sun, Z.; Hu, X. (2021). Fabrication of MOF-derived CuOx-C electrode for electrochemical degradation of ceftazidime from aqueous solution. *Chemosphere*, 268, 129157. doi: 10.1016/j.chemosphere.2020.129157
- [23] Ding, Y.; Guo, X.; Liang, C.; Wu, Z.; Meng, G.; Zang, Z.; He, Y. (2022). Temperature modulated p-n transition NO<sub>2</sub> sensor in metal-organic framework-derived CuO. *Sensors and Actuators B: Chemical*, 359, 131605. doi: 10.1016/j.snb.2022.131605
- [24] Gu, C.; Wang, Q.; Zhang, L.; Yang, P.; Xie, Y.; Fei, J. (2020). Ultrasensitive non-enzymatic pesticide electrochemical sensor based on HKUST-1-derived copper oxide @ mesoporous carbon composite. *Sensors and Actuators B: Chemical*, 305, 127478. doi: 10.1016/j.snb.2019.127478
- [25] He, L.; Liu, J.; Yang, L.; Song, Y.; Wang, M.; Peng, D.; Zhang, Z.; Fang, S. (2018). Copper metal-organic framework-derived CuOx-coated three-dimensional reduced graphene oxide and polyaniline composite: Excellent candidate free-standing electrodes for high-performance supercapacitors. *Electrochimica Acta*, 275, 133-144. doi: 10.1016/j.electacta.2018.04.089
- [26] Saleem, S.; Jabbar, A. H.; Jameel, M. H.; Rehman, A.; Kareem, Z. H.; Abbas, A. H.; Ghaffar, Z.; Razzaq, S. A.; Pashameah, R. A.; Alzahrani, E.; Ng, E.-P.; Sapuan, S. M. (2022). Enhancement in structural, morphological, and optical properties of copper oxide for optoelectronic device applications. *Nanotechnology Reviews*, 11 (1), 2827-2838. doi: 10.1515/ntrev-2022-0473

- [27] Sivayogam, D.; Kartharinal Punithavathy, I.; Johnson Jayakumar, S.; Mahendran, N. (2022). Study on structural, electro-optical and optoelectronics properties of CuO nanoparticles synthesis via sol gel method. *Materials Today: Proceedings*, 48(part 2), 508-513. doi: 10.1016/j.matpr.2021.04.494
- [28] Hoàng, T. H. H.; Đào, N. N. (2014). Characteristics and catalytic activity for the CO oxidation reaction of CuO, CeO<sub>2</sub> oxides and CuO-CeO<sub>2</sub> mixed oxides. *Journal of Chemistry*, 52 (1), 86-90. doi:
- [29] Nguyen, T. T. T.; Nguyen, Y. N. N.; Tran, X. T.; Nguyen, T. T. T.; Tran, T. V. (2023). Green synthesis of CuO, ZnO and CuO/ZnO nanoparticles using *Annona glabra* leaf extract for antioxidant, antibacterial and photocatalytic activities. *Journal of Environmental Chemical Engineering*, 11 (5). 111003. doi: 10.1016/j.jece.2023.111003
- [30] Jadhav, A. L.; Jadhav, S. L.; Mandlekar, B. K.; Kadam, A. V. (2023). Hydrothermally synthesized three-dimensional hierarchical CuO nanomaterials for energy storage applications. *Materials Chemistry and Physics*, 310. 128494. doi: 10.1016/j.matchemphys.2023.128494
- [31] Dai, X.; Fang, X.; Wu, H. (2024). Highly sensitive and selective room-temperature NO sensor based on rich-oxygen vacancy CuO nanoflakes. *Materials Letters*, 356. 135564. doi: 10.1016/j.matlet.2023.135564
- [32] Ye, Y.; Xu, J.; Gao, L.; Zang, S.; Chen, L.; Wang, L.; Mo, L. (2023). CuO/CeO<sub>2</sub> catalysts prepared by modified impregnation method for ethyl acetate oxidation. *Chemical Engineering Journal*, 471. 144667. doi: 10.1016/j.cej.2023.144667
- [33] Shen, Z.; Xing, X.; Wang, S.; Lv, M.; Zheng, Z.; Li, J.; Li, H. (2023). High activity of CuO/#-Fe<sub>2</sub>O<sub>3</sub> for low temperature CO oxidation: Effect of support crystal types in catalyst design. *Journal of the Energy Institute*, 110, 101339. doi: 10.1016/j.joei.2023.101339
- [34] Yun, J.; Wu, L.; Hao, Q.; Teng, Z.; Gao, X.; Dou, B.; Bin, F. (2022). Non-equilibrium plasma enhanced oxygen vacancies of CuO/CeO<sub>2</sub> nanorod catalysts for toluene oxidation. *Journal of Environmental Chemical Engineering*, 10 (3). 107847. doi: 10.1016/j.jece.2022.107847
- [35] Dorner, L.; Cancellieri, C.; Rheingans, B.; Walter, M.; Kagi, R.; Schmutz, P.; Kovalenko, M. V.; Jeurgens, L. P. H. (2019). Cost-effective sol-gel synthesis of porous CuO nanoparticle aggregates with tunable specific surface area. *Sci Rep*, 9 (1), 11758. doi: 10.1038/s41598-019-48020-8
- [36] Anitha, T. V.; Gadha Menon, K.; Venugopal, K.; Vimalkumar, T. V. (2024). Investigating the role of film thickness on the physical properties of sol-gel coated CuO thin films: Discussing its potentiality in optoelectronic applications. *Materials Science and Engineering: B*, 299, 116960. doi: 10.1016/j.mseb.2023.116960
- [37] Abdel-Galil, A.; Moussa, N. L. (2023). Nanostructure CuO thin film deposited by spray pyrolysis for technological applications. *Radiation Physics and Chemistry*, 212. 111119. doi: 10.1016/j.radphyschem.2023.111119
- [38] Mahana, D.; Mauraya, A. K.; Singh, P.; Muthusamy, S. K. (2023). Evolution of CuO thin films through thermal oxidation of Cu films prepared by physical vapour deposition techniques. *Solid State Communications*, 366-367, 115152. doi: 10.1016/j.ssc.2023.115152
- [39] Kongvarhodom, C.; Nammahachak, N.; Tippomuang, W.; Fongchaiya, S.; Turner, C.; Ratanaphan, S. (2021). Role of crystallographic textures on the growth of CuO nanowires via thermal oxidation. *Corrosion Science*, 193, 109898. doi: 10.1016/j.corsci.2021.109898
- [40] Warsi, A.-Z.; Hussien, O. K.; Iftikhar, A.; Aziz, F.; Alhashmialameer, D.; Mahmoud, S. F.; Warsi, M. F.; Saleh, D. I. (2022). Co-precipitation assisted preparation of Ag<sub>2</sub>O, CuO and Ag<sub>2</sub>O/CuO nanocomposite: Characterization and improved solar irradiated degradation of colored and colourless organic effluents. *Ceramics International*, 48 (13), 19056-19067. doi: 10.1016/j.ceramint.2022.03.194
- [41] Banu, T.; Jamal, M.; Gulshan, F. (2023). Opto-structural properties and photocatalytic activities of CuO NPs synthesized by modified sol-gel and Co-precipitation methods: A comparative study. *Results in Materials*, 19, 100419. doi: 10.1016/j.rinma.2023.100419
- [42] Garg, D.; Rekhi, H.; Kaur, H.; Singh, K.; Malik, A. K. (2022). A Novel Method for the Synthesis of MOF-199 for Sensing and Photocatalytic Applications. *J Fluoresc*, 32 (3), 1171-1188. doi: 10.1007/s10895-022-02902-9

# Performance Evaluation of Neural Networks in Road Sign Recognition

Sanjit Kumar Saha

Department of Computer Science and Engineering, Jahangirnagar University, Bangladesh

Received: 20 Nov 2023,

Receive in revised form: 27 Dec 2023,

Accepted: 05 Jan 2024,

Available online: 13 Jan 2024

©2024 The Author(s). Published by AI  
Publication. This is an open access article under  
the CC BY license

(<https://creativecommons.org/licenses/by/4.0/>).

**Keywords—** Hybrid Neural network, Neural network, Pattern recognition, Performance evaluation, Road sign recognition

**Abstract—** This paper presents an in-depth study of road sign recognition techniques leveraging neural networks. Road sign recognition stands as a critical component of intelligent transportation systems, contributing to enhanced road safety and efficient traffic management. The paper focuses on exploring various neural network architectures for example, backpropagation neural network and hybrid neural network which is a combination of two neural network (backpropagation neural network and bidirectional associative memory), training methodologies, dataset considerations, and performance evaluations for accurate and real-time recognition of road signs. The experimental result shows that the hybrid neural network is faster than the backpropagation neural network in the completion of the training process with higher recognition accuracy.

## I. INTRODUCTION

In today's dynamic and interconnected world, the safety and efficiency of transportation systems stand as paramount concerns. Road sign recognition, a fundamental component of intelligent transportation systems, plays a pivotal role in enhancing road safety, facilitating efficient traffic management, and enabling the progression towards autonomous driving. Recognizing and interpreting road signs is crucial for providing timely and accurate information to drivers and autonomous vehicles, aiding in adherence to traffic regulations, and ensuring safe navigation on roadways.

Road signs convey essential messages to drivers, alerting them to speed limits, warnings about hazards, providing directions, and communicating regulatory instructions. The ability to recognize these signs accurately and swiftly is imperative, as it directly influences driver decision-making, reduces accident risks, and contributes significantly to the overall efficiency of transportation networks.

Traditionally, road sign recognition relied on manual interpretation by human drivers. However, advancements in computer vision, machine learning, and neural network-

based approaches have revolutionized this field. These technologies enable automated recognition and interpretation of road signs from images or video streams captured by cameras mounted on vehicles or infrastructure.

The complexity of road sign recognition arises from various factors, including diverse environmental conditions, variations in sign appearances due to aging, damage, or regional differences in designs and symbols, as well as the need for real-time processing to ensure timely responses. Overcoming these challenges requires sophisticated algorithms, robust training methodologies, and extensive datasets that encompass the diversity of road signs encountered in different geographical locations and environmental conditions.

In recent years, there has been notable research advancement in the domain of road sign recognition. Namyang and Phimoltares [1] utilized a combination of Support Vector Machines (SVM) and Random Forest algorithms, along with HOG and the Color Layout Descriptor (CLD), for traffic sign classification. Soni et al. [2] employed HOG and LBP descriptors with Principal Component Analysis (PCA) and Support Vector Machines (SVM) for traffic sign classification. Sapijaszko et al. [3]

proposed a traffic sign recognition system encompassing stages such as normalization, feature extraction, compression, and classification. Aziz and Youssef [4] proposed a traffic sign recognition system utilizing feature extraction and the Extreme Learning Machine (ELM) algorithm. Wang [5] introduced a traffic sign classification system employing three machine learning classifiers: Logistic Regression (LR), Multilayer Perceptron (MLP), and SVM.

But, neural networks, particularly Backpropagation Neural Network, have demonstrated remarkable capabilities in image recognition tasks, making them a promising approach for road sign recognition. This paper outlines the performance evaluation of the backpropagation neural network and the hybrid neural network.

## II. PRELIMINARIES

### A. Road Signs

Road signs serve as crucial elements of traffic control and safety, providing essential information to drivers, pedestrians, and other road users. These signs are standardized visual cues that communicate various instructions, warnings, regulations, and guidance about road conditions. Figure 1 shows some road signs with their corresponding meanings.

| Signs   | Meaning         |
|---|-----------------|
|  | No parking      |
|  | School zone     |
|  | Crossroad ahead |
|  | Gas             |
|  | No U turn       |
|  | No pedestrians  |

Fig. 1 Road signs

### B. Neural Networks

A neural network is characterized as a reasoning model inspired by the human brain's structure. The brain is composed of a highly interconnected network of nerve cells known as neurons, which serve as the fundamental units for processing information. Human brains encompass nearly 10 billion neurons and an extensive network of 60 trillion synapses interconnecting them, as documented by Shepherd and Koch [6] Leveraging the simultaneous activation of

multiple neurons enables the brain to execute tasks at a considerably higher speed compared to today's fastest computers.

Despite their straightforward architecture, a collection of neurons yields remarkable computational capabilities. Each neuron comprises a cell body, a multitude of dendrites (fiber-like structures), and a solitary elongated fiber identified as the axon. Dendrites form an intricate network surrounding the cell body, while the axon extends towards other neurons' dendrites and cell bodies. Refer to Figure 2 for an illustrative representation of a biological neuron.

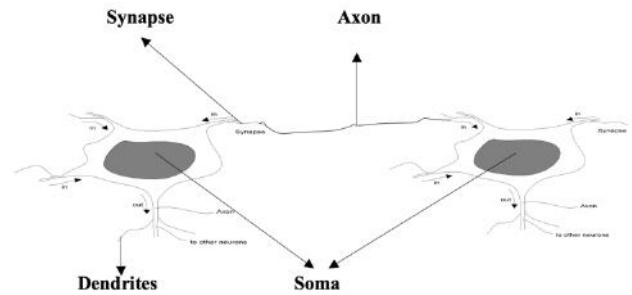


Fig. 2 Biological neuron

Our brain functions as an intricate and sophisticated information-processing system that operates in a highly complex, nonlinear, and parallel manner. Unlike traditional systems where data processing occurs in specific areas, in neural networks, information is stored and processed simultaneously across the entire network. This global approach to both data and its processing distinguishes neural networks by their widespread rather than localized functionality. The adaptability of connections between neurons, causing variations that contribute to arriving at the 'correct' outcome, highlights the plasticity of neural networks. Consequently, these networks possess the capacity to learn from experiences, marking learning as a foundational and vital attribute of biological neural networks. The innate ability to learn effortlessly prompted endeavors to replicate a biological neural network's functionality within a computer environment.

### C. Backpropagation Neural Network

The backpropagation neural network (BPNN) architecture comprises an input layer, an output layer, and one or more hidden layers. The number of input units corresponds to the quantity of bits or values representing the input pattern, accommodating these  $n$  bits or values. Similarly, the count of output units is determined by the bits or values associated with the output pattern. Conventionally, the network establishes complete connectivity exclusively between adjacent layers, forming fully connected pathways throughout the network as shown in Figure 3.

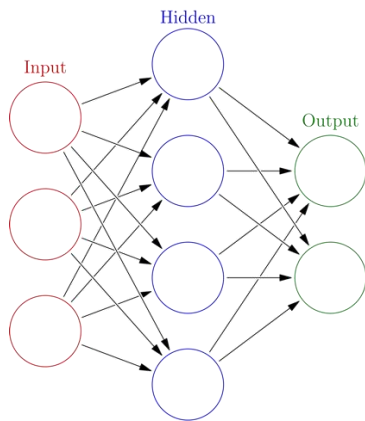


Fig. 3 Backpropagation Neural Network

The backpropagation method uses two steps:

1. In the ‘forward step’, the input is applied and allowed to propagate to the output. The error values of the output units are calculated by subtracting output value from target value for each unit.
2. In the ‘backward step’, errors are propagated backwards, and weights are modified.

The network's training objective involves refining the weights to ensure that a given set of inputs yields the intended set of outputs. For conciseness, these input-output combinations are often denoted as vectors. Training operates on the premise that each input vector aligns with a target vector, symbolizing the anticipated output; collectively, these form a training pair. Typically, a network undergoes training with multiple such pairs. For instance, an input pair might encompass a sequence of ones and zeros representing a binary image corresponding to an alphabet letter. The compilation of these training pairs constitutes a training set.

D. Bidirectional Associative Memory

Bart Kosko [7] introduced Bidirectional Associative Memory (BAM) as a heteroassociative neural network as shown in Figure 4. It operates by receiving an input pattern represented as a vector across one group of neurons and generates a correlated yet distinct output vector across another set, and conversely does the same in reverse.

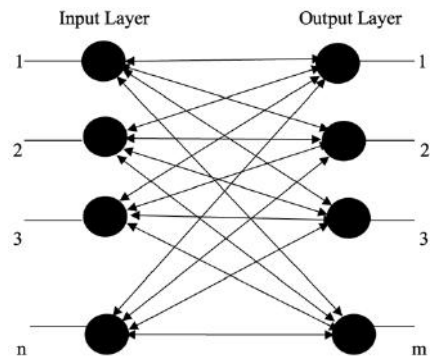


Fig. 4 BAM Network Architecture

The main features of a BAM are given below:

- A BAM comprises two layers of interconnected neurons.
- Neurons within one layer establish complete connections with neurons in the other layer.
- There are no interconnections among neurons within the same layer.
- The storage capacity and reliability of recall hinge on the network architecture and the algorithms used for both recalling and learning.
- Enhancing performance can be achieved by introducing additional layers or establishing more interconnections among neurons.

The input to a BAM network is a vector of real number, usually in the set  $\{-1, +1\}$ . The output is also a vector in the set  $\{-1, +1\}$  with the same or different dimension. These vectors can be considered as patterns, and the network makes heteroassociation of patterns. If the output is required to be the same as input, then the network is said to make auto-association.

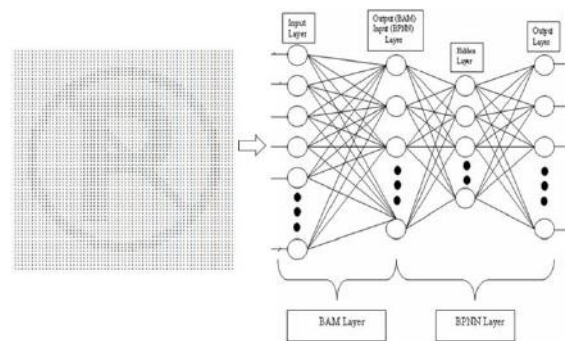


Fig. 5 Hybrid neural network

E. Hybrid Neural Network

A hybrid neural network consists of two distinct neural networks: the BAM neural network and the Bidirectional neural network. BAM is employed to reduce the dimensions of the feature matrix, thereby enhancing the speed and

efficiency of recognition. Figure 5 illustrates the network architecture for this hybrid neural network.

### III. EXPERIMENTS AND PERFORMANCE EVALUATION

Recognition of Road Sign is a step-by-step processing of road sign. These processes include:

- Preprocessing
- Recognition of sign
- Performance evaluation

The effectiveness of the algorithm has been justified for different Road Sign images of different resolutions. The algorithm is capable of preprocessing and recognizing signs of any grayscale images. The implementation of the algorithm was carried out using the C programming language.

At the beginning, a sign is chosen. The sign is a grayscale image. Whole of the task is done by the following way:

#### A. Preprocessing

Road signs are being preprocessed by following a sequence of operations: Capturing, Binary image conversion.

*Capturing:* Road sign acquisition involves utilizing a camera for capturing purposes. For this study, specific obligatory road signs were utilized to create an image database stored as BMP type files. As part of the capturing process, standardization, and geometric normalization, involving adjustments in size and direction, were applied to the images. For analysis purposes, the images were resized to a resolution of  $64 \times 64$  pixels, as depicted in Figure 6.



Fig. 6 Road sign image

*Binary Image Conversion:* The initial image was notably in color. It underwent a transformation into a grayscale image and subsequently underwent binarization, a process chosen for its simplicity in pattern matching during sign recognition. Each sign is represented as a matrix of numerical values, ranging from 0 to 255, which can be further translated into binary format (0s and 1s). The conversion sequence is demonstrated in Figure 7.

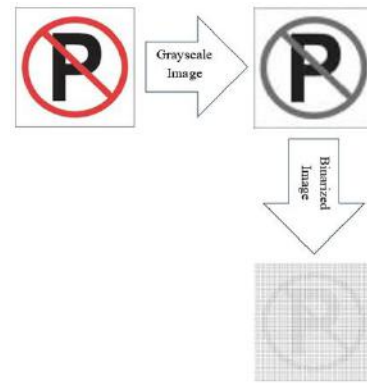


Fig. 7 Image conversion

The road signs are arranged within a  $64 \times 64$  grid and inputted into the neural network's input layer as feature vectors or training patterns. Consequently, the grid configurations are depicted as vectors comprising 4096 components (where each vector component is 1 if the pixel in the grid is shaded, otherwise it is 0). The hidden layers encompass 60 neurons each, which account for 60% of the input layer. Considering a total of 64 signs, inclusive of both mandatory and other signs, the output layer comprises 64 neurons. Having 64 neurons in the output layer enables the representation of a 6-bit code ( $2^6 = 64$ ) for classifying each target output. Hence, the target outputs range from 000000 to 111111, aligning with each distinct sign.

#### B. Recognition of sign

The road sign recognition phase is most important and complicated phase. Hence, the sign is  $64 \times 64$  pixels image. Each sign has a feature matrix of 4096 elements in it. Each element is nothing but binary values (0 and 1).

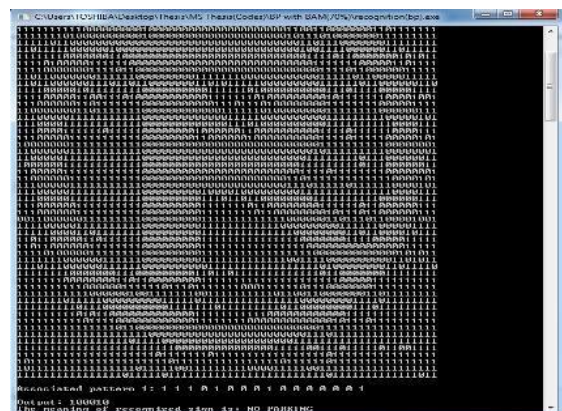


Fig. 8 Recognition of a sign "NO PARKING"

Hence, in this experiment the number of neurons in input layer is 4096, neurons in input layer for BPNN and output layer for BAM is 16, number of neurons in hidden layer is 10, and finally the neurons in output layer is 6. The

number of neurons in hidden layer can vary from 50% to 70% of its input neurons.

Figure 8 shows the snapshot of the program output of a normal image.

C. Performance evaluation

To assess the neural network's performance, a series of experiments were conducted, employing separate training and test image sets for each sign without any overlap between them. The back-propagation neural network underwent training utilizing default learning parameters (learning rate 0.3, threshold 1) over 75 epochs. Subsequently, the network was employed to recognize individual signs.

Throughout the training process, the program continued execution until the error reached a minimum threshold level, illustrating the error reduction per iteration in a graphical representation. Initially, the task was implemented using the BPNN algorithm alone, followed by merging the BAM and BPNN algorithms to train and recognize road signs. Upon analysis, it was observed that employing the hybrid network (BAM and BPNN) required fewer iterations for training and less time for sign recognition compared to BPNN alone.

Table 1 Iteration Vs. Error (70%)

| Iteration | BP (70%) | BP With BAM (70%) |
|-----------|----------|-------------------|
| 2         | 3,866509 | 1,959864          |
| 5         | 3,858203 | 1,894699          |
| 10        | 3,503066 | 1,881338          |
| 100       | 3,435648 | 1,702669          |
| 500       | 3,217658 | 1,119279          |
| 1000      | 3,095643 | 0,612061          |
| 1500      | 2,943532 | 0,575292          |
| 2000      | 2,873423 | 0,554884          |
| 2500      | 2,806753 | 0,543144          |
| 3000      | 2,645987 | 0,53713           |
| 3500      | 2,546534 | 0,531881          |
| 4000      | 2,513423 | 0,492877          |
| 4500      | 2,485645 | 0,315097          |
| 5000      | 2,437864 | 0,293473          |
| 6000      | 2,376588 | 0,278986          |
| 7000      | 2,238757 | 0,272395          |
| 8000      | 2,187658 | 0,268759          |
| 9000      | 2,074542 | 0,266053          |
| 10000     | 1,984532 | 0,264022          |

|       |          |          |
|-------|----------|----------|
| 15000 | 1,912328 | 0,258816 |
| 20000 | 1,813421 | 0,256447 |
| 25000 | 1,746574 | 0,255095 |
| 30000 | 1,698342 | 0,25338  |
| 34075 | 1,607801 | 0,009981 |
| 40000 | 1,576457 |          |
| 45000 | 1,53768  |          |
| 50000 | 1,457854 |          |
| 55000 | 1,356245 |          |
| 60000 | 1,247856 |          |
| 65000 | 1,109854 |          |
| 70000 | 1,065242 |          |
| 75000 | 0,176542 |          |
| 80000 | 0,039947 |          |
| 85000 | 0,017469 |          |
| 88043 | 0,009997 |          |

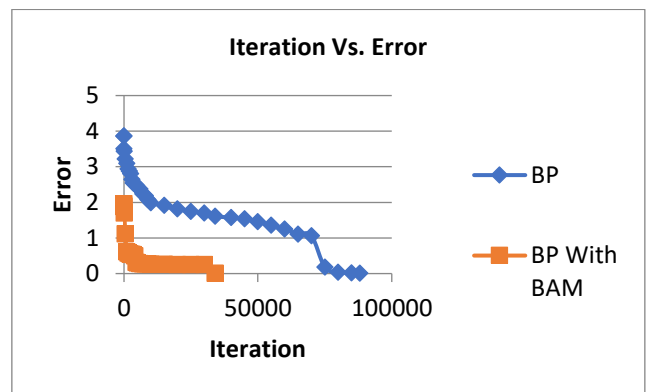


Fig. 9 Iterations Vs. Error (70%)

The training process involved eight training input patterns and employed an error threshold (e.g., 0.001) to halt training. The number of iterations was contingent upon the percentage of the hidden layer and the algorithm utilized during training. For instance, setting the hidden layer to 70% of the input layer resulted in 88043 iterations, while reducing the hidden layer to 50% led to 43067 iterations.

Upon adopting the hybrid network with the same percentage of the hidden layer, the iteration count decreased further. Specifically, it decreased from 34075 to 14977, illustrating an even more pronounced reduction in iterations compared to previous results.



Table 2 Iteration Vs. Error (50%)

| Iteration | BP (50%) | BP With BAM (50%) |
|-----------|----------|-------------------|
| 2         | 6,933186 | 3,07014           |
| 5         | 5,694922 | 3,055324          |
| 10        | 4,678283 | 3,025566          |
| 100       | 4,333929 | 1,374816          |
| 500       | 4,045357 | 0,567401          |
| 1000      | 3,874532 | 0,316263          |
| 1500      | 3,523548 | 0,134039          |
| 2000      | 3,223324 | 0,077653          |
| 2500      | 2,963092 | 0,057539          |
| 3000      | 2,927669 | 0,04723           |
| 3500      | 2,906451 | 0,040717          |
| 4000      | 2,566751 | 0,035315          |
| 4500      | 2,550943 | 0,031443          |
| 5000      | 2,539485 | 0,028615          |
| 6000      | 2,530225 | 0,023834          |
| 7000      | 2,522263 | 0,020596          |
| 8000      | 2,515119 | 0,018211          |
| 9000      | 2,502996 | 0,016202          |
| 10000     | 2,448071 | 0,014673          |
| 14977     | 2,056355 | 0,01              |
| 20000     | 1,800224 |                   |
| 25000     | 1,034644 |                   |
| 30000     | 0,176542 |                   |
| 35000     | 0,039947 |                   |
| 40000     | 0,017469 |                   |
| 43067     | 0,009997 |                   |

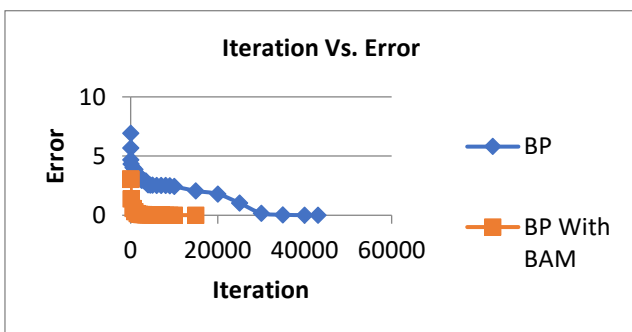


Fig. 10 Iterations Vs. Error (50%)

Comparing the performance of two networks as BPNN and hybrid neural network a decision had been taken that the hybrid neural network takes less iteration than BPNN in completion of the training process.

#### IV. CONCLUSION

Neural network-based road sign recognition holds immense potential in revolutionizing transportation systems by enhancing road safety and traffic management. The paper underscores the significance of neural networks in this domain and outlines the performances of BPNN and hybrid neural networks with experimental results. And the result shows that the hybrid neural network performs faster than BPNN with high recognition accuracy.

#### REFERENCES

- [1] Namyang, N. & Phimoltares, S. (2020). Thai traffic sign classification and recognition system based on histogram of gradients, color layout descriptor, and normalized correlation coefficient. *International Conference on Information Technology (InCIT), Chonburi, Thailand*, 270-275.
- [2] Soni, D., Chaurasiya, R.K. & Agrawal, S. (2019). Improving the Classification Accuracy of Accurate Traffic Sign Detection and Recognition System Using HOG and LBP Features and PCA-Based Dimension Reduction. *Proceedings of the International Conference on Sustainable Computing in Science, Technology and Management (SUSCOM), Amity University Rajasthan, Jaipur, India*.
- [3] Sapijaszko, G., Alobaidi, T. & Mikhael, W.B. (2019). Traffic sign recognition based on multilayer perceptron using DWT and DCT. *Proceedings of the 2019 IEEE 62nd International Midwest Symposium on Circuits and Systems (MWSCAS), Dallas, TX, USA*, 440-443.
- [4] Aziz, S. & Youssef, F. (2018). Traffic sign recognition based on multi-feature fusion and ELM classifier. *Procedia Computer Science*, 127, 146-153.
- [5] Wang, B. (2022). Research on the Optimal Machine Learning Classifier for Traffic Signs. *Web of Conferences; EDP Sciences: Les Ulis, France*, 144, 03014.
- [6] Shepherd, G. M. & Koch, C. (1990). Dendritic electrotonus and synaptic integration. *The Synaptic Organization of the Brained, G. M. Shepherd, Oxford University Press, appendix*.
- [7] Kosko, B. (1988). Bidirectional associative memories. *IEEE Transactions on Systems, Man, and Cybernetics*, 18(1), 49-60.
- [8] Saha, S.K., Chakraborty, D. & Bhuiyan, Md. Al.Amin (2012). Neural Network based Road Sign Recognition. *International Journal of Computer Applications*, 50, 35-41.

# Computational analysis of the transition of a system between two non-equilibrium stationary states through two-dimensional laminar natural convection in a cylindrical cavity

Herimiah Rakotondranja Stelarijao Eloi<sup>1</sup>, Raminosoa Andrianary Lala<sup>2</sup>, Ramanantsoa Ravo Mparany<sup>2</sup>, Randrianandraina Hery Zo<sup>2</sup>, Rakotomalala Minoson<sup>2</sup>, Razafinjato Victor Albert<sup>3</sup>

<sup>1</sup>Laboratoire de Thermodynamique Thermique et Combustion, University of Antananarivo

<sup>2</sup>Institut pour la Maitrise de l'Energie d'Antananarivo

<sup>3</sup>Institut Supérieur de Technologie d'Antananarivo

Received: 30 Nov 2023,

Receive in revised form: 02 Jan 2024,

Accepted: 10 Jan 2024,

Available online: 19 Jan 2024

©2024 The Author(s). Published by AI Publication. This is an open access article under the CC BY license (<https://creativecommons.org/licenses/by/4.0/>).

**Keywords**— *Natural convection, non-equilibrium stationary states, transient regime, cylindrical crescent, bi-cylindrical coordinates, laminar regime.*

**Abstract**— *Our work focuses on the numerical study of two-dimensional and transient natural convection in a fluid confined within a crescent-shaped space delimited by two horizontal cylinders. The upper wall is subjected to a non-uniform heat flux, while the lower wall experiences a uniform heat flux, thereby generating thermal natural convection. The transfer equations are solved in a bi-cylindrical coordinate system using the formalism of stream function and vorticity, and then integrated using the finite difference method. Subsequently, these transfer equations are integrated using S.V Patankar's finite difference method with an implicit scheme. The computational program is implemented using Maple V Release Student software. The discretization of the equations highlights the following parameters: the Prandtl number ( $Pr$ ), the modified Grashof number ( $Gr$ ), and the aspect ratio ( $r_2/r_1$ ). The Prandtl number is fixed at 0.7. The results include temperature distributions, local and average Nusselt values, as well as graphs illustrating variations in various parameters based on slice indices.*

## I. INTRODUCTION

Natural convection is a heat transfer mechanism that occurs exclusively within fluid mediums when there is a temperature gradient between two surfaces. This mechanism is the most significant mode of heat transfer and involves the description of fluid movement generated by Archimedean forces resulting from variations in density with temperature. Consequently, there is a coupling of dynamics and thermodynamics. The velocity field transports heat and, due to the temperature-dependent density, influences the distribution of mass; in turn,

changes in mass create movement through Archimedean buoyancy.

The study of natural convection phenomena captivates researchers due to its widespread applications in various natural phenomena and industrial processes, including the cooling of electronic and electrical components, thermal power plants, nuclear power plants, space heating, heat exchangers, aerospace applications, and even in the vicinity of the human body, among others.

This type of fluid flow is omnipresent in daily life and prevalent in almost all industrial environments. Numerous

studies have been conducted on natural convection, focusing on scenarios such as cylinders with walls subjected to uniform density flux [11] or maintained at constant temperatures [4, 22].

Rolland Aimé ANDRIAMAHENINA [8] conducted a study on transient laminar natural convection between two equilibrium states in a fluid confined within a flattened half-ellipsoid, with the wall subjected to a constant density flux.

All the aforementioned studies rely on a mathematical model based on the Boussinesq hypothesis and the two-dimensionality of the flow.

**II. MATHEMATICAL MODEL OF TRANSFER EQUATIONS AND NUMERICAL METHOD**

**Figure 1** illustrates the cross-section of a cylindrical crescent delimited by the intersection of two cylinders, while **Figure 2** depicts the schematic representation of bi-cylindrical coordinates according to [20].

We make the following simplifying assumptions:

- The lower wall is subjected to a uniform heat flux  $q_2$ , and the upper wall is traversed by a variable heat flux  $q$  [1].

$$q = \frac{(I_1 - I)N + 1}{I_1} q_2 \tag{1}$$

$N$ : slice index

$I_1$ : total length of the arc where the heat flux  $q$  is applied to the upper wall

$I$ : length of the arc where the heat flux  $q$  is applied to the upper wall

- The fluid is an ideal gas assumed to be incompressible.
- Viscous dissipation and radiation are considered negligible.
- The physical properties of the fluid are constant, except for its density  $\rho$ , which varies and gives rise to natural convection.
- The Boussinesq hypothesis, upon which the heat flux is applied, is valid.
- The convection is laminar and in a transient regime.

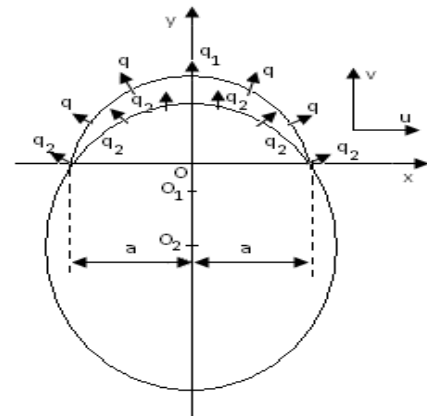


Fig. 1

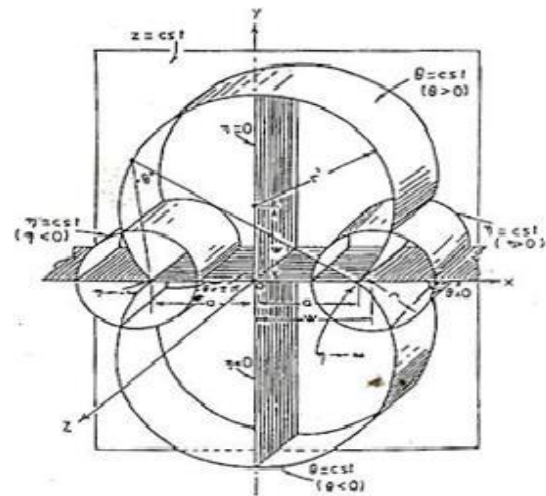


Fig. 2

**2.1 Formulation of equations**

By introducing vorticity and the stream function, the dimensionless transfer equations in bi-cylindrical coordinates can be expressed as follows:

- Continuity equation

$$\frac{\partial}{\partial \eta} (HV_{\eta}^+) + \frac{\partial}{\partial \theta} (HV_{\theta}^+) = 0 \tag{2}$$

- Momentum equation

$$\frac{\partial \omega^+}{\partial \tau^+} + \frac{V_{\eta}^+}{H} \frac{\partial \omega^+}{\partial \eta} + \frac{V_{\theta}^+}{H} \frac{\partial \omega^+}{\partial \theta} = \frac{1}{H} \left[ F(\eta, \theta) \frac{\partial T^+}{\partial \theta} + G(\eta, \theta) \frac{\partial T^+}{\partial \eta} \right] + \frac{1}{H^2} \left[ \frac{\partial^2 \omega^+}{\partial \eta^2} + \frac{\partial^2 \omega^+}{\partial \theta^2} \right] \tag{3}$$

- Heat Equation

$$\frac{\partial T^+}{\partial \eta} + \frac{V_{\eta}^+}{H} \frac{\partial T^+}{\partial \eta} + \frac{V_{\theta}^+}{H} \frac{\partial T^+}{\partial \theta} = \frac{1}{Pr H^2} \left[ \frac{\partial^2 T^+}{\partial \eta^2} + \frac{\partial^2 T^+}{\partial \theta^2} \right] \tag{4}$$

### 2.2 Boundary Conditions

The boundary conditions associated with the transfer equations on both walls are as follows:

- Lower wall (wall with index 2)

Conditions on velocities and flux:

$$\begin{cases} V_{\eta}^+ \Big|_{(\eta, \theta_2, t^+)} = 0 \\ V_{\theta}^+ \Big|_{(\eta, \theta_2, t^+)} = 0 \end{cases} \quad (5)$$

$$\frac{\partial \psi^+}{\partial \eta} \Big|_{(\eta, \theta_2, t^+)} = 0 \quad (6)$$

$$\frac{\partial T^+}{\partial \theta} \Big|_{(\eta, \theta_2, t^+)} = -q_2 \frac{Hg \beta D_H^4}{\lambda \nu^2} \quad (7)$$

- Upper wall (wall with index 1)

$$\begin{cases} V_{\eta}^+ \Big|_{(\eta, \theta_1, t^+)} = 0 \\ V_{\theta}^+ \Big|_{(\eta, \theta_1, t^+)} = 0 \end{cases} \quad (8)$$

$$\frac{\partial \psi^+}{\partial \eta} \Big|_{(\eta, \theta_1, t^+)} = 0 \quad (9)$$

$$\frac{\partial T^+}{\partial \theta} \Big|_{(\eta, \theta_1, t^+)} = -q \frac{Hg \beta D_H^4}{\lambda \nu^2} \quad (10)$$

### 2.3 Numerical method

We solved the system of transfer equations with associated boundary conditions using the "finite difference" method, which relies on TAYLOR series expansions approximating the values of derivatives at a point or in its vicinity through differences. To discretize the equations and boundary conditions, we chose the method developed by S.V. Patankar and Nogotov [6].

## III. RESULTS AND DISCUSSION

In our study, we selected air as the fluid, and its physical properties are provided at the initial temperature  $T_0 = 293$  K, corresponding to a Prandtl number  $Pr = 0.7$ . The values of physical constants are fixed as follows:

- Focal distance  $a = 0.12$  m.
- Heat flux density  $q_2 = 12$  W/m<sup>2</sup>, resulting in a Grashof number  $Gr = 10^6$ .
- All presented results are calculated based on the dimensionless time step of  $3.65 \times 10^{-4}$ .

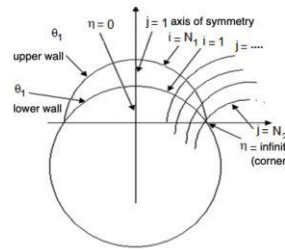


Fig. 3: Notation Representation.

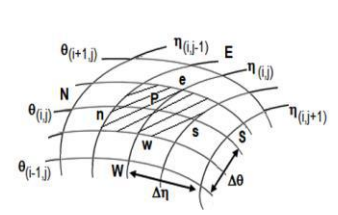


Fig. 4: Node representation in the mesh.

Figure 5 shows the radial variations of dimensionless tangential velocity as a function of the slice index  $\eta$ . Three distinct zones are observed over dimensionless time:

- Near the axis of symmetry ( $\eta = 0$ ), the particle velocity magnitude decreases rapidly and approaches zero, as the temperature is very low in this zone (20%);
- In the central zone (between 20% and 80%), the particle velocity magnitude is nearly uniform, following the geometric shape of the crescent, as there is no temperature variation in this range;
- Near the crescent tip, the particle velocity magnitude increases exponentially because the temperature is considerable in this region.

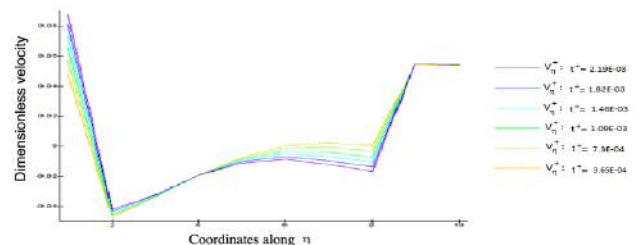


Fig. 5: Radial variations of dimensionless tangential velocity as a function of slice index  $\eta$  over dimensionless time.

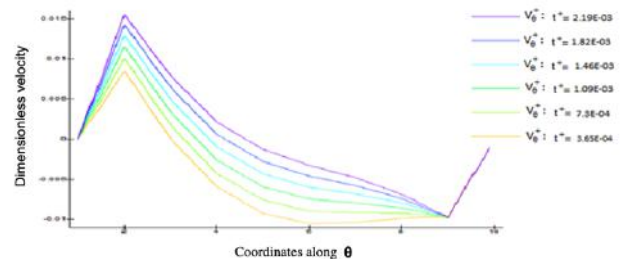


Fig. 6: Radial variations of dimensionless normal velocity as a function of slice index  $\theta$  over dimensionless time.

Figure 6 depicts the radial variations of dimensionless normal velocity as a function of the slice index  $\theta$ . The heat flux density through the wall affects the movement of fluid

particles, accelerating their velocity, especially when substantial.

The normal velocity curves exhibit alternations:

- Near the axis of symmetry (between 0–20%), an upward movement starting from zero velocity characterizes this range, with a predominance of normal velocity up to the upper part;
- Then a descent (between 20–90%) to the lower part;
- Reaching the lower part, fluid particles ascend, passing through zero normal velocity, and then the cyclic movement of fluid particles recommences.

These phenomena are interpreted by the fact that the movement and normal velocity of fluid particles are influenced by the variation of the variable heat flux density  $q$  imposed on the upper wall.

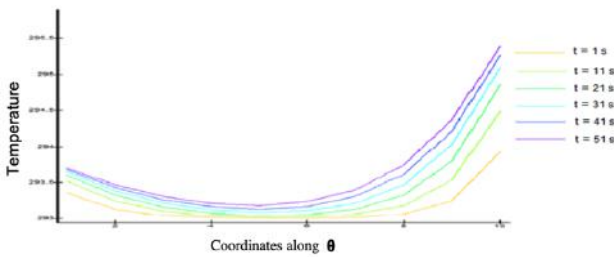


Fig. 7: Variation of real temperature as a function of slice index  $\theta$  over dimensionless time.

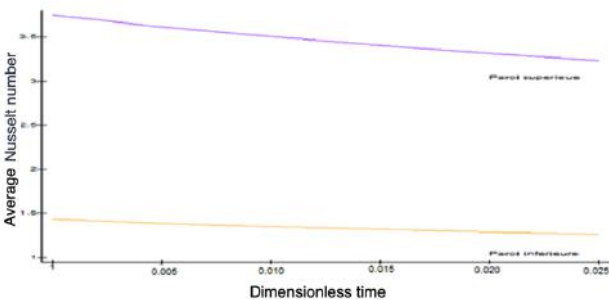


Fig. 8: Variation of the average Nusselt number as a function of dimensionless time.

**Figure 7** depicts the variations in real temperature as a function of the slice index  $\theta$ . It is observed that the temperature decreases slowly and levels off between 30–50%, indicating the existence of a steady-state regime in this zone. Temperatures reach their maximum values at the crescent tip, where temperature variations are substantial.

**Figure 8** shows the variations in the average Nusselt number as a function of dimensionless time. The average Nusselt number decreases as dimensionless time increases, indicating a reduction in the temperature gradient, i.e., the fluid temperature begins to approach that of the walls.

#### IV. CONCLUSION

We conducted a numerical study on the transition of a system between two non-equilibrium stationary states through two-dimensional laminar natural convection in a cylindrical crescent. The use of the finite difference method by S.V. Patankar [5] allows for the approximation of complex partial differential transfer equations to linear partial differential equations. The choice of the bi-cylindrical coordinate system is crucial and suitable for the crescent, given the geometric properties of the system. With the aid of computational tools where the program was executed, we obtained reliable and consistent results regarding radial and tangential velocities, temperature, and the average Nusselt number, in accordance with the adopted methods.

#### NOMENCLATURE

$a$ : focal distance [m]

$C_p$ : specific heat capacity of the fluid at constant pressure [J.kg.K<sup>-1</sup>]

$D_H$ : characteristic length scale defined by  $D_H = 2(r_2 - r_1)$  [m]

$g$ : acceleration due to gravity [m.s<sup>-2</sup>]

$F, G$ : functions defined in the momentum equation

$h$ : metric coefficient of the bi-cylindrical coordinate system [m]

$H$ : dimensionless value of  $h$

$P$ : pressure within the fluid [Pa]

$q, q_2$ : respective heat flow densities applied to the upper and lower walls [W.m<sup>-2</sup>]

$q^+$ : dimensionless heat flux density

$r_1, r_2$ : respective radii of cylinders ( $C_1$ ) and ( $C_2$ ) [m]

$T$ : fluid temperature [K]

$T^+$ : dimensionless fluid temperature

$T_1$ : temperature of the lower cylinder [K]

$T_2$ : temperature of the upper cylinder [K]

$\Delta T$ : temperature difference defined by  $\Delta T = T_2 - T_1$  [K]

$T'$ : temperature difference defined by  $T' = T - T_1$  [K]

$T_r$ : reference temperature [K]

$t$ : time [s]

$t^+$ : dimensionless time

$V_\eta, V_\theta$ : velocity components in the  $\eta$  and  $\theta$  directions [m.s<sup>-1</sup>]

$V_\eta^+, V_\theta^+$  : dimensionless velocity components in the  $\eta$  and  $\theta$  directions

$V^+$ : velocity vector with components ( $U, V, W$ ) [ $\text{m}\cdot\text{s}^{-1}$ ]

$X, Y, Z$ : Cartesian coordinates [ $\text{m}$ ]

$X^+$ : dimensionless coordinate defined by  $X^+ = X/D_H$

$\alpha$ : thermal diffusivity of the fluid  $\alpha = \lambda/\rho C_p$  [ $\text{m}^2\cdot\text{s}^{-1}$ ]

$\beta$ : coefficient of thermal expansion of the fluid at constant pressure, defined by

$$\beta = -\frac{1}{\rho} \left( \frac{\partial \rho}{\partial T} \right)_P \quad [\text{K}^{-1}]$$

$\lambda$ : thermal conductivity of the fluid [ $\text{W}\cdot\text{m}^{-1}\cdot\text{K}^{-1}$ ]

$\eta$ : kinematic viscosity of the fluid [ $\text{m}^2\cdot\text{s}^{-1}$ ]

$\rho$ : density of air [ $\text{kg}\cdot\text{m}^{-3}$ ]

$\omega$ : vorticity [ $\text{s}^{-1}$ ]

$\omega^+$ : dimensionless vorticity

$\eta, \theta, Z$ : components in bi-cylindrical coordinates

$\Psi$ : stream function [ $\text{m}^2\cdot\text{s}^{-1}$ ]

$\Psi^+$ : dimensionless stream function

Indices:

Upper Wall

Lower Wall

$E, W$ : East and West nodes, respectively

$N, S$ : North and South nodes, respectively

$e, w$ : East and West faces of the control volume, respectively

$n, s$ : North and South faces of the control volume, respectively

## REFERENCES

- [1] Amadou, D. (1992). *Contribution à l'étude de la convection naturelle thermique dans un fluide newtonien situé dans l'espace d'intersection de deux cylindres horizontaux* [Thesis, University of Perpignan, France].
- [2] Razafinjato, V. A. (1993). *Contribution à l'étude de la convection mixte entre deux cylindres excentrés horizontaux* [Thesis, University of Antananarivo, Madagascar].
- [3] Lee, J. H. (1984). *Contribution à l'étude de la convection naturelle thermique en régime laminaire transitoire dans un récipient cylindrique verticalement rempli de fluide newtonien* [Thesis, University of Perpignan, France].
- [4] Kuehn, T. H. (1976). *Natural convection heat transfer from a horizontal circular cylinder to surrounding cylindrical enclosure* [Thesis, University of Minnesota, USA].
- [5] Patankar, S. V. (1980). *Numerical heat transfer and fluid flow*. New York, NY: McGraw-Hill.
- [6] Nogotov, E. F. (1976). *Applications of Numerical Heat Transfer*. New York, NY: McGraw-Hill.
- [7] Randriamanarina, C. (1989). *Etude de convection naturelle laminaire à l'intérieur d'un ellipsoïde de révolution d'axe vertical dont la paroi est traversée par un flux de chaleur de densité constante* [Master's thesis, University of Antananarivo, Madagascar].
- [8] Rolland, A. A. (1997). *Contribution à l'étude de la convection naturelle en régime laminaire transitoire entre deux états d'équilibres à l'intérieur ellipsoïde aplati soumis à un flux de chaleur de densité constante* [Master's thesis, University of Antananarivo, Madagascar].
- [9] Poulikakos, D., & Bejan, A. (1983). Natural convection experiments in a triangular enclosure. *Journal of Heat Transfer*, 105, 652–655.
- [10] King, H. H. (1976). A Poisson Equation Solver for Rectangular or Annular Region. *International Journal for Numerical Methods in Engineering*, 10, 799-809.
- [11] Kassem, T. (1989). *Contribution à l'étude de la convection naturelle thermique entre deux cylindres excentrés horizontaux* [Thesis, Compiègne University of Technology, France].
- [12] Morsli, S. (2015). *Simulation numérique de la convection naturelle et la génération de l'entropie dans les cavités* [Thesis, Oran University of Sciences and Technology, Algeria].
- [13] Yousif, N. J. (1986). *Contribution à l'étude théorique de la convection naturelle thermique bidimensionnelle en régime laminaire transitoire dans un récipient cylindrique vertical à fond incliné et partiellement rempli* [Thesis, University of Poitiers, France].
- [14] Peixinho, J. (2004). *Contribution expérimentale à l'étude de la convection thermique en régime laminaire, transitoire et turbulent pour un fluide à seuil en écoulement dans une conduite* [Thesis, University of Henry Poincaré – Nancy 1, France].
- [15] Foucher, L. (1999). *Convection naturelle laminaire dans une cavité contenant un ou plusieurs plaques* [Thesis, Ecole Centrale Paris, France].
- [16] Khelifi Touhami, M. S. (2012). *Simulation numérique de la convection naturelle dans un bec de stockage de GNL* [Thesis, M'Hamed Bougara University, Algeria].
- [17] Li, Y. (2016). *Approches analytique et expérimentale de la convection naturelle en canal vertical. Application aux double-façades photovoltaïques* [Thesis, INSA Lyon, France].
- [18] Kalache, D. (1987). *Contribution à l'étude de la convection naturelle en cavité trapézoïdale chauffée par dessous* [Thesis, University of Poitiers, France].
- [19] David, D. (2010). *Etude expérimentale de la convection naturelle aux abords de parois contenant des matériaux à changement de phase* [Thesis, INSA Lyon, France].
- [20] Moon, P., & Spenser, D. E. (1961). *Field Theory Engineers*. Toronto, Canada: D. Van Nostrand Company, Ltd.

# Particle Swarm Algorithm Applied to Image Reconstruction on Multiphase Flows

B. C. B. N. Souza<sup>1</sup>, R. A. M. Junior<sup>2</sup>, M. G. Nascimento<sup>3</sup>, C. S. Gonçalves<sup>4</sup>, D. V. B. Siqueira<sup>5</sup>, R. A. Câmara<sup>6</sup>

<sup>1</sup>Departamento de Física – UFPB, UFPB Campus I, Cidade Universitária, S/N – João Pessoa, Paraíba, Brazil CEP: 58.051-900

<sup>2</sup>Departamento de Energias Alternativas Renováveis, CEAR – UFPB, UFPB Campus I, Cidade Universitária, S/N – João Pessoa, Paraíba, Brazil CEP: 58.051-900

<sup>3</sup>Departamento de Engenharia Civil e Ambiental – DECA – UFPB, UFPB Campus I, Cidade Universitária, S/N – João Pessoa, Paraíba, Brazil CEP: 58.051-900

<sup>4</sup>Departamento de Física – UFPB, UFPB Campus I, Cidade Universitária, S/N – João Pessoa, Paraíba, Brazil CEP: 58.051-900

<sup>5</sup>Departamento de Física – UFPB, UFPB Campus I, Cidade Universitária, S/N – João Pessoa, Paraíba, Brazil CEP: 58.051-900

<sup>6</sup>Centro de Energia Alternativa e Renováveis – CEAR – UFPB, UFPB Campus I, Cidade Universitária, S/N – João Pessoa, Paraíba, Brazil CEP: 58.051-900

Received: 29 Nov 2023,

Receive in revised form: 01 Jan 2024,

Accepted: 08 Jan 2024,

Available online: 19 Jan 2024

©2024 The Author(s). Published by AI Publication. This is an open access article under the CC BY license (<https://creativecommons.org/licenses/by/4.0/>)

**Keywords**—*Electrical tomography, finite elements, inverse problems, particle swarm optimization, parallel processing, multiphase systems.*

**Abstract** — *This work presents a methodology for reconstructing multiphase flow electrical capacitive tomography (ECT) images, using a particle swarm optimization (PSO) algorithm in the parallel processing paradigm. Intended is to improve the efficiency of the inverse problem algorithm in ECT, increasing the resolution of the reconstructed images, without necessarily increasing the processing time of these reconstruction technique. A limitation found is that, for inverse problem-type reconstruction techniques for ECT, the response of the sensor system is non-linear and, therefore, the processing time grows faster than any increase in resolution, imposing a high computational cost. For real-time applications, the first contribution is the removal of unnecessary processing from the usual code; the second is the creation of a new PSO algorithm for image reconstruction that is more efficient than normal. The new parallel processing routine present the physical principles of ECT, the heuristic algorithms used in the reconstruction process and the main concepts for parallel computing.*

## I. INTRODUCTION

Multiphase flows are often present in numerous industrial processes, particularly in food, chemical and petroleum industries and also in energy plants, among others (Thorn, Johansen and Hjertaker, 2013; Zainal-Mokhtar and Mohamad-Saleh, 2013; Cui et al, 2014; Mei et al, 2016). In the majority of these studied flows the dielectric nature of matter dominates, and consequently, the use of electrical capacitance tomography (ECT) is reinforced as one of the most advantageous tomographic method to obtain images from such industrial processes. In comparison to other tomographic techniques, ECT offers

some advantages, such as i) been non-radioactive, ii) non-invasive and non-intrusive, iii) cost effective, iv) non susceptible to adverse temperature and pressure conditions and v) relative fast response.

This technique is based on measurement of capacitance changes in dielectric distribution of the material present in the multiphase flow. Electrodes are placed around the flow pipe, usually 8 to 16, and the capacitance values across each pair are measured. Those capacitance measurements are then applied to an appropriate reconstruction algorithm which produces an image of the dielectric spatial

distribution and therefore the material across the sensor (Yang and Peng, 2003).

The ECT sensor is composed by a number of electrodes that can be made of a copper sheet placed around the flow pipe in a non-parallel way. Besides the capacitive sensor, there are also i) an electronic system of transduction to read a voltage signal which is proportional to the capacitance and between each pair of electrodes, and ii) a control and acquisition system that coordinates the multi-electrode measurements and converts the analog signal into the data to be used by the image reconstruction algorithm.

## II. METHOD

### 2.1 Forward and inverse problem of ECT

Due to its specific features, ECT is considered as a soft-field tomography. Therefore, the material to be imaged modifies the electric sensing field. Such effect is highly non-linear and the image reconstruction process becomes more complex in comparison to conventional x-ray tomography (Belo, 1999).

Image reconstruction using ECT is a two steps task: firstly, the forward problem should be solved, in other words, it is the determination, using the excitation data, of the electric potentials inside the domain and the respective response along the contour. Secondly, the inverse problem should then be solved, which is the determination of the dielectric distribution into the domain from the relation between excitation data and the boundary response.

#### Forward Problem Solution

The solution of the forward problem associated with ECT can be defined as the determination of the electric potential, and thus the capacitance between the electrodes, associated to a given dielectric distribution over the area of a cross section of the pipe in study.

If there are no free charges within the section of the imaged region, the relationship between the capacitance and permittivity distribution is modeled by Equation (1):

$$\vec{\nabla}[\varepsilon_0 \varepsilon(x, y) \vec{\nabla} \varphi(x, y)] = 0 \quad (1)$$

where  $(x, y) \in \Omega$  represents the space domain,  $\varepsilon_0$  is the vacuum absolute permittivity,  $\varepsilon(x, y)$  is the relative permittivity distribution of the material inside the imaged region,  $\varphi(x, y)$  is the electric potential and  $\Gamma$  is the closed curve enclosing the electrodes surrounding the region.

The boundary conditions are defined when an electrode is excited with a potential  $\varphi = V_0$  (source electrode) and all others are kept on ground level ( $\varphi = 0$ ). The measuring process is then multiplexed for each grounded electrode (sensing electrode) in order to obtain the respective

capacitance. Therefore, the potential distribution is expressed as

$$\varphi(x, y) = \begin{cases} V_0, & (x, y) \in \Omega_i \\ 0, & (x, y) \in \Omega_k, k \neq i \end{cases} \quad (2)$$

and for the capacitance we have

$$C = \frac{-\varepsilon_0}{V_c} \int_{\Gamma} \varepsilon(x, y) \vec{\nabla} \varphi(x, y) d\Omega \quad (3)$$

As long as there is not a general analytic solution for all configurations of permittivity distribution and electrodes excitation conditions, only particular solutions can be achieved for specific configurations. For example, numerical routines using finite element method (FEM) have been developed to determine the capacitance values from the permittivity distribution and excitation profile of electrodes surrounding a pipe (Souza, 2009).

FEM was chosen due to its versatility and robustness in dealing with complex geometries and inhomogeneous media and this is also the method implemented here to solve the forward problem.

#### Inverse Problem Solution

Solution of the inverse problem associated to ECT can be defined as the determination of the dielectric distribution over the area of a cross section of the pipe under analysis which is related to the capacitance values obtained by the sensor.

One method of accomplishing this is to compare estimated values obtained from a numerical model with experimental measurements from a capacitance sensor. Thus, the traditional tomography problem is moved to the minimization of an error functional. Such functional should be able to reflect the discrepancies between the experimental measurements values and numerically calculated values corresponding to changes in permittivity distribution inside the region to be imaged.

The optimization process consists in a search algorithm for the dielectric distribution that globally minimizes the error functional (Smolik, 2010). At initialization, the forward problem is solved for a given initial distribution which results in a numerical answer to the capacitance value that gives a new value to the error functional. If such value is smaller than the earlier value, then the former distribution is updated and this process will be iterated many times until a global minimum for the error functional is found. When the process ends the ultimate numerical result obtained should correspond to the distribution that most resembles to the actual permittivity distribution inside the sensor, in other words, an image of the sensor cross section is achieved.

When choosing a reconstruction algorithm, the main considerations that we should take into account are computational effort, speed and accuracy. Iterative



algorithms can increase accuracy but, on the other hand, may slow the rebuilding process. Image reconstruction process using iterative approach is time consuming, because it has to estimate the capacitance value by solving the forward problem many times, in an iterated fashion, thus becoming a low-speed reconstruction technique, one that cannot be applied to systems that require real-time images.

## 2.2 RECONSTRUCTION ALGORITHM

Unlike direct algorithms, the iterative algorithms are formulated in terms of an optimization problem, characterized by iterated attempts to minimize an error function between the capacitance values obtained by the theoretical solution of the forward problem and experimental capacitance values obtained by the system sensor. It is assumed as the solution of the inverse problem, the dielectric configuration that can minimize the error functional (Li, 2015).

### Particle Swarm Optimization

Particle Swarm Optimization (PSO) is a stochastic computational technique based on population dynamics. PSO has emerged from experiences developed by Kennedy and Eberhart (1995) with algorithms that model a social behavior from a set of individuals.

Likewise, other collective intelligence approaches, PSO is based on the skills of a population of individuals which are able to interact with each other and also the environment. Relying on the capabilities of self-evaluation, comparison and imitation, individuals are able to deal with a number of possible situations presented by the environment and therefore, global behaviors emerge from these interactions. The algorithm developed by Kennedy and Eberhart (1995) seeks the optimization of a fitness function using information exchanges among individuals (particles) and the whole population (swarm).

In order to achieve the optimal solution, each particle in PSO is treated as a point in  $R^n$  space and it represents a potential solution of the forward problem. Particle position is adjusted according to its own experience as well as group experience. Equation (4) corresponds to the sum of three distinct terms: the first one refers to the particle inertia; the second is a cognitive term related to particle individual learning of the best position it had already reached; the third is a social term that represents the experience exchange among all particles. In each iteration, the particle position is updated according to Equation (5) which considers its current position as well as a displacement given by the velocity due to iterating process.

$$v_i = wv_i + c_1r_1(p_{best} - x_i) + c_2r_2(g_{best} - x_i) \quad (4)$$

$$x_i = x_i + v_i \quad (5)$$

Where  $v_i$  is the particle  $i$  current velocity,  $w$  is an inertial weight that balances global and local exploration,  $c_1$  and  $c_2$  are behavior coefficients,  $r_1$  and  $r_2$  are random numbers between 0 and 1,  $p_{best}$  is the best position already reached by the particle and  $g_{best}$  is the best position found by the swarm.

Velocity update of particles depends on parameters that should be adjusted for each problem to be optimized, namely the inertial weight, cognitive and social terms. Inertial weight  $w$  allows broadness on the exploration space: high values improve global exploration. To the contrary, small values favor local exploration. In this work, the inertial weight has an update procedure (Equation 6) identical to what is described in Eberhart and Shi (2001), where  $w$  is adjusted linearly in the interval 0.4 to 0.9. Shi and Eberhart (1998) suggested to keep  $c_1 = c_2 = 2.0$  in order to balance social and cognitive behavior of the particle.

$$w = w_{max} - (w_{max} - w_{min}) \frac{(k-1)}{m} \quad (6)$$

Where  $k$  is the iteration number,  $m$  is the maximum iteration number,  $w_{max}$  and  $w_{min}$  are the maximum and minimum weight, respectively. The steps for implementing PSO algorithm are described in the Pseudocode 1 (Eberhart and Shi, 2001):

---

### Pseudocode 1. PSO algorithm

---

```

1 initialize constants  $m, n, c_1, c_2, w$ ;
2 randomly initialize  $n$  positions and velocities in the space  $R^n$ ;
3 for  $k \leftarrow 1$  to  $m$  do
4   for  $i \leftarrow 1$  to  $n$  do
5     solve forward problem for position  $i$ ;
6     evaluate fitness  $f(x_i)$ ;
7   end for
8   for  $i \leftarrow 1$  to  $n$  do
9     if  $f_k^i \leq f_p^i$  then
10       $f_p^i = f_k^i$ 
11       $p_{best} = x_k^i$ 
12    end if
13    if  $f_k^i \leq f_g$  then
14       $f_g = f_k^i$ 
15       $g_{best} = x_k^i$ 
16    end if
17  end for
18  update velocity according to Equation (4);
19  update position according to Equation (5);
20  update  $w$  according to Equation (6);
21 end for

```

**Result:** assume  $g_{best}$  as the problem solution;

---

Parallel algorithm implementation of PSO can be described as a master-slave paradigm (Schutte et al, 2004). The master processor (MP) creates a set of random initial positions in the space  $R^n$ , partitions this set into subsets and

sends them to have its fitness function analyzed by the slave processors (SPs). All decision processes are carried out by the MP, for instance, position and velocity update as well as the algorithm convergence control. SPs solve the forward problem and compare their results to the capacitance values obtained experimentally. Thus, for each position configuration the fitness function is evaluated and the resulting value is returned to the MP. MP and SPs tasks are described in Pseudocode 2.

### Pseudocode 2. Parallel PSO algorithm

```

1  if my_id = 0 then // I am the master
2    initialize constants iter_max, n, c_1, c_2, w;
3    randomly initialize n positions and velocities in the space R^n;
4  end if
5  for k ← 1 to iter_max do
6    if my_id = 0 then // I am the master
7      for target ← 1 to n_processors do
8        send position x_i of m particles to each slave
9      end for
10     for source ← 1 to n_processors do
11       receive position x_i of m particles from each slave;
12       receive fitness f(x_i) of m particles from each slave;
13     end for
14     perform barrier synchronization for all fitness evaluation results;
15     for i ← 1 to n do
16       if f_k^i ≤ f_p^i then
17         f_p^i = f_k^i
18         p_best = x_k^i
19       end if
20       if f_k^i ≤ f_g then
21         f_g = f_k^i
22         g_best = x_k^i
23       end if
24     end for
25     update velocity according to Equation (4);
26     update position according to Equation (5);
27     update w according to Equation (6);
28   else // I am a slave
29     receive position x_i of m particles from the master;
30     for i ← 1 to m do
31       solve forward problem for each x_i;
32       evaluate fitness f(x_i);
33     end for
34     send fitness f(x_i) of m particles back to the master;
35   end if
36 end for

```

**Result:** Assume  $g_{best}$  as the problem solution;

The initial steps of serial and parallel PSO algorithms are the same. Once the initialization step has been carried out by the MP, a package of  $m$  particles is sent to the SPs where the fitness function for each particle is evaluated.

Information exchange between MP and SPs is implemented using Message Passing Interface (MPI), a peer-to-peer communication library, as described in Singh (2012).

Parallel algorithm application aims to reduce processing time span from capacitance measurements (from sensor) to image reconstruction in comparison to serial algorithm.

Such reduction is attained by the distribution of forward problem solving to many processors.

## 2.3 EVALUATION OF ALGORITHMS BY SIMULATION

### Algorithm process

To analyze the spatial resolution obtained by the PSO algorithm applied to the ECT, we numerically simulated the response of a capacitive sensor with eight electrodes, with 3 different distributions of a two-phase mixture (oil-water): A core flow distribution, a homogeneous distribution of oil water containing bubbles and finally a stratified distribution.

Capacitance values were obtained from the direct problem solution for simulated values of permittivity, where they were contaminated with numerical noise in order to observe the impact of experimental error in the quality of the reconstructed image. The relative permittivity of the materials was admitted to be 4.1, 3.0 and 80.0, respectively for the acrylic pipe, oil and water contained within the pipe.

During the process of image reconstruction, a structured mesh was used, subdividing the region under study in two subregions – inner portion and pipe wall as can be seen in Figure 1a) and 1b). In order to avoid the “inverse crime” described in Wirgin (2004), we used a more refined mesh to compute the simulated capacitance values and a less refined mesh for the solution of the inverse problem.

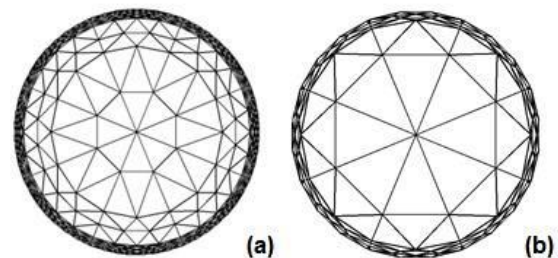


Fig.1. Discretization domain with (a) 128 elements and (b) 32 elements inside the pipe.

For the execution of the numerical routines, it was used a computer with an Intel® Core™ i7-4790, 16 GB of RAM, running Ubuntu operational system and GNU/Linux 64 bits kernel 15.10.

A cluster was assembled using a set of virtual machines on VirtualBox 4.1.8 running OpenMP protocol library.

The processing algorithm was coded in Fortran 90 language, using the GNU Fortran compiler. For pre- and post-processing, routines developed in Scilab language have been implemented.

**Evaluation criteria**

Two quality assessment methods were employed to evaluate the obtained images: qualitative and quantitative. The qualitative assessment involves visual comparisons of similarity for different reconstruction methods.

Reconstructed images obtained from the pipe section are also compared quantitatively using the following estimators:

- a) Normalized mean square error (NMSE):

$$\Delta \varepsilon = \frac{\sum_{i=1}^N (\varepsilon_i^{ref} - \varepsilon_i^{rec})^2}{\sum_{i=1}^N (\varepsilon_i^{ref} + \varepsilon_i^{rec})^2} \tag{7}$$

- b) Normalized absolute error – NAE:

$$\delta \varepsilon = \frac{\sum_{i=1}^N |\varepsilon_i^{ref} - \varepsilon_i^{rec}|}{\sum_{i=1}^N |\varepsilon_i^{ref}|} \tag{8}$$

- c) Correlation coefficient –  $R_{xy}$ :

$$R_{xy} = \frac{\sum_{i=1}^N (\varepsilon_i^{rec} - \bar{\varepsilon}^{rec})(\varepsilon_i^{ref} - \bar{\varepsilon}^{ref})}{\left[ \left( \sum_{i=1}^N (\varepsilon_i^{rec} - \bar{\varepsilon}^{rec})^2 \right) \left( \sum_{i=1}^N (\varepsilon_i^{ref} - \bar{\varepsilon}^{ref})^2 \right) \right]^{\frac{1}{2}}} \tag{9}$$

Where  $\varepsilon_i^{ref}$  and  $\varepsilon_i^{rec}$  are respectively the permittivity value of the element  $i$  for the reference dielectric distribution and reconstructed dielectric distribution by LBP algorithm and PSO, and  $\bar{\varepsilon}^{ref}$  and  $\bar{\varepsilon}^{rec}$  are their average values, respectively.

The best algorithm is the one with small values of  $\delta \varepsilon$  and  $\Delta \varepsilon$ , and values of  $R_{xy}$  close to unity. The normalized quadratic error is sensitive to large errors of some elements, while the normalized absolute error is sensitive to small errors on many factors, where the correlation coefficient indicates the spatial similarity between the reference image and the reconstructed image.

**III. RESULTS**

Images of the simulated flows profiles are shown on Figure 2. Those images should be compared with Figures 3, 4 and 5 for the qualitative evaluation of the results. Numerical noise of 3% and 5% were also added to the capacitance values in order to test the robustness of reconstruction algorithms.

In order to compare the quality of images obtained by the PSO algorithm, we employed linear back projection (LBP) algorithm as reference for the simulated flows shown on Figure 2. Based on the sensitivity matrix model, LBP is still the most cited reconstruction method and in its simplest implementation it presumes that the sensitivity matrix is invariant within the studied area (Li, 2015). All images were accomplished using a 5000 particles swarm and 500 iterations.

Numerical evaluation for the chosen estimators is listed on Tables 1, 2 and 3 for capacitance values without numerical noise, 3% and 5% of noise, respectively.

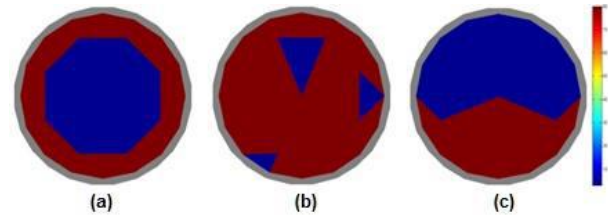


Fig.2. Dielectric simulated flow profiles: (a) core flow, (b) bubbles and (c) stratified.

Table 1. Error values  $\varepsilon$  related to the image reconstruction process without numerical noise.

| Flow Pattern | Method | NMSE (%) | NAE (%) | $R_{xy}$ |
|--------------|--------|----------|---------|----------|
| CORE         | LBP    | 57.90    | 56.97   | 92.96    |
|              | PSO    | 0.137    | 0.112   | 99.99    |
| BUBBLE       | LBP    | 103.5    | 125.6   | 22.89    |
|              | PSO    | 0.010    | 0.010   | 100.0    |
| STRATIFIED   | LBP    | 51.75    | 32.23   | 85.89    |
|              | PSO    | 2.842    | 1.883   | 99.96    |

Table 2. Error values  $\varepsilon$  related to the image reconstruction process with numerical noise of 3%.

| Flow Pattern | Method | NMSE (%) | NAE (%) | $R_{xy}$ |
|--------------|--------|----------|---------|----------|
| CORE         | LBP    | 59.134   | 58.560  | 91.836   |
|              | PSO    | 9.831    | 4.472   | 99.548   |
| BUBBLE       | LBP    | 102.462  | 123.595 | 22.653   |
|              | PSO    | 36.812   | 24.552  | 93.523   |
| STRATIFIED   | LBP    | 51.189   | 31.665  | 86.197   |
|              | PSO    | 6.281    | 3.400   | 99.815   |

Table 3. Error values  $\varepsilon$  related to the image reconstruction process with numerical noise of 5%.

| Flow Pattern | Method | NMSE (%) | NAE (%) | $R_{xy}$ |
|--------------|--------|----------|---------|----------|
| CORE         | LBP    | 62.440   | 64.772  | 90.778   |
|              | PSO    | 18.389   | 7.613   | 98.400   |
| BUBBLE       | LBP    | 102.998  | 122.218 | 21.327   |
|              | PSO    | 55.840   | 37.547  | 85.370   |
| STRATIFIED   | LBP    | 52.236   | 33.208  | 85.652   |
|              | PSO    | 9.856    | 5.542   | 99.547   |

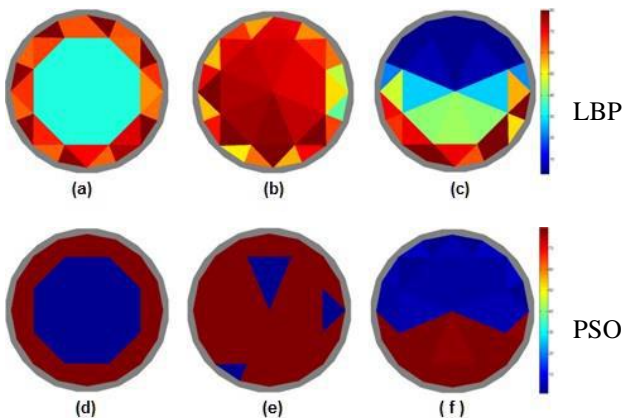


Figure 3. Reconstructed images from simulated values without numerical noise.

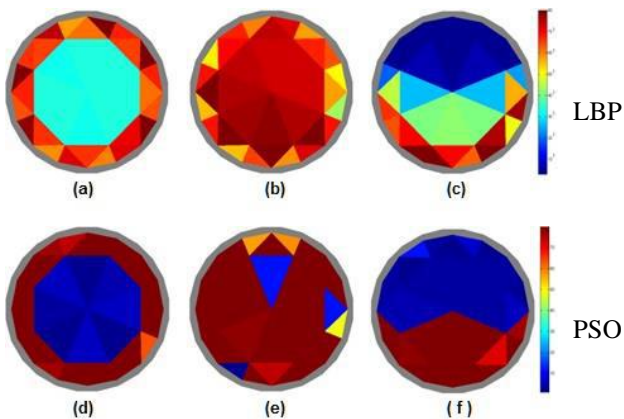


Figure 4. Reconstructed images from simulated values without numerical noise of 3%.

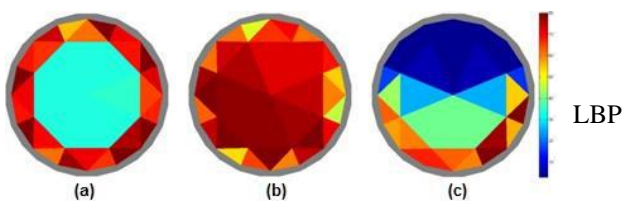


Fig.5. Reconstructed images from simulated values without numerical noise of 5%.

#### IV. DISCUSSION

PSO technique applied to ECT imaging has compelling results concerning its potentiality. Even in the presence of noise, it is possible to observe, not only visually but also by the quality indicators above, a good agreement between the proposed permittivity models and the accomplished results for the distinct flow patterns tested.

#### V. CONCLUSION

However, one of the main limitations of PSO technique is reached when the complexity of the optimization functional increases in conjunction with the amount of image pixels and, therefore, the number of parameters to be determined. This situation limits the maximum image resolution that can be achieved in real time applications. A possible solution is to grow the swarm size, which facilitates the determination of an optimal solution, but such approach is time consuming when a single processing unit is employed.

#### REFERENCES

- [1] BELO, F.A. AND MOURA, L.F.M. (1999). *A high frequency electronic transducer for multiphase flow measurements*, Journal of the Brazilian Society of Mechanical Sciences, 21(4), 611-621.
- [2] CUI, Z., YANG, C., SUN, B. AND WANG, X. (2014). *Liquid Film Thickness Estimation using Electrical Capacitance Tomography*. Measurement Science Review, 14(1), pp. 8-15.
- [3] EBERHART, R.C. AND SHI, Y. (2001). *Particle swarm optimization: developments, applications and resources*, in Proceedings of the Congress on Evolutionary Computation 2001 (CEC '01), Seoul, Korea. Piscataway, NJ: IEEE Service Center, pp. 81-86.
- [4] KENNEDY, J. AND EBERHART, R.C. (1995). *Particle swarm optimization*. Proc. IEEE Int'l. Conf. on Neural Networks, IV, Piscataway, NJ: IEEE Service Center. pp. 1942-1948.
- [5] LI, KEZHI, (2015). *A Brief Survey of Image Processing Algorithms in Electrical Capacitance Tomography*, CoRR, arXiv preprint arXiv:1510.04585.
- [6] MEI, I.L.S., ISMAIL, I., SHAFQUET, A. AND ABDULLAH, B. (2016). *Real-time monitoring and*

- measurement of wax deposition in pipelines via non-invasive electrical capacitance tomography*, Measurement Science and Technology, 27(2), pp. 25403-25413.
- [7] SCHUTTE, J. F., REINBOLT, J. A., FREGLY, B. J., HAFTKA, R. T. AND GEORGE, A. D. (2004). *Parallel global optimization with the particle swarm algorithm*, International journal for numerical methods in engineering, 61(13), p. 2296.
- [8] SHI, Y. AND EBERHART, R.C. (1998). *Parameter selection in particle swarm optimization*. In Evolutionary Programming VII: Proc. EP98, New York: Springer-Verlag, pp. 591-600.
- [9] SINGH, N. (2012). *Parallel Astronomical Data Processing or How to Build a Beowulf Class Cluster for High Performance Computing?* Centre for Astronomy, School of Physics National University of Ireland, Galway.
- [10] SMOLIK, W. T. (2010). *Accelerated Levenberg-Marquardt method with an optimal step length in electrical capacitance tomography*, International Conference on Imaging Systems and Techniques, IEEE, pp. 204-209.
- [11] SOUZA, B. C. B. N. (2009). *Resolução do problema direto da técnica de reconstrução de imagens via tomografia capacitiva elétrica aplicada ao estudo de sistemas multifásicos*, Dissertação de Mestrado, UFPB, João Pessoa-PB.
- [12] THORN, R., JOHANSEN, G. A. AND HJERTAKER, B. T. (2013). *Three-phase flow measurement in the petroleum industry*, Meas. Sci. Technol., vol. 24, no. 1, pp. 012003.
- [13] WIRGIN, A (2004). *The inverse crime*, arXiv preprint math-ph/0401050.
- [14] YANG, W.Q. AND PENG, L. (2003). *Image reconstruction algorithms for electrical capacitance tomography*, Meas. Sci. Tech. 14, 2003, pp. 1-13.
- [15] ZAINAL-MOKHTAR, K. AND MOHAMAD-SALEH, J. (2013). *An Oil Fraction Neural Sensor Developed Using Electrical Capacitance Tomography Sensor Data*. Sensors 13, no. 9: pp. 11385-11406.

# Effect of Calcium Carbonate on the Properties of Acid Soluble Cement Slurry

Catherine Ijeoma Miete-Ileberi<sup>1</sup>, John Vitus Anaele<sup>2</sup>, Samuel Mofunlewi<sup>3</sup>

<sup>1</sup>Department of Chemical Engineering, University of Port Harcourt, Nigeria

Email: mieteileberijeoma@gmail.com

<sup>2</sup>Department of Chemical Engineering, University of Port Harcourt, Nigeria

Email : john.anaele@uniport.edu.ng

<sup>3</sup>World Bank Africa Centre of Excellence in Oilfield Chemicals Research, University of Port Harcourt, Nigeria

Email: samuel.mofunlewi@aceuniport.org

Received: 01 Dec 2023,

Receive in revised form: 04 Jan 2024,

Accepted: 15 Jan 2024,

Available online: 22 Jan 2024

©2024 The Author(s). Published by AI  
Publication. This is an open access article  
under the CC BY license

[\(https://creativecommons.org/licenses/by/4.0/\)](https://creativecommons.org/licenses/by/4.0/)

**Keywords—** Plug cement, Acid soluble cement, Calcium carbonate, thickening time, Compressive strength.

**Abstract—** Cementation process in oil well drilling can be challenging, causing serious well control issues. The properties of cement slurry aid the designer to know the accurate dynamic placement of the cement slurry from surface to downhole of the wellbore. It presents the stability of locally sourced  $\text{CaCO}_3$  and class G cement slurry blend, giving insight to the effective pumpability and setting time for better slurry placement. Utilization of locally source recipes serving as an alternative use to imported additives in the reduction of oilfield cementation operations is imperative, considering the cost of imported chemicals. In this paper, fine  $\text{CaCO}_3$  identified as an acid-soluble additive was used for the design and formulation of a plug cementation operation through coil tubing for zonal isolations. Four different blends of  $\text{CaCO}_3$  containing 20%, 25% 30%, 40% BWOC and 100% Class 'G' cement used for the experiment at a test temperature of 175degree F BHST and a slurry density of 15.8ppg to ascertain the impact of  $\text{CaCO}_3$  on the mixability, pumpability, stability on the cement slurry. The placement time and strength data of cement slurry is very crucial to meeting planned cementing schedule. From the thickening time evaluation, at 40BC an average range of 8hrs-11hrs pumpable time was deduced for all blends. However, the point of departure for 30%  $\text{CaCO}_3$  BWOC showed a better result. The result helped to provide real-time information about the initial compressive strength development in the slurry specimen and this aids in determining waiting on cement time (WOC). It indicates that the more calcium carbonate in the system, the lesser the strength which means that the presence of calcium carbonate reduces the compressive strength in an acid-soluble cement slurry compared to the neat slurry. The paper presents experimental details on the average wait on cement time and the pumpable time for acid soluble cement slurry, contributing to data gathering and proper well planning before execution and. competency in the use of the slurry designs have been established in this work.

## I. INTRODUCTION

Cementing an oil well may be challenging and lead to major well control concerns owing to the high chance of fluid loss during the operation. This might make the cementing process more expensive than necessary. Remedial cementing, also known as secondary cementing, is carried out if there is a concern about the well's performance throughout any stage of its life cycle, including construction, stimulation, production, and abandonment. This is done to mitigate problems that are associated with primary cement. [9,19, 20, 15]

The remedial cement operation is categorized into two broad categories known as squeeze cementing and plug cementing. The plug cement is the placement of certain volume of slurry into the wellbore leaving it to set. It can be temporary or permanent plug within a cased or open hole section purposefully as a sealant to lost circulation zone, seal-off zones that have depleted over time, during directional drilling operation, as an anchor for well testing in open hole and as an isolation for wells abandonment. Acid soluble cement slurry used as a plug cement requires as much technical, engineering, and operational experience to enable adequate planning and risk assessment to cement placement. Therefore, accurate knowledge of its properties is imperative. [11, 12, 13, 14]

On the topic "A study of acid cement reactions using the rotating disk apparatus" found out that class G cement can be used to prepare cement plugs for sectional isolation and how acids react with the remedial cement plugs [18]. The objective of the work was to understand the nature of the reaction of class G cement plugs with the various acid types to mitigate the instability of plug placement during primary squeeze cementation. From the analytical procedure, the class G cement used was Saudi class G and inductively coupled plasma emission spectroscopy (ICP) was used to analyze the number of different cations (Aluminum, Iron, Calcium,) present in the class G cement then the rotating disk apparatus was used to react the cement plug with various acids for dissolution in a dynamic condition.

The work "Low-density acid removable cement as a solution for lost circulation across producing formation" confirmed the use of lightweight acid soluble slurry as a plugback cement to cut off "barefoot" (open hole) horizontal segment of a producing well-bore. Implementation of this type of plug cement that is in accordance with oil well cement parameters was done in the Middle East where it was applied as a lost circulation cement for the temporary plug to strengthen the wellbore environment and enable drilling with reduced effect of well control challenges.

In the journal "particle size distribution acid-soluble Cement instituted that a multi-modal particle size distribution cement design was used to achieve the required acid-soluble slurry and set cement properties owing to the fact that the cemented laterals with its numerous advantages still have increased wellbore friction pressure during stimulation resulting to damages.[10]

Considering the minimal pressure required (6500psi as highest-pressure difference between plugs) for placement operation, in "Successful Application of acid-soluble plugs in open hole slotted-liner completion" studied and surveyed several plugs. [23] In the bit to assuage well control issues resulting from huge losses when closed hole circulation drilling techniques (CHCD) is deployed with 5½" liner and cemented with primary cement for wellbore stability, this has been intricately seen unsafe therefore, open-hole slotted-liner with pre-installed acid-soluble cement (ASC) slurry was evaluated and considered fit for purpose for well completion procedure at the reservoir section in the work. The acid soluble plug used was magnesium-based cement plug where the permeability of the producing zone can be reinstated with an acidizing process. The ASC was characterized by the following properties: low permeability rate to alley losses, good compressive strength for wellbore stability, exhibits thermal expansion, 100% dissolvable in 15% HCl acid to enhance well productivity, non-contamination with drilling fluids or completions fluids and easily drilled out [16]. The benefit of the study indicated an increase in well production as possible producing zone damage and partial perforation skin effect is reduced, the time and cost required for commission operation are mitigated using the open-hole slotted-liner with dissolvable cement (ASC) and lastly eliminating perforation operation issues (lose of gun in the wellbore).

Conventional Portland cement with a blend of various sized calcium carbonate and magnesium oxychloride cement were the two types of acid-soluble cement slurries in "Detailed Laboratory Experiment of Acid Solubilized Cements as Remedy for Missing Circulation from across Producing Zones." [6] This analytical investigation established stable rheological properties with densities of 13ppg to 15.8ppg (pound per gallon) at 300% CaCO<sub>3</sub> bwoc also, lower compressive strength property with increase in the quantity of CaCO<sub>3</sub> in the conventional Portland cement-based system due to lower cementitious or binder additive was established but the acid dissolution was not 100% nevertheless, the magnesium oxychloride cement (MOC) type showed complete acid dissolution.

In the work "Low-density acid removable cement as a solution for lost circulation across producing formation"

confirmed the use of lightweight acid soluble slurry as a plugback cement to cut off “barefoot” (open hole) horizontal segment of a producing well-bore [5]. Implementation of this type of plug cement that is in accordance with oil well cement parameters was done in the Middle East where it was applied as a lost circulation cement for the temporary plug to strengthen the wellbore environment and enable drilling with reduced effect of well control challenges. It was also introduced to kill and abandon problematic well however, enable re-entering of the well after acidizing the abandoned zone [17]. This work identified that adjustments can be made to the cement type such as its density, thickening time, compressive strength properties, and bonding strength to suit the oil well specification for plug jobs as zonal isolation.

The bulk of the existing literature reviews have taken a quantitative approach and therefore, there is a need for a qualitative approach to the topic. Although some studies have examined different types of acid-soluble cement slurry, the research gaps limit our understanding of how calcium carbonate obtained in Nigeria can impact the properties of a plug acid-soluble cement. There is a lack of research on locally sourced calcium carbonate effect on the properties of acid-soluble cement slurry on its stability in the wellbore deployed to optimize placement time and tensile strength. Therefore, this study aims to analyze the impact calcium carbonate will have on acid-soluble cement slurry properties such as the thickening time, and the compressive strength. All these properties determine the placement time and the stability of the cement slurry in the wellbore when faced with the challenge of curing a lost circulation problem [8]. It will also increase the competency level on the subject.

**II. MATERIAL AND METHODS**

This analytical study is centered on describing and evaluating the effect of calcium carbonate on the properties of an Acid soluble cement slurry. Description of the materials and equipment in the experimental study used in achieving the objective of this study is stated below. [1, 2, 4, 7]

**2.1 Materials**

- Mixer
- Atmospheric Consistometer
- Pressurized consistometer
- FANN – 35 Rotational viscometers for Rheology
- Fluid loss equipment

- Free Water separation
- Ultrasonic cement analyzer (UCA)

**2.2 Additives**

- i. Class G cement
- ii. Calcium carbonate fine
- iii. Deformer
- iv. Friction reducer
- v. Fluid loss additive (a synthetic co-polymer)
- vi. Fluid loss additive (a synthetic polymer)
- vii. Retarder
- viii. Freshwater

**2.3 Cement Slurry Formulation**

From Table 2.3 below the slurry was designed and formulated with various ratios of locally sourced CaCO<sub>3</sub> mixed with conventional Portland cement to generate Acid soluble cement slurry (ASC) which was homogenously mixed, conditioned to the test temperature of 175degree F to obtain the thickening time and compressive strength properties.

*Table 2.3 Recipe of Acid soluble cement slurry*

| MATERIAL                               | CONCENTRATION              |
|--|----------------------------|
| Dyckerhoff Class G                     | Varied (80,75, 70, 60,100) |
| Calcium Carbonate (CaCO <sub>3</sub> ) | Varied (20, 25, 30, 40, 0) |
| Dispersant                             | 0.3%BWOC                   |
| Fluid Loss Additive (Polymer)          | 0.5%BWOC                   |
| Fluid Loss Additive (Co-Polymer)       | 0.5%BWOC                   |
| Retarder                               | 0.15%BWOC                  |
| Defoamer                               | 0.05gps                    |
| Fresh Water                            | 41.67 L/100kg              |

**2.4 Methods**

The experimental work was carried out in a cement laboratory, so results will be subject to ambient weather conditions during the experimental work.

This section gives the detailed procedure of equipment usage, slurry conditioning procedure, thickening time



procedure and ultrasonic compressive strength procedure of the slurry design.

#### 2.4.1 Weighing

The weighing scale was used to measure the design recipes. This helps to keep tabs on the accurate amount of the recipe needed for preparation of the product.[3]



Fig.2.1 Weighing Scale

#### 2.4.2 Mixing

After measuring the additives, a warring blender as shown in fig 2.1 below was used to mix a homogeneous slurry. Mixing of the additives required following the right mixing order as follows: Water, deformer, friction reducer, fluid loss additives, retarder, and a mixed blend of cement and calcium carbonate in their ratios,

Turning the blender to 4000 rpm while adding the additives, and then turning the blender speed to 12,000 rpm for 30seconds makes a cement slurry that is ready to be conditioned. [3, 4 ,7]



Fig.2.2 Fann Model 7000 Mixer

#### 2.4.3 Thickening Time Test Procedure

This test evaluates the time at which the slurry sets, and the HTHP consistometer is used for the test. The cement slurry was conditioned to the BHST in the atmospheric consistometer shown in fig 2.3 then placed into the pressurized consistometer as shown in fig 2.4 to determine the

thickening time of the slurry for the various blend ratios [24, 25]. The following procedures are followed for the evaluation: All parts of the assembly cup are gathered; the cup thread is greased.

and correctly coupled, then the slurry was poured in, and the hexagonal plug (pivot bearing) screws the cap tightly and excess air and slurry is removed. Place the slurry cup into the pressurized consistometer. Start within 5 minutes, by turning on the motor and the drive table rotates the slurry cup at 150 rpm. The potentiometer is placed on the rotating slurry cup, aligning the slots in the potentiometer with the inside of the cylinder and the bar drive is engaged and all set-ups of the test are carried out according to recommended practice. Input the test parameters into the computer software to perform the test to the testing temperature, pressure and Ramp time as the heater and timer are switched on to start data acquisition. After the test result was obtained, the controller/ software was turned off and result generated, the chamber was allowed to cool and the consistometer was open to remove and clean the potentiometer with WD-40 solvent. Slurry cup was disassembled, and all components cleaned.



Fig.2.3 Atmospheric Consistometer



Fig.2.4 Pressurized Consistometer



Fig.2.5 Parts of the pressurized consistometer

2.4.4 Ultrasonic Cement Analyzer (UCA) test procedure

The test is done to analyze the slurry strength. It is the ultrasonic strength of the slurry when spotted in the wellbore [21]. The following procedures were taken for the testing. The conditioned cement slurry was filled into the cell to the level gauge and the transducers coated with ultrasonic couplants (gels). O-rings were inspected for damage to ensure no pressure loss. All the algorithms for the cement density and design are selected in the computer software. Then the equipment is pressurized to 3000psi for the transit signal. During a typical cure, temperature and pressure are applied beginning with the recording of the transit time and ending when the test is completed. After a result has been obtained, the machinery is shut down, dismantled, and cleaned.



Fig.3.8 Ultrasonic Cement Analyzer

III. RESULTS AND DISCUSSIONS

The following results are discussed below in accordance with the slurry properties considered in this work.

3.1 Thickening Time

Each combination of acid-soluble cement and plain cement was tested for how long the resulting slurry could remain liquid under downhole conditions and pump effectively to the wellbore using a procedure called the thickening time test. This placement time which is very crucial should be simulated to meet the planned cementing schedule as possible. Typically for a batch-mixed cement job where a liner hanger is used, the periods that make up pumpable cement are the slurry batch mixing time, pump time, liner plug release time, displacement time, liner hanger setting time, circulation or reverse out time, and safety margin of 2hours. Therefore, the minimum thickening time is engineered to consider all of this to optimize good slurry design and planning. The thickening time chart from Figure 3.1- Figure 3.5 was summarized in Table 3.1 of the acid-soluble cement slurry showing a time range of 8 hours to 11 hours, indicating longer setting time. This placement time which is very crucial should be simulated to meet the planned cementing schedule as possible. The ratio of 30/70 showed good PoD (point of departure). The right data development and competency in the use of these slurry designs have been established in this work.

Table 3.1 Thickening time Evaluation (BHCT: 175°F, BHP: 6400psi, Heating Time: 48Mins)

|       | 20/80 Ratio | 25/75 Ratio | 30/70 Ratio | 40/60 Ratio | 100% Cement |
|-------|-------------|-------------|-------------|-------------|-------------|
|       | (HH:MM)     | (HH:MM)     | (HH:MM)     | (HH:MM)     | (HH:MM)     |
| 30Bc  | 09:20       | 08:40       | 07:39       | 08:08       | 10:59       |
| 40Bc  | 09:28       | 08:47       | 07:48       | 08:09       | 11:02       |
| 50Bc  | 09:34       | 09:17       | 07:52       | 08:11       | 11:25       |
| 70Bc  | 09:59       | 09:22       | 08:17       | 08:13       | 11:28       |
| 100Bc | 10:05       | 09:25       | 08:20       | 09:02       | 11:29       |

3.1.1 Thickening Time Charts for all blends of slurries

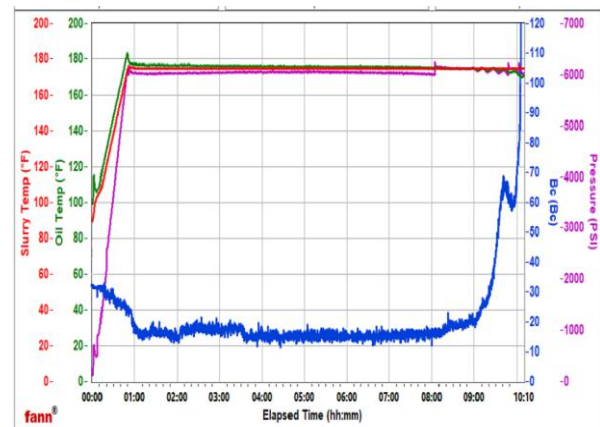


Fig.3.1 Thickening time for blend mixture 20/80

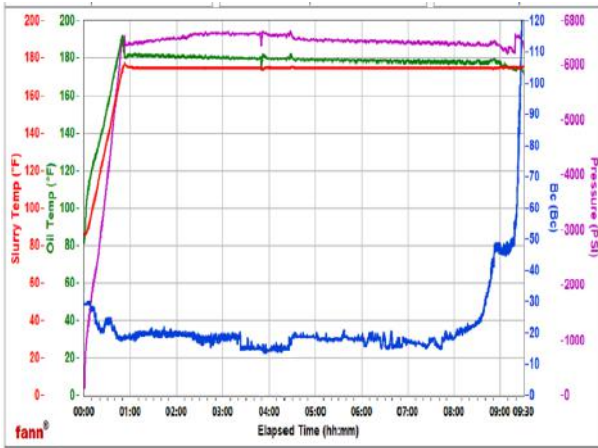


Fig.3.2 Thickening time for blend mixture 25/75

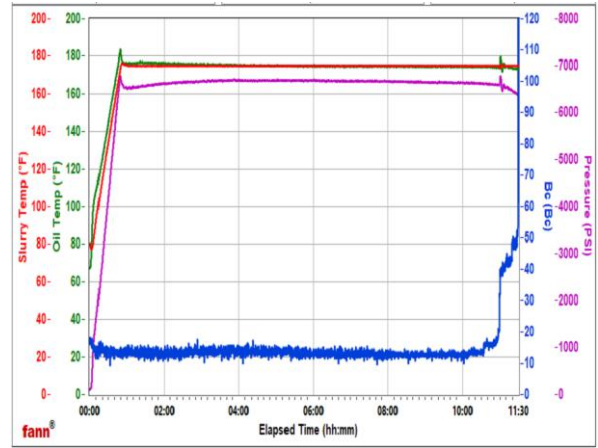


Fig.3.5 Thickening time for 100% cement

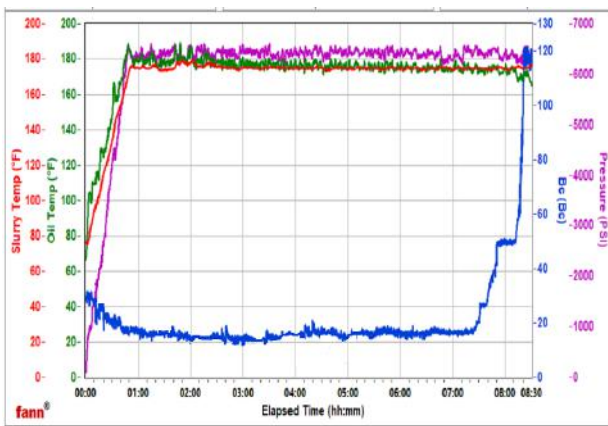


Fig.3.3 Thickening time for blend mixture 30/70

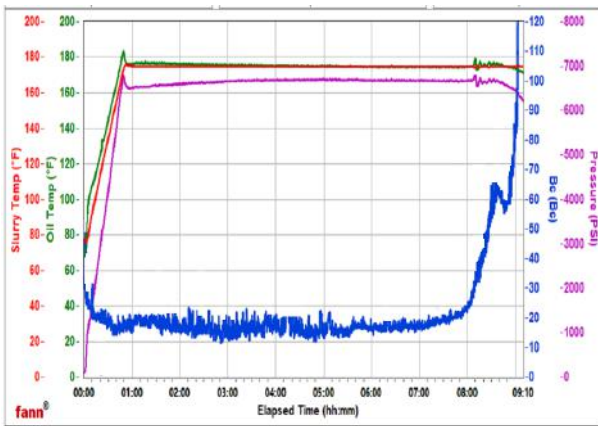


Fig.3.4 Thickening time for blend mixture 40/60

### 3.2 Compressive Strength (UCA)

Ultrasonic cement analyzer (UCA), a non-destructive test type for compressive strength of cement slurry measures and records the inverse P-wave of the velocity through the slurry as a function of time. After the conditioned slurry was inserted into the testing equipment, the cement bond log was calibrated by calculating the attenuation time using the sonic time plot shown in Fig 3.6 – Fig 3.1.0. The result helped to provide real-time information about the initial compressive strength development in the slurry specimen and this aids in determining waiting on cement time (WOC). The compressive strength which provides the strength data of the slurry under downhole conditions was evaluated and the sustained compressive strength reading was taken as shown in Table 3.5, and as a summary of all the design specimens in Fig 3.6 to Fig 3.1.0. indicates that the more calcium carbonate in the system the lesser the strength which means that the presence of calcium carbonate reduces the compressive strength in an acid-soluble cement slurry. it is important to note that the slurries designed in this work using locally sourced additive fit for purpose for a plug cement operation depending on well parameters that need longer timing as the strength development of the slurries at 50psi and 500psi was within a range of 9hrs-10hrs. Standard authorities adhere to compressive strength for a cementing process as follows: 50 to 200psi is adequate to support casing, 500psi is adequate for cement drill-out, 1000psi for perforation, 2000psi for stimulation of wellbore and the sidetracking job should have a pressure more than adjacent formation[22]. The experimental details obtained can contribute to data gathering and proper well planning before execution.

Table 3.2 UCA test Evaluation

|                | 20/80<br>Ratio | 25/75<br>Ratio | 30/70<br>Ratio | 40/60<br>Ratio | 100%<br>Cement |
|----------------|----------------|----------------|----------------|----------------|----------------|
| 50psi (hh:mm)  | 09:22          | 10:01          | 09:27          | 09:56          | 07:36          |
| 500psi (hh:mm) | 10:44          | 11:31          | 10:52          | 11:40          | 08:34          |
| 12hr CS (psi)  | 850            | 630            | 837            | 577            | 1184           |
| 24hr CS (psi)  | 1748           | 1456           | 1831           | 1411           | 1868           |

3.2.1 UCA- Compressive Strength Charts

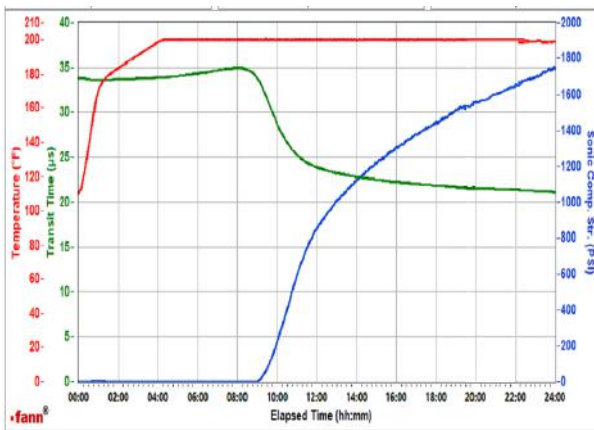


Fig.3.6 Compressive Strength for blend mixture 20/80

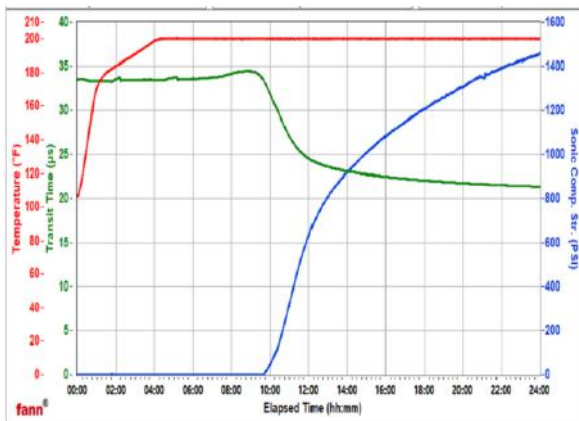


Fig.3.7 Compressive Strength for blend mixture 25/75

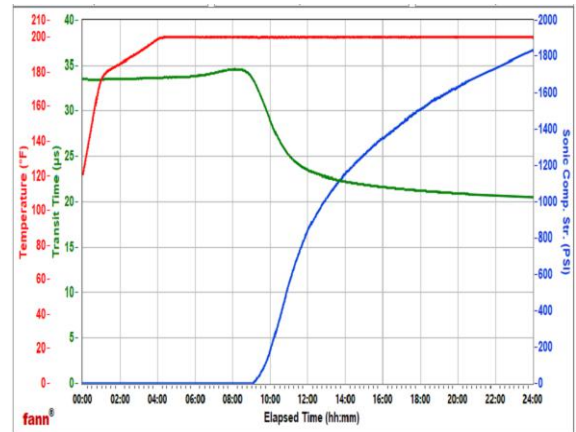


Fig.3.8 Compressive Strength for blend mixture 30/70

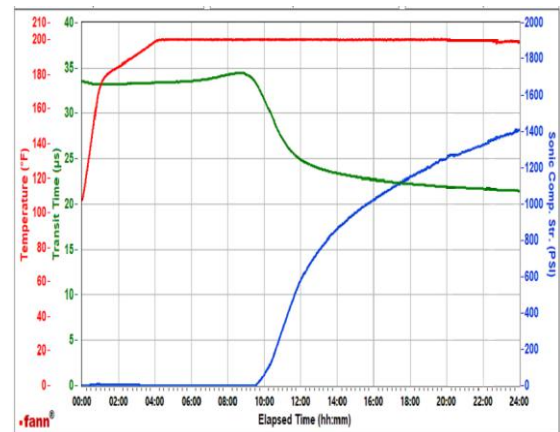


Fig.3.9 Compressive Strength for blend mixture 40/60

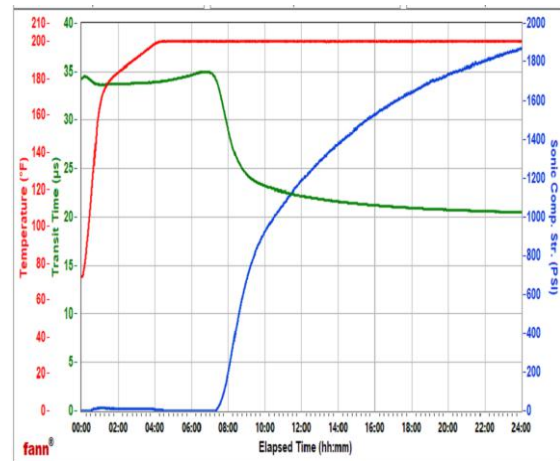


Fig.3.1.0 Compressive Strength for 100% Cement

IV. CONCLUSION AND RECOMMENDATION

4.1 Conclusion

Materials such as fluid loss additives, viscosifier, retarder, deformer, dispersant, cement, and locally sourced fine calcium carbonate needed for the experiment were identified for successful analysis. The concentrations of

the additives were formulated to give a stable designed slurry. Calcium carbonate of varying ratios (0, 20, 25, 30, and 40%) BWOC were analyzed. From the analysis, it was deduced that 30% calcium carbonate by weight of cement gave the optimum thickening time (TT) and compressive strength. This is because the point of departure for TT and the wait on cement (WOC) time was better than other ratios used in this work.

#### 4.2 Recommendation

The downhole temperature for production zone is typically between 145°F to 190°F. This research was conducted at 175°F. Hence, it is recommended to conduct further research at temperatures below and above 175°F to increase data gathering and proper well design and execution.

#### ACKNOWLEDGEMENT

The authors would like to appreciate the support of Halliburton Fluids laboratory and Baker Hughes cementing professionals in Nigeria. The Authors would also like to appreciate the University of Port Harcourt and Prof. Joel Ogbonna of the World Bank Center of Excellence in Oilfield Chemicals Research for their guidance to the successful completion of this experimental research.

#### REFERENCES

- [1] Abbas, G., Irawan, S., Kumar, S., Memon, K. R., & Khalwar, S. A. (2014). Characteristics of Oil Well Cement Slurry using Hydroxypropylmethylcellulose. *Journal of Applied Sciences*, 14(11), 1154–1160. <https://doi.org/10.3923/jas.2014.1154.1160>
- [2] Al-Yami, A., Ramasamy, J., & Wagle, V. (2017). Chemical Additives for Oil Well Cementing. *HAL (Le Centre Pour La Communication Scientifique Directe)*. <https://hal.archives-ouvertes.fr/hal-03796371>
- [3] Anaele, J.V., Joel, O.F., Chukwuma, F.O. and Otaraku, I.J. (2019) Alternative Utilization of Sawdust for Oilfield Chemical Additive (Cement Retarder) Production: A Case Study of Local Cement. *International Journal of Science and Engineering Investigations (IJSEI)*, 8(85): 33-37
- [4] API. 2010. API 10A. Specification for cement and materials for well cementing, 24<sup>th</sup> edn. American Petroleum Institute, Washington, DC
- [5] Bour D., Vinson E., Totten P., & Waheed A. (1993b). Low-Density Acid-Removable Cement as a Solution for Lost Circulation Across Producing Formations *SPE Middle East Oil Show*. <https://doi.org/10.2118/25543-ms>
- [6] Brian S., and Ashok S., (2013). Detailed Laboratory Investigation of Acid Soluble Cements as Solution for Lost Circulation across the Producing Zones. *All Days*. <https://doi.org/10.2118/166804>
- [7] Calvert, D., & Smith, D. K. (1990). API Oilwell Cementing Practices. *Journal of Petroleum Technology*, 42(11), 1364–1373. <https://doi.org/10.2118/20816-pa>
- [8] Costa, B. L. D. S., Souza, G. G. D., Freitas, J. C. D. O., Araujo, R. G. D. S., & Santos, P. H. S. (2017). Silica content influence on cement compressive strength in wells subjected to steam injection. *Journal of Petroleum Science and Engineering*, 158, 626–633. <https://doi.org/10.1016/j.petrol.2017.09.006>
- [9] Gaurina-Medimurec, N., Pašić, B., Mijić, P., & Medved, I. (2021b). Drilling Fluid and Cement Slurry Design for Naturally Fractured Reservoirs. *Applied Sciences*, 11(2), 767. <https://doi.org/10.3390/app11020767>
- [10] Hakyeul, T. L., Matthew H, and Janz R, Schlumberger (2015, July 20-22). Particle size distribution acid soluble cement. *Unconventional Resources Technology Conference San Antonio, Texas, USA*.
- [11] Herriot-Watt (2005). Drilling Engineering. [https://www.academia.edu/39642604/Heriot\\_Watt\\_University\\_Drilling\\_Engineering](https://www.academia.edu/39642604/Heriot_Watt_University_Drilling_Engineering)
- [12] Herriot-Watt (2022). Cementing-11. *Course hero*. <https://www.coursehero.com/file/p6qn3sq0/Cementing-11-Institute-of-Petroleum-Engineering-Heriot-Watt-University-Cement/>
- [13] Jadhav, R., & Patil, S. (2018). Acid-Soluble Thixotropic Cement System for Lost Circulation Challenges. *Day 2 Tue, November 13, 2018*. <https://doi.org/10.2118/193168-ms>
- [14] Khan, B., & Muhammad-Ullah, M. U. (2004). Effect of a Retarding Admixture on the Setting Time. of Cement Pastes in Hot Weather. *Journal of King Abdulaziz University-Engineering Sciences*, 15(1), 63–79. <https://doi.org/10.4197/eng.15-1.5>
- [15] Lorek, A., Labus, M., & Bujok, P. (2016b). Wellbore cement degradation in contact zone with formation rock. *Environmental Earth Sciences*, 75(6). <https://doi.org/10.1007/s12665-015-5114-z>
- [16] Matteo, E. N. M., Huet, & Scherer, G. W. S. (2016). Precipitation/Dissolution of Calcium Carbonate in Wellbore Cement and its Implications for the Seal Integrity of abandoned Wells. <https://www.researchgate.net/publication/266669572>.
- [17] Mangadlao, J. D., Cao, P., & Advincula, R. C. (2015). Smart cement and cement additives for oil and gas operations. *Journal of Petroleum Science and Engineering*, 129, 63–76. <https://doi.org/10.1016/j.petrol.2015.02.009>
- [18] Nasr-El-Din, H. A., Al-Yami, A., Al-Aamri, A., & El-Marsafawi, Y. (2007). A study of Acid Cement Reactions Using the Rotating Disk Apparatus. *All Days*. <http://doi.org/10.2118/106443.ms>
- [19] Nelson, E. B. (2006) Well Cementing. *Elsevier*, 25-235.
- [20] Ogbonna, F.J. (2010) *Design and field Application of drilling cementing and stimulation fluids*. Port Harcourt, Rivers State Nigeria. Amethyst & Colleagues Publishers.
- [21] Rageh, S. M., Nezami, M.K., Dhanalakshmi, K. & Basha, S.L.A. (2017). Compressive Strength and Thickening Time of Cement in Oil Well. *International Journal of Engineering Science Invention (IJESI)*, 6(12):1-4

- [22] Renpu, W., 2011. *Advanced Well Completion Engineering*. New York: Gulf Professional Publishing.
- [23] Repetto, C., Moroni, N., Pilia, L., D'Ancona, E., Ravi, K., & Santra, A. (2010). *Successful Application of Acid-Soluble Plugs in Open Hole Slotted-Liner Completion*. All Days. <https://doi.org/10.2>
- [24] Salam, K. K., Arinkoola, A. O., Ajagbe, B. M., & Sanni, O. (2013). Evaluation of Thickening Time of Oil Field Class G Cement Slurry at High Temperature and Pressure Using Experimental Design - TI Journals. *International Journal of Engineering Science*. <http://www.waprogramming.com/papers/51f6656fab0446.94110973.pdf>
- [25] Wang, Y., He, F., Wang, J., Wang, C., & Xiong, Z. (2019b). Effects of calcium bicarbonate on the properties of ordinary Portland cement paste. *Construction and Building Materials*, 225, 591–600. <https://doi.org/10.1016/j.conbuildmat.2019.07.262>

# Breaking Index Study on Weighted Laplace Equation

Syawaluddin Hutahaean

Ocean Engineering Program, Faculty of Civil and Environmental Engineering, -Bandung Institute of Technology (ITB), Bandung 40132, Indonesia

[syawalf1@yahoo.co.id](mailto:syawalf1@yahoo.co.id)

Received: 04 Dec 2023,

Receive in revised form: 08 Jan 2024,

Accepted: 17 Jan 2024,

Available online: 25 Jan 2024

©2024 The Author(s). Published by AI  
Publication. This is an open access article under  
the CC BY license

[\(https://creativecommons.org/licenses/by/4.0/\)](https://creativecommons.org/licenses/by/4.0/)

**Keywords—** *Weighted Taylor Series, Weighted Laplace Equation, Weighted Coefficients*

**Abstract—** *This study serves as an extension of prior research focusing on weighting coefficients within the context of weighted Taylor series. The primary objective is to determine the weighting coefficients' values in the weighted Taylor series for the purpose of modeling water waves based on velocity potential. Utilizing the weighted Taylor series, we derive both the weighted continuity equation and the weighted Laplace equation. The latter is addressed using the variable separation method over a sloping bottom, leading to the formulation of the velocity potential equation, wave constant equations, and energy conservation equations. Within the wave constant equations, a breaking equation is incorporated. Leveraging both the breaking equation and the energy conservation equations, breaking indexes equations are formulated. These equations encompass breaker length, breaker depth, and breaker height indexes, with weighting coefficients prominently featured. Calibrating the results of the breaking indexes equations against findings from earlier studies provides suitable values for the weighting coefficients. Additionally, this research introduces a shoaling-breaking model and a refraction-diffraction model to explore the phenomena of shoaling-breaking within the solution of the weighted Laplace equation.*

## I. INTRODUCTION

Hydrodynamic equations are conventionally expressed through Taylor series, typically truncated to first order, under the assumption that higher-order terms, such as second order and beyond, become negligible at very small intervals. While not inherently incorrect, this truncation approach sacrifices the representation of the function's characteristics encapsulated in the higher-order terms, leading to an imprecise approximation.

To address this limitation, Hutahaean (2021,2022,2023a) proposes the utilization of weighted Taylor series. This involves truncating the Taylor series to the first order, while compensating for the omission of higher-order contributions through the incorporation of weighting coefficients. In Hutahaean's work (2023a), a more systematic application of Taylor series truncation is introduced, employing the Central Difference Method. This method allows for the systematic removal of even higher-

order differential terms, ensuring their disappearance without merely being eliminated or overlooked. Furthermore, the study explores the extraction of 3rd order odd differential term contributions, with the additional inclusion of 5th order terms.

The use of the weighted Taylor series is characterized by the absence of truncation errors. Consequently, when applied to the continuity equation, the weighted Taylor series formulation minimizes or eliminates truncation errors. Similarly, the weighted Laplace equation, derived from the weighted continuity equation, maintains this heightened accuracy. Moreover, equations pertaining to various wave mechanics, formulated using the weighted Laplace equations, incorporate weighting coefficients, thereby enhancing their accuracy and reliability.

**II. WEIGHTED TAYLOR SERIES**

Taylor series (Arden, Bruce W. and Astill Kenneth N., 1970) for a function  $f = f(x, t)$  where  $x$  is the horizontal axis and  $t$  is time

$$f(x + \delta x, t + \delta t) = f(x, t) + \delta t \frac{\partial f}{\partial t} + \delta x \frac{\partial f}{\partial x} + \frac{\delta t^2}{2!} \frac{\partial^2 f}{\partial t^2} + \delta t \delta x \frac{\partial^2 f}{\partial t \partial x} + \frac{\delta x^2}{2!} \frac{\partial^2 f}{\partial x^2} + \dots \dots \dots (1)$$

This equation can be expressed as,

$$f(x + \delta x, t + \delta t) = f(x, t) + \left(1 + \frac{\delta t}{2!} \frac{\partial}{\partial t} + \delta x \frac{\partial}{\partial x} + \dots\right) \delta t \frac{\partial f}{\partial t} + \left(1 + \frac{\delta x}{2!} \frac{\partial}{\partial x} + \dots\right) \delta x \frac{\partial f}{\partial x}$$

In this paper,  $x$  represents the horizontal axis,  $z$  represents the vertical axis, while  $t$  represents time.

The complete Taylor series, there are contributions from high-order differential terms in the first-order differential term. The contributions of these high-order differential terms can be represented by a coefficient, allowing for the elimination of terms with high differentials.

$$f(x + \delta x, t + \delta t) = f(x, t) + \gamma_{t,2} \delta t \frac{\partial f}{\partial t} + \gamma_x \delta x \frac{\partial f}{\partial x} \dots \dots \dots (2)$$

$\gamma_{t,2}$  and  $\gamma_x$  are referred to as weighting coefficients, while (2) is called the weighted Taylor series. The weighted Taylor series for the function  $f(x, z, t)$  is as follows:

$$f(x + \delta x, z + \delta z, t + \delta t) = f(x, z, t) + \gamma_{t,3} \delta t \frac{\partial f}{\partial t} + \gamma_x \delta x \frac{\partial f}{\partial x} + \gamma_z \delta z \frac{\partial f}{\partial z} \dots \dots \dots (3)$$

There is no difference in the values of  $\gamma_x$  in the function  $f(x, t)$  compared to  $\gamma_x$  in the function  $f(x, z, t)$ . The baseline values for these weighting coefficients are  $\gamma_{t,2} = 2$ ,  $\gamma_{t,3} = 3$ ,  $\gamma_x = 1$  and  $\gamma_z = 1$ . More precise values of the weighting coefficients are presented in Table (1). The calculation method can be found in Hutahaeen (2023a), where the computation of the weighting coefficients in Table (1) is achieved with greater accuracy compared to Hutahaeen (2023a). In these weighting coefficients, all even-order differential terms in the Taylor series are represented, while the absorbed odd-order high differential

terms are of order 3 and 5. Higher-order differentials are truncated with the reduction of intervals,  $\delta t$ ,  $\delta x$  and  $\delta z$ . The values of the weighting coefficients are presented in Table (1).

Table 1 Weighting coefficient values

| $\epsilon$ | $\gamma_{t,2}$ | $\gamma_{t,3}$ | $\gamma_x$ | $\gamma_z$ |
|------------|----------------|----------------|------------|------------|
| 0.03       | 1.99812        | 3.05087        | 0.98899    | 1.11999    |
| 0.032      | 1.99786        | 3.05877        | 0.98746    | 1.139      |
| 0.034      | 1.99758        | 3.06738        | 0.98583    | 1.15986    |
| 0.036      | 1.99728        | 3.07674        | 0.9841     | 1.1827     |
| 0.038      | 1.99695        | 3.08689        | 0.98227    | 1.20765    |
| 0.04       | 1.99662        | 3.09786        | 0.98034    | 1.23485    |
| 0.042      | 1.99626        | 3.1097         | 0.97831    | 1.26448    |
| 0.044      | 1.99588        | 3.12244        | 0.97617    | 1.29669    |
| 0.046      | 1.99548        | 3.13614        | 0.97393    | 1.3317     |

$\epsilon$  is referred to as the optimization coefficient, where a larger  $\epsilon$  corresponds to a larger interval size and consequently, larger values for the absorbed third and fifth-order differential terms in the weighting coefficients. This research aims to obtain appropriate values for the weighting coefficients expressed in terms of  $\epsilon$ . The appropriateness is assessed concerning the breaking parameter generated by the breaking index equations.

**III. WEIGHTED LAPLACE EQUATION**

The Laplace equation is formulated by employing the continuity equation, substituting the properties of the velocity potential into the continuity equation. The formulation of the weighted continuity equation is carried out using a well-known method, namely by applying the principle of mass conservation to a control volume where fluid inflow-outflow occurs,

3.1. Weighted Continuity Equation

By employing the weighted Taylor series, a weighted continuity equation can be obtained.

$$\gamma_x \frac{\partial u}{\partial x} + \gamma_z \frac{\partial w}{\partial z} = 0 \dots \dots \dots (4)$$

$u$  is the horizontal water particle velocity, and  $w$  is the vertical water particle velocity. This equation represents the weighted continuity equation, where  $\gamma_x$  and  $\gamma_z$  are weighting coefficients. By using the weighted Taylor series, there is no longer truncation error or at least the truncation error has been greatly minimized

Mathematically, equation (4) can be written as,



$$\frac{\partial u}{\partial x} + \frac{\gamma_z}{\gamma_x} \frac{\partial w}{\partial z} = 0$$

Or,

$$\frac{\gamma_x}{\gamma_z} \frac{\partial u}{\partial x} + \frac{\partial w}{\partial z} = 0$$

Both of these writings are somewhat inaccurate and will result in different solutions because each coefficient has a specific function. It can be said that  $\gamma_x$  is associated with  $\frac{\partial u}{\partial x}$  and  $\gamma_z$  is associated with  $\frac{\partial w}{\partial z}$ .

### 3.2. Weighted Laplace Equation

In fluid flow, there is a scalar quantity called velocity potential, denoted as,

$$u = -\frac{\partial \phi}{\partial x} \text{ and } w = -\frac{\partial \phi}{\partial z}$$

Substituting the velocity potential property into (4), we obtain the weighted Laplace equation,

$$\gamma_x \frac{\partial^2 \phi}{\partial x^2} + \gamma_z \frac{\partial^2 \phi}{\partial z^2} = 0 \quad \dots\dots(5)$$

This Laplace equation differs from the commonly used Laplace equation in water wave modeling, where there are actually weighting coefficients with  $\gamma_x = \gamma_z = 1$ .

## IV. SOLUTION TO THE WEIGHTED LAPLACE EQUATION

### 4.1. Solution using the Separation of Variables Method

The solution to (5) is carried out using the separation of variables method. In the variable separation method, it is assumed that the velocity potential is the product of three functions (Dean (1991)), namely

$$\phi(x, z, t) = X(x)Z(z)T(t) \quad \dots(6)$$

Here,  $X(x)$  : is a function of  $x$  only,  $Z(z)$  is a function of  $z$  only, and  $T(t)$  is a function of  $t$  only. Substituting into (5) and dividing the equation by (6), the following is obtained:

$$\frac{\gamma_x}{X(x)} \frac{\partial^2 X}{\partial x^2} + \frac{\gamma_z}{Z(z)} \frac{\partial^2 Z}{\partial z^2} = 0$$

This equation is fulfilled if

$$\frac{\gamma_x}{X(x)} \frac{\partial^2 X}{\partial x^2} = -k_x^2$$

Defined as  $k_x = \frac{k}{\sqrt{\gamma_x}}$ , hence

$$\frac{1}{X(x)} \frac{\partial^2 X}{\partial x^2} = -k_x^2 \quad \dots(7)$$

Using the same method,

$$\frac{1}{Z(z)} \frac{\partial^2 Z}{\partial z^2} = k_z^2 \quad \dots\dots(8)$$

Where  $k_z = \frac{k}{\sqrt{\gamma_z}}$ .

$k$  is the wave number where the wavelength is  $L = \frac{2\pi}{k}$ . Hence, there are two wavelengths: the horizontal wavelength,  $L_x = \frac{2\pi}{k_x}$ , and the vertical wavelength,  $L_z = \frac{2\pi}{k_z}$ , with different lengths.

Equation (7), is offered for a solution

$$X(x) = A \cos k_x x + B \sin k_x x$$

Equation (8) has a solution of

$$Z(z) = C e^{k_z z} + D e^{-k_z z}$$

Then, an assumption is made that the velocity potential is periodic with respect to time; hence,  $T(t) = \sin \sigma t$

$\sigma = \frac{2\pi}{T}$  s the angular frequency, where  $T$  is the wave period. Substituting  $X(x)$ ,  $Z(z)$  and  $T(t)$  ke (6),

$$\phi(x, z, t) = (A \cos k_x x + B \sin k_x x) (C e^{k_z z} + D e^{-k_z z}) \sin \sigma t \quad \dots(9)$$

The constants A, B, C, and D in equation (9) still need their specific forms to be determined.

### 4.2. Working on the Kinematic Bottom Boundary Condition

To obtain equations for the constants in the solution, the Kinematic Bottom Boundary Condition is applied at characteristic points where  $\cos k_x x = \sin k_x x$ . At these characteristic points, the velocity potential equation becomes,

$$\phi(x, z, t) = (A + B) \cos k_x x (C e^{k_z z} + D e^{-k_z z}) \sin \sigma t$$

Kinematic bottom boundary condition is,

$$w_{-h} = -u_{-h} \frac{dh}{dx}$$

$w_{-h}$  is the vertical water particle velocity at the sea bed at  $z = -h$ .

$u_{-h}$  is the horizontal water particle velocity at the sea bed at  $z = -h$ .

$h$  is the water depth relative to the still water level,  $\frac{dh}{dx}$  is the bottom slope, which has a negative value for waves moving from deeper to shallower waters. Utilizing the properties of velocity potential,

$$w(x, z, t) = -\frac{\partial \phi}{\partial z} = -(A + B)k_z \cos k_x x (C e^{k_z z} - D e^{-k_z z}) \sin \sigma t$$

$$w_{-h} = -(A + B)k_z \cos k_x x$$

$$(Ce^{-k_z h} - De^{k_z h}) \sin \sigma t$$

$$u(x, z, t) = -\frac{\partial \phi}{\partial x} = (A + B)k_x \sin k_x x$$

$$(Ce^{k_z z} + De^{-k_z z}) \sin \sigma t$$

$$u_{-h} = (A + B)k_x \sin k_x x (Ce^{-k_z h} + De^{k_z h}) \sin \sigma t$$

The substitution of the Equations  $w_{-h}$  and  $u_{-h}$  to Kinematic Bottom Boundary Condition was performed at characteristic points as well as at  $(A + B)$  and when  $\sin(\sigma t)$  is not equal to zero, yields the equation

$$k_z(Ce^{-k_z h} - De^{k_z h}) = k_x(Ce^{-k_z h} + De^{k_z h}) \frac{dh}{dx}$$

$$\left(k_z - k_x \frac{dh}{dx}\right) Ce^{-k_z h} = \left(k_z + k_x \frac{dh}{dx}\right) De^{k_z h}$$

Considering  $k_x = \frac{k}{\sqrt{\gamma_x}}$  dan  $k_z = \frac{k}{\sqrt{\gamma_z}}$

$$\left(\frac{1}{\sqrt{\gamma_z}} - \frac{1}{\sqrt{\gamma_x}} \frac{dh}{dx}\right) Ce^{-k_z h} = \left(\frac{1}{\sqrt{\gamma_z}} + \frac{1}{\sqrt{\gamma_x}} \frac{dh}{dx}\right) De^{k_z h}$$

$$C = De^{2k_z h} \frac{\frac{1}{\sqrt{\gamma_z}} + \frac{1}{\sqrt{\gamma_x}} \frac{dh}{dx}}{\frac{1}{\sqrt{\gamma_z}} - \frac{1}{\sqrt{\gamma_x}} \frac{dh}{dx}}$$

Defined as,

$$\alpha = \frac{\frac{1}{\sqrt{\gamma_z}} + \frac{1}{\sqrt{\gamma_x}} \frac{dh}{dx}}{\frac{1}{\sqrt{\gamma_z}} - \frac{1}{\sqrt{\gamma_x}} \frac{dh}{dx}}$$

Hence

$$C = De^{2k_z h} \alpha$$

Substituting to (7)

$$\phi(x, z, t) = (A + B) \cos k_x x$$

$$(De^{2k_z h} \alpha e^{k_z z} + De^{-k_z z}) \sin \sigma t$$

$$\phi(x, z, t) = (A + B)De^{k_z h} \cos k_x x$$

$$(\alpha e^{k_z(z+h)} + e^{-k_z(z+h)}) \sin \sigma t$$

Defined as,

$$\beta(z) = \frac{\alpha e^{k_z(z+h)} + e^{-k_z(z+h)}}{2}$$

$$\beta_1(z) = \frac{\alpha e^{k_z(z+h)} - e^{-k_z(z+h)}}{2}$$

Where on  $\alpha = 1$ ,

$$\beta(z) = \cosh k_z(h + z); \beta_1(z) = \sinh k_z(h + z)$$

$$\phi(x, z, t) = 2(A + B)De^{k_z h} \beta(z) \cos k_x x \sin \sigma t$$

Defined as  $A = 2A$  dan  $B = 2B$ , hence

$$\phi(x, z, t) = (A + B)De^{k_z h} \beta(z) \cos k_x x \sin \sigma t$$

Hutahaean (2022) shows that  $A = B$

$$\phi(x, z, t) = 2ADe^{k_z h} \beta(z) \cos k_x x \sin \sigma t$$

Defined as  $G = ADe^{k_z h}$

$$\phi(x, z, t) = 2G\beta(z) \cos k_x x \sin \sigma t$$

The full equation,

$$\phi(x, z, t) = G\beta(z) \cos k_x x \sin \sigma t + G\beta(z)$$

$$\sin k_x x \sin \sigma t \quad \dots(10)$$

At the characteristic point where  $\cos k_x x = \sin k_x x$ , velocity potential equation becomes,

$$\phi(x, z, t) = 2G\beta(z) \cos k_x x \sin \sigma t \quad \dots(11)$$

## V. EQUATION FOR G

The equation for  $G$  is formulated by integrating the Kinematic Free Surface Boundary Condition with respect to time  $t$  and is performed at characteristic points. The form of the Kinematic Free Surface Boundary Condition uses a weighted Taylor Series for two variables  $f = f(x, t)$ , in this case, where the function  $f$  is the water elevation  $\eta = \eta(x, t)$ .

$$\eta(x + \delta x, t + \delta t) = \eta(x, t) + \gamma_{t,2} \delta t \frac{\partial \eta}{\partial t} + \gamma_x \delta x \frac{\partial \eta}{\partial x}$$

$$\frac{\eta(x + \delta x, t + \delta t) - \eta(x, t)}{\delta t} = \gamma_{t,2} \frac{\partial \eta}{\partial t} + \gamma_x \frac{\delta x}{\delta t} \frac{\partial \eta}{\partial x}$$

With  $\delta t$  and  $\delta x$  that are small, there obtained,

$$\frac{D\eta}{dt} = \gamma_{t,2} \frac{\partial \eta}{\partial t} + \gamma_x u_\eta \frac{\partial \eta}{\partial x}$$

$\frac{D\eta}{dt}$  is the total velocity of vertical surface water particle movement is denoted as  $w_\eta$ , while  $u_\eta$  represents the horizontal surface water particle velocity. Therefore, the equation for the Kinematic Free Surface Boundary Condition is.

$$w_\eta = \gamma_{t,2} \frac{\partial \eta}{\partial t} + \gamma_x u_\eta \frac{\partial \eta}{\partial x}$$

This equation is expressed as the water surface equation as follows,

$$\gamma_{t,2} \frac{\partial \eta}{\partial t} = w_\eta - \gamma_x u_\eta \frac{\partial \eta}{\partial x}$$

$w_\eta$  and  $u_\eta$  are substituted by velocity potential (11), using the velocity potentials properties ( $u = -\frac{\partial \phi}{\partial x}$ ,  $w = -\frac{\partial \phi}{\partial z}$ ), and by considering that  $k_x = \frac{k}{\sqrt{\gamma_x}}$  dan  $k_z = \frac{k}{\sqrt{\gamma_z}}$ ,

$$\gamma_{t,2} \frac{\partial \eta}{\partial t} = -2Gk \left( \frac{1}{\sqrt{\gamma_z}} \beta_1(\eta) + \sqrt{\gamma_x} \beta(\eta) \right) \frac{\partial \eta}{\partial x} \cos k_x x \sin(\sigma t) \dots\dots(12)$$

For the periodical function,

$$2Gk \left( \frac{1}{\sqrt{\gamma_z}} \beta_1(\eta) + \sqrt{\gamma_x} \beta(\eta) \right) \frac{\partial \eta}{\partial x} = constant$$

Integration (12) can be resolved by integrating  $\sin(\sigma t)$ .

$$\eta(x, t) = \frac{2Gk}{\gamma_{t,2}\sigma} \left( \frac{1}{\sqrt{\gamma_z}} \beta_1(\eta) + \sqrt{\gamma_x} \beta(\eta) \right) \frac{\partial \eta}{\partial x} \cos k_x x \cos(\sigma t)$$

For the periodical function,

$$A = \frac{2Gk}{\gamma_{t,2}\sigma} \left( \frac{1}{\sqrt{\gamma_z}} \beta_1(\eta) + \sqrt{\gamma_x} \beta(\eta) \right) \frac{\partial \eta}{\partial x} \dots\dots(13)$$

Where  $A$  is wave amplitude. Hence, water surface elevation equation is presented as,

$$\eta(x, t) = A \cos k_x x \cos(\sigma t) \dots\dots(14)$$

$$\frac{\partial \eta}{\partial x} = -k_x A \sin k_x x \cos \sigma t$$

At the characteristic point,  $\cos k_x x = \sin k_x x$  dan  $\cos(\sigma t) = \sin(\sigma t)$

$$\frac{\partial \eta}{\partial x} = -\frac{k_x A}{2}$$

Substituted to (13), obtaining a wave amplitude function equation as follows.

$$A = \frac{2Gk}{\gamma_{t,2}\sigma} \left( \frac{1}{\sqrt{\gamma_z}} \beta_1 \left( \frac{A}{2} \right) - \sqrt{\gamma_x} \beta \left( \frac{A}{2} \right) \frac{k_x A}{2} \right)$$

Considering  $k_x = \frac{k}{\sqrt{\gamma_x}}$  and taking out  $\beta \left( \frac{A}{2} \right)$  of the bracket,

$$A = \frac{2Gk\beta \left( \frac{A}{2} \right)}{\gamma_{t,2}\sigma} \left( \frac{1}{\sqrt{\gamma_z}} \beta_1 \left( \frac{A}{2} \right) - \frac{kA}{2} \right)$$

Based on the conservation law of wave number discussed in section (6), hence  $\beta \left( \frac{A}{2} \right)$  and  $\beta_1 \left( \frac{A}{2} \right)$  are constant, where

$$\frac{\beta_1 \left( \frac{A}{2} \right)}{\beta \left( \frac{A}{2} \right)} = constant$$

This constant value applies to all bodies of water, including both deep water and shallow water. In deep water where the bottom slope no longer has an effect, hence

$$\frac{\beta_1 \left( \frac{A}{2} \right)}{\beta \left( \frac{A}{2} \right)} = \tan k \left( h + \frac{A}{2} \right) \approx 1$$

This condition is achieved when,

$$k \left( h + \frac{A}{2} \right) = \theta \pi$$

Where  $\tanh \theta \pi \approx 1$ ,  $\theta$  is referred to as the deep water coefficient. The equation for the wave amplitude function becomes:

$$A = \frac{2Gk \cosh \theta \pi}{\gamma_{t,2}\sigma} \left( \frac{\tanh \theta \pi}{\sqrt{\gamma_z}} - \frac{kA}{2} \right) \dots\dots(15)$$

This equation can be expressed as Equation for  $G$ ,

$$G = \frac{\sigma \gamma_{t,2} A}{2k \left( \frac{\tanh \theta \pi}{\sqrt{\gamma_z}} - \frac{kA}{2} \right) \cosh \theta \pi} \dots\dots(16)$$

## VI. EQUATIONS OF CONSERVATION

In its movement towards shallower waters, waves will undergo changes in its constants, namely  $G$ ,  $k$  and  $A$ . The governing equations controlling these changes are the conservation equation of wave number and the conservation equation of energy.

### a. Conservation Equation of Wave Number

In the method of separating variables, it is stated that  $Z(z)$  is a function of  $z$  only. For the velocity potential equation,  $Z(z)$  is expressed as:

$$Z(z) = \beta(z)$$

As only function  $z$ , hence,

$$\frac{\partial Z(z)}{\partial x} = \beta_1(z) \frac{\partial k_z(h+z)}{\partial x} = 0$$

Hence

$$\frac{\partial k_z(h+z)}{\partial x} = 0$$

Substituting  $k_z = \frac{k}{\sqrt{\gamma_z}}$  and according to the formulation of  $G$  equation, therefore  $z = \frac{A}{2}$  is used.

$$\frac{\partial k \left( h + \frac{A}{2} \right)}{\partial x} = 0 \dots\dots(17)$$

This equation is the conservation equation of wave number. This equation shows that,,

$$k \left( h + \frac{A}{2} \right) = constant$$

The constant value is found in deep water, i.e.,

$$\tanh k \left( h + \frac{A}{2} \right) \approx 1$$

Where  $\tanh \theta \pi \approx 1$  and  $\theta$  is the deep water coefficient, therefore,

$$k \left( h + \frac{A}{2} \right) = \theta \pi \dots\dots(18)$$

This equation is valid for all water depths, including deep water and shallow water.

### b. Conservation Equation of Energy

Substituting (10) into (5) using the properties of velocity potential, and working on the obtained equation with point characteristic properties, we get

$$\frac{\partial^2 G}{\partial x^2} = 0 \quad \dots(19)$$

Substituting (11) into (5) using the properties of velocity potential and considering (19) at characteristic points, we obtain

$$G \frac{\partial k}{\partial x} + 2k \frac{\partial G}{\partial x} = 0 \quad \dots(20)$$

This is an energy conservation equation.

### VII. DEEP WATER WAVE LENGTH

Hutahaean (2022) formulates the relationship between wavelength and wave height in deep water. By employing weighting coefficients in this study, the relationship between wavelength and wave height in deep water is,

$$L_0 = \frac{\pi(\gamma_{t,2} + \frac{\gamma_z \gamma_{t,3}}{2})H_0}{\gamma_{t,3} \tanh \theta \pi} \quad \dots(21)$$

$$L_{0,x} = L \sqrt{\gamma_x}$$

$$L_{0,z} = L \sqrt{\gamma_z}$$

Example calculation results of the wavelength for a wave amplitude  $A = 1.2$  m, with various values of weighting coefficients, are presented in Table (2).

Table.2 Wave length at wave amplitude of 1.2 m.

| $\epsilon$ | $L_x$<br>(m) | $L_z$<br>(m) | $\frac{H}{L_x}$ |
|------------|--------------|--------------|-----------------|
| 0.03       | 9.11         | 9.695        | 0.263           |
| 0.032      | 9.161        | 9.839        | 0.262           |
| 0.034      | 9.217        | 9.997        | 0.26            |
| 0.036      | 9.279        | 10.172       | 0.259           |
| 0.038      | 9.347        | 10.363       | 0.257           |
| 0.04       | 9.421        | 10.573       | 0.255           |
| 0.042      | 9.503        | 10.803       | 0.253           |
| 0.044      | 9.592        | 11.055       | 0.25            |
| 0.046      | 9.689        | 11.33        | 0.248           |

In Table (2), the  $\epsilon$  values represent the weighting coefficients, with the corresponding values available in Table (1).

Table (2) includes two wavelengths: the horizontal wavelength  $L_x$  and the vertical wavelength  $L_z$ . These

wavelengths exhibit a slight difference, although both are present. It is noteworthy that a larger  $\epsilon$  corresponds to a longer wavelength, resulting in a smaller wave steepness.

Toffoli, A., Babanin, A., Onaroto, M., and Wased, T. (2010), determined that the critical wave steepness is 0.170, with a recommended upper limit of 0.200. To align with Toffoli et al.'s criteria and achieve a wave steepness closer to their recommendations, it is advisable to utilize a larger  $\epsilon$  value.

### VIII. WAVE TRANSFORMATION MODEL

This section demonstrates that the potential velocity encompasses the shoaling-breaking phenomenon. Notably, this phenomenon persists irrespective of whether the original Laplace equation (as proposed by Hutahaean (2023b)) or the weighting coefficients  $\gamma_x = \gamma_z = 1$  are employed. The focus of this section is solely on illustrating that the shoaling-breaking phenomenon remains unaffected by the weighting coefficients in the Laplace equation.

Within this context, the weighting coefficient plays a crucial role in influencing the breaking characteristics. Specifically, it impacts key parameters such as breaker height  $H_b$ , breaker depth  $h_b$  and breaker length  $L_b$ .

#### 8.1. Shoaling Breaking Modeling

The shoaling and breaking models are established based on conservation equations (17) and (20), incorporating equations governing the wave amplitude function (15) and the function  $G$  (16). The detailed formulation process is elucidated in Hutahaean (2023b). The equations governing the changes in wave constants  $k$ ,  $A$ , and  $G$  as a wave travels from point  $x$  to  $x + \delta x$  are essential components of this approach.

$$\frac{dk}{dx} = -\frac{4k}{(4h+3A)} \frac{dh}{dx} \quad \dots\dots(22)$$

$$\frac{\partial A}{\partial x} = \frac{G}{\sigma \gamma_{t,2}} \frac{\partial k}{\partial x} \left( \frac{\tan \theta \pi}{\sqrt{\gamma_z}} - \frac{kA}{2} \right) \cosh(\theta \pi) \quad \dots\dots(23)$$

Furthermore,

$$k_{x+\delta x} = k_x + \delta x \frac{\partial k}{\partial x}$$

$$A_{x+\delta x} = A_x + \delta x \frac{\partial A}{\partial x}$$

$$G_{x+\delta x} = e^{\ln G_x - \frac{1}{2}(\ln k_{x+\delta x} - \ln k_x)}$$

To demonstrate the outcomes of the shoaling-breaking model, an analysis was conducted in a coastal zone characterized by a bottom slope of  $\frac{dh}{dx} = -0.02$ . The study utilized waves with a period of 8.0 seconds and a deep water wave amplitude of  $A_0 = 1.2$  meters. The deep water

coefficient  $\theta = 1.60$ , and a weighting coefficient of  $\varepsilon = 0.042$  was applied, with the specific values found in Table (1). The deep water wave number,  $k_0$ , was calculated using equation (21), and the deep water wave height,  $h_0 = \frac{\theta\pi}{k_0} - \frac{A_0}{2}$ . Additionally, the deep water wave constant  $G_0$  was calculated using equation (16). The results of the shoaling-breaking model are visually presented in Figure (1), offering a comprehensive illustration of the dynamic behavior in the coastal zone under the specified conditions.

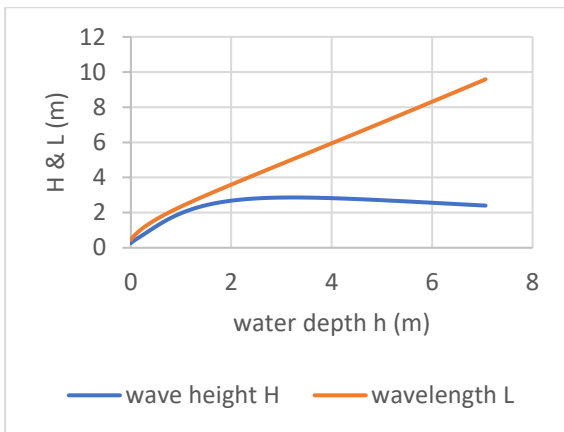


Fig.1: The outcome of shoaling-breaking modeling

In Fig(1), it can be observed that the model is able to simulate shoaling and breaking phenomena effectively. Details regarding breaking characteristics, including breaker height  $H_b$ , breaker depth  $h_b$ , and breaker length  $L_b$ , are discussed in another section.

### 8.2 Refraction-Diffraction Analysis

Utilizing the shoaling-breaking equations, the formulation of refraction-diffraction equations is established, as detailed in Hutahaeen (2023b). The application of the refraction-diffraction model is demonstrated on bathymetry featuring a headland configuration (Fig. (2)), considering waves with a period of 8 seconds and a deep water wave amplitude of 1.20 meters. The resulting 2-D contour image depicting wave height from the refraction-diffraction model is presented in Fig. (3), while Fig. (4) illustrates the 3-D wave height contour.

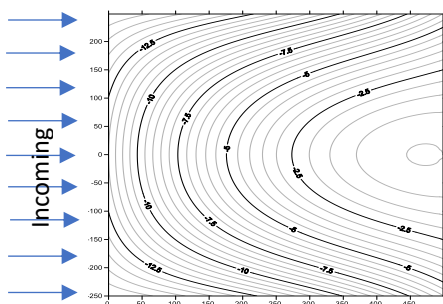


Fig.2: Batimetri tanjong contour

The model implementation involves a deep water coefficient of  $\theta = 1.60$  and an optimization coefficient of  $\varepsilon = 0.042$ , providing insights into wave behavior in the presence of bathymetric features and headlands.

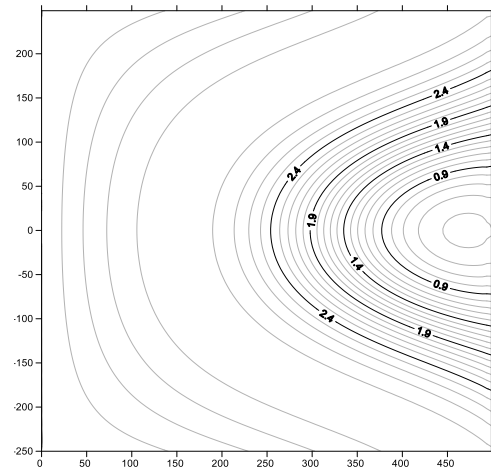


Fig.3: Wave height 2-D Contour

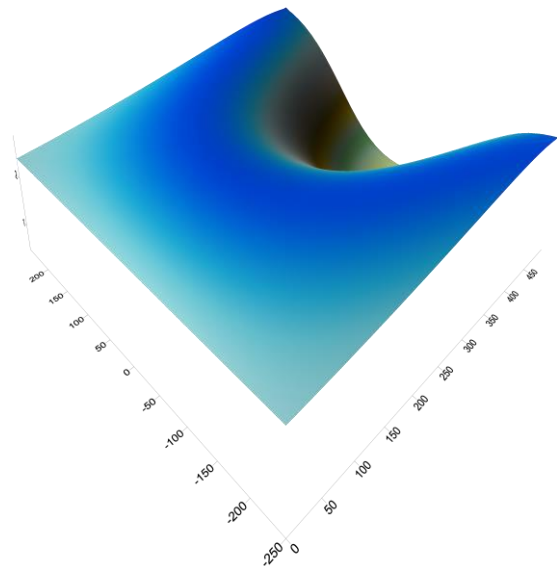


Fig.4: wave height 3-D Contour

In the analysis of refraction-diffraction results, a notable concentration of wave energy is observed at the center of the headland, coinciding with the point where breaking occurs. Both the shoaling-breaking model and the refraction-diffraction model incorporate equations involving the wave amplitude function, wave number conservation, and energy conservation to collectively simulate the processes of shoaling and breaking. These equations include weighting coefficients.

To determine suitable values for these weighting coefficients, an examination will be conducted using breaker index equations, as elaborated upon in the subsequent section..

**IX. BREAKING INDEXES EQUATIONS.**

In the preceding section, it has been demonstrated that the developed equations can effectively simulate shoaling and breaking. In this section, breaking indexes equations are formulated, and the role of corresponding weighting coefficients is studied.

9.1. Equation breaking.

The breaking equation is present in both the wave amplitude function Equation (15) and the wave constant Equation G (16). Breaking occurs when,

$$\frac{\tanh \theta \pi}{\sqrt{\gamma_z}} - \frac{kA}{2} = 0 \quad \dots\dots(24)$$

Based on Equation (24), breaker indexes are formulated, including the breaker length index, breaker depth index, and breaker height index.

9.2. Breaker Length Index Equation

Equation (24) can be expressed as,

$$\frac{kA}{2} = \frac{\tanh \theta \pi}{\sqrt{\gamma_z}}$$

Considering  $k_x = \frac{k}{\sqrt{\gamma_x}}$  or  $k = k_x \sqrt{\gamma_x}$  and  $k_x = \frac{2\pi}{L_x}$  hence

$$\frac{H_b}{L_{b,x}} = \frac{2 \tanh \theta \pi \sqrt{\gamma_x}}{\pi \sqrt{\gamma_z}} \quad \dots\dots(25)$$

$H_b$  represents the breaking wave height, while  $L_{x,b}$  is the horizontal wavelength at the breaker point. In Equation (25), there are weighting coefficients, namely  $\gamma_x$  and  $\gamma_z$ , indicating the influence of weighting coefficients on breaking characteristics in this equation. In Table (3), the calculation of  $\frac{H_b}{L_{b,x}}$  is presented for various values of  $\varepsilon$  and  $\theta$ , where  $\theta_1 = 1.60$ ,  $\theta_2 = 1.70$ ,  $\theta_3 = 1.80$  and  $\theta_4 = 1.90$ . The values of  $\tanh \theta \pi$  include,

$$\tanh 1.6\pi = 0.999914$$

$$\tanh 1.7\pi = 0.999954$$

$$\tanh 1.8\pi = 0.999975$$

$$\tanh 1.9\pi = 0.999987$$

All of them  $\approx 1$ .

Table.3 The value of  $\frac{H_b}{L_{b,x}}$  on different  $\varepsilon$  and  $\theta$

| $\varepsilon$ | $\theta_1$ | $\theta_2$ | $\theta_3$ | $\theta_4$ |
|---------------|------------|------------|------------|------------|
| 0.03          | 0.565      | 0.565      | 0.565      | 0.565      |
| 0.032         | 0.555      | 0.555      | 0.555      | 0.555      |
| 0.034         | 0.545      | 0.545      | 0.545      | 0.545      |
| 0.036         | 0.535      | 0.535      | 0.535      | 0.535      |
| 0.038         | 0.524      | 0.524      | 0.524      | 0.524      |

|       |       |       |       |       |
|-------|-------|-------|-------|-------|
| 0.04  | 0.513 | 0.513 | 0.513 | 0.513 |
| 0.042 | 0.502 | 0.502 | 0.502 | 0.502 |
| 0.044 | 0.49  | 0.49  | 0.49  | 0.49  |
| 0.046 | 0.479 | 0.479 | 0.479 | 0.479 |

In Table (3), it can be observed that as the value of  $\varepsilon$  increases, the value of  $\frac{H_b}{L_{b,x}}$  decreases. Meanwhile, concerning the deep water coefficient  $\theta$ , the value of  $\frac{H_b}{L_{b,x}}$  remains constant, as this is only considered up to the third decimal place. If examined up to the fifth decimal place, the  $\frac{H_b}{L_{b,x}}$  value increases with an increase in the  $\theta$  value.

9.3. Breaker Depth Index Equation.

Defined as

$$\tanh k \left( h + \frac{A}{2} \right) = \alpha k \left( h + \frac{A}{2} \right)$$

Substituting to (24),

$$\frac{\alpha k \left( h + \frac{A}{2} \right)}{\sqrt{\gamma_z}} - \frac{kA}{2} = 0$$

$$\alpha k \left( h + \frac{A}{2} \right) - \frac{\sqrt{\gamma_z} k A}{2} = 0$$

$$\alpha k h + \frac{\alpha k A}{2} - \frac{\sqrt{\gamma_z} k A}{2} = 0$$

$$\alpha - \left( \sqrt{\gamma_z} - \alpha \right) \frac{A}{2h} = 0$$

$$k \left( h + \frac{A}{2} \right) = \theta \pi \text{ hence ,}$$

Substituting to Equation  $\alpha$ ,

$$\alpha = \frac{\tanh \theta \pi}{\theta \pi}$$

At breaker point and on the sinusoidal wave,  $A = \frac{H}{2}$  applies

$$\frac{\tanh \theta \pi}{\theta \pi} - \left( \sqrt{\gamma_z} - \frac{\tanh \theta \pi}{\theta \pi} \right) \frac{A}{2h} = 0$$

$$\tanh \theta \pi - \left( \theta \pi \sqrt{\gamma_z} - \tanh \theta \pi \right) \frac{H_b}{4h_b} = 0$$

$$\frac{H_b}{h_b} = \frac{4 \tanh \theta \pi}{\left( \theta \pi \sqrt{\gamma_z} - \tanh \theta \pi \right)} \quad \dots\dots\dots(26)$$

This equation represents the breaker depth index, where  $h_b$  is the breaker depth. In equation (26), there is a weighting coefficient denoted as  $\gamma_z$ . Table (4) presents the results of the calculation of equation (26) for various values of  $\theta$  and several values of  $\varepsilon$ . In the table,  $\theta_1 = 1.60$ ,  $\theta_2 = 1.70$ ,  $\theta_3 = 1.80$  and  $\theta_4 = 1.90$ .

Table.4 the value of  $\frac{H_b}{h_b}$  on several values of  $\epsilon$  and  $\theta$

| $\epsilon$ | $\theta_1$ | $\theta_2$ | $\theta_3$ | $\theta_4$ |
|------------|------------|------------|------------|------------|
| 0.03       | 0.869      | 0.808      | 0.754      | 0.708      |
| 0.032      | 0.853      | 0.793      | 0.741      | 0.695      |
| 0.034      | 0.836      | 0.777      | 0.726      | 0.682      |
| 0.036      | 0.819      | 0.762      | 0.712      | 0.668      |
| 0.038      | 0.801      | 0.745      | 0.697      | 0.654      |
| 0.04       | 0.783      | 0.728      | 0.681      | 0.639      |
| 0.042      | 0.764      | 0.711      | 0.665      | 0.625      |
| 0.044      | 0.745      | 0.694      | 0.649      | 0.61       |
| 0.046      | 0.726      | 0.676      | 0.633      | 0.594      |

The results in Table (4) indicate that the value of  $\frac{H_b}{h_b}$  decreases with an increase in  $\epsilon$  and also decreases with an increase in  $\theta$ . For a constant value of  $H_b$ , the decrease in  $\frac{H_b}{h_b}$  with an increase in  $\theta$  suggests a deeper breaker depth. According to Mc. Cowan's criteria (1894), where  $\frac{H_b}{h_b} = 0.78$ , and considering the calculation of the breaker height  $h_b$  in subsection (9.5), resulting in  $\epsilon = 0.038 - 0.046$ , the appropriate  $\theta$  value is therefore 1.60.

9.4 Breaker depth-length index.

Equation (25) is written as an equation for  $H_b$  and substituted into (26), resulting in the breaker depth-length index equation, denoted as Equation (27).

$$\frac{h_b}{L_{b,x}} = \left(\frac{\theta}{2} - \frac{\tanh \theta \pi}{2\pi\sqrt{\gamma_z}}\right) \sqrt{\gamma_x} \dots(27)$$

Condition  $\frac{h}{L} \geq 1$  represents deep water conditions. Breaking due to bathymetry occurs in shallow water where  $\frac{h}{L} < 1$  hence, (27) must be less than 1. Table (5) illustrates the values of  $\frac{h_b}{L_{b,x}}$  for  $\epsilon = 1.60$  and  $\theta = 2.30$

Table.5 Provides an overview of the values of  $\frac{h_b}{L_b}$  concerning the deep water coefficient  $\theta$ .

| $\epsilon$ | $\theta = 1.60$       |                   | $\theta = 2.30$       |                   |
|------------|-----------------------|-------------------|-----------------------|-------------------|
|            | $\frac{h_b}{L_{b,x}}$ | $\frac{H_b}{h_b}$ | $\frac{h_b}{L_{b,x}}$ | $\frac{H_b}{h_b}$ |
| 0.03       | 0.65                  | 0.869             | 0.996                 | 0.567             |
| 0.032      | 0.651                 | 0.853             | 0.997                 | 0.557             |
| 0.034      | 0.652                 | 0.836             | 0.997                 | 0.547             |
| 0.036      | 0.653                 | 0.819             | 0.998                 | 0.536             |
| 0.038      | 0.655                 | 0.801             | 0.998                 | 0.525             |

|       |       |       |       |       |
|-------|-------|-------|-------|-------|
| 0.04  | 0.656 | 0.783 | 0.999 | 0.514 |
| 0.042 | 0.657 | 0.764 | 0.999 | 0.502 |
| 0.044 | 0.658 | 0.745 | 1     | 0.491 |
| 0.046 | 0.659 | 0.726 | 1     | 0.479 |

From Table (5), it is evident that as the value of  $\epsilon$  increases, the value of  $\frac{h_b}{L_{b,x}}$ , also increases, and as  $\theta$  increases, the value of  $\frac{h_b}{L_{b,x}}$  also increases. At  $\theta = 2.30$ , the value of  $\frac{h_b}{L_{b,x}}$  approaches 1. It can be concluded that the value of  $\theta$  must be less than 2.30.

9.5. Breaker Height Index Equation,  $\frac{H_b}{H_0}$ .

The breaker height index is the ratio of the breaker height to the wave height in deep water, denoted as  $\frac{H_b}{H_0}$ . The wave energy for a single wavelength is given by the equation:

$$E = c_E \rho g H^2 L$$

where  $c_E$  is the energy coefficient. In the linear wave theory (Dean (1991)),  $c_E = \frac{1}{8}$ . In this context, the value of  $c_E$  is not influential as it cancels out in the energy conservation equation. By equating the wave energy at the breaker point to the wave energy in deep water, we obtain Equation (28):

$$H_b^2 L_b = H_0^2 L_0 \dots\dots(28)$$

Equation (25) can be expressed as an equation for  $L_b$  and substituted into (28). Meanwhile,  $L_0$  is substituted with (21), resulting in Equation (29):

$$\frac{H_b}{H_0} = \left(\frac{2\sqrt{\gamma_x}(\gamma_{t,2} + \frac{\gamma_z \gamma_{t,3}}{2})}{\gamma_{t,3} \sqrt{\gamma_z}}\right)^{1/3} \dots(29)$$

In this equation, there are no parameters for the deep water coefficient  $\theta$  and wave period. Therefore, the breaker height is solely determined by the deep water wave height  $H_0$  and the weighting coefficient.

To illustrate the influence of the weighting coefficient on the breaker height index  $\frac{H_b}{H_0}$  and the breaker height  $H_b$ , the results are presented in Table (6). The calculated breaker height is compared with the breaker height from Komar, Paul D., and Gaughan, Michael K. (1968):

$$H_b = 0.39 g^{1/5} (TH_0)^{2/5} \text{ m.}$$

In this equation, the wave period  $T$ , is set to 8 seconds, and two different deep water wave heights  $H_0$  of 2.00 m and 2.40 m are used. In Table (6),  $H_{b-29}$  is the result of Equation (29) multiplied by  $H_0$ .

In Table (6), an observable trend is noted: as  $\epsilon$  increases, the breaker height decreases. Following the Komar-Gaughan equation, a breaker height  $H_0 = 2.00 \text{ m}$  is achieved at  $\epsilon =$

0.038, while for a higher initial wave height  $H_0 = 2.40$  m, the corresponding  $\varepsilon = 0.046$ . However, it is challenging to precisely determine  $\varepsilon$  from these findings. For a wave height of 2.40 m and a wave period of 8 seconds, identified as the maximum in that period, a pragmatic approach suggests using  $\varepsilon = 0.042$  for wave heights below the maximum.

Table.6 Presents the calculated breaker height  $H_b$ .

| $\varepsilon$ | $\frac{H_b}{H_0}$ | $H_0 = 2.0$ m |           | $H_0 = 2.4$ m |           |
|---------------|-------------------|---------------|-----------|---------------|-----------|
|               |                   | $H_{b-29}$    | $H_{b-K}$ | $H_{b-29}$    | $H_{b-K}$ |
| 0.03          | 1.267             | 2.534         | 2.463     | 3.041         | 2.85      |
| 0.032         | 1.259             | 2.518         | 2.463     | 3.021         | 2.85      |
| 0.034         | 1.25              | 2.501         | 2.463     | 3.001         | 2.85      |
| 0.036         | 1.241             | 2.483         | 2.463     | 2.979         | 2.85      |
| 0.038         | 1.232             | 2.464         | 2.463     | 2.957         | 2.85      |
| 0.04          | 1.222             | 2.444         | 2.463     | 2.933         | 2.85      |
| 0.042         | 1.212             | 2.424         | 2.463     | 2.909         | 2.85      |
| 0.044         | 1.202             | 2.403         | 2.463     | 2.884         | 2.85      |
| 0.046         | 1.191             | 2.382         | 2.463     | 2.858         | 2.85      |

The study of breaker indexes underscores the substantial impact of weighting coefficients on breaking parameters. Consequently, employing the weighted Laplace equation in modeling wave dynamics is anticipated to yield more accurate and reliable results for breaking parameters.

The results of this study also indicate that the appropriate deep water coefficient is  $\theta = 1.60$ , with a value of  $\varepsilon = 0.042$ , along with weighting coefficients:

| $\varepsilon$ | $\gamma_{t,2}$ | $\gamma_{t,3}$ | $\gamma_x$ | $\gamma_z$ |
|---------------|----------------|----------------|------------|------------|
| 0.042         | 1.99626        | 3.1097         | 0.97831    | 1.26448    |

### X. CONCLUSION

The Weighted Taylor series refers to a truncated Taylor series that is transformed into a first-order series with significantly reduced truncation errors, and in some cases, without any errors. Utilizing the weighted Taylor series for formulating the continuity equation and Laplace equation results in the creation of the weighted continuity equation and weighted Laplace equation, characterized by minimal truncation errors. Consequently, constructing a water wave model using the weighted Laplace equation enhances the model's accuracy.

The pivotal role of weighting coefficients cannot be overstated, as they play a crucial role in determining wave characteristics such as wavelength and breaking parameters, including breaker height, depth, and length. This

underscores the importance of utilizing the weighted Laplace equation in water wave modeling. Furthermore, since water wave modeling is inherently based on velocity potential, employing the weighted Laplace equation is deemed more effective.

In situations where the latest data from physical model research is available and reliable, the values of weighting coefficients can be easily adjusted to fine-tune the model. This adaptability enhances the applicability and accuracy of the water wave model, making it a valuable tool in studying water wave behavior.

### REFERENCES

- [1] Hutahaeen, S. (2021). Weighted Taylor Series for Water Wave Modeling. International Journal of Advance Engineering Research and Science (IJAERS). Vol. 8, Issue 6; Jun, 2021, pp 295-302. Article DOI: <https://dx.doi.org/10.22161/ijaers.86.37>.
- [2] Hutahaeen, S. (2022). Wavelength and wave Period Relationship with Wave Amplitude: A Velocity Potential Formulation. International Journal of Advance Engineering Research and Science (IJAERS). Vol. 9, Issue 8; Aug, 2022, pp 1-7. Article DOI: <https://dx.doi.org/10.22161/ijaers.98.38>.
- [3] Hutahaeen, S. (2023a). Method for Determining Weighting Coefficients in Weighted Taylor Series Applied to Water Wave Modeling. International Journal of Advance Engineering Research and Science (IJAERS). Vol. 10, Issue 12; Dec, 2023, pp 105-114. Article DOI: <https://dx.doi.org/10.22161/ijaers.1012.11>.
- [4] Arden, Bruce W. and Astill Kenneth N. (1970). Numerical Algorithms : Origins and Applications. Philippines copyright (1970) by Addison-Wesley Publishing Company, Inc.
- [5] Dean, R.G., Dalrymple, R.A. (1991). Water wave mechanics for engineers and scientists. Advance Series on Ocean Engineering.2. Singapore: World Scientific. ISBN 978-981-02-0420-4. OCLC 22907242.
- [6] Toffoli, A., Babanin, A., Onaroto, M. and Wased, T. (2010). Maximum steepness of oceanic waves : Field and laboratory experiments. Geophysical Research Letters. First published 09 March 2010. <https://doi.org/10.1029/2009GL.0441771>
- [7] Hutahaeen, S. (2023b). Water Wave Velocity Potential on Sloping Bottom in Water Wave Transformation Modeling . International Journal of Advance Engineering Research and Science (IJAERS). Vol. 10, Issue 10; Oct, 2023, pp 149-157. Article DOI: <https://dx.doi.org/10.22161/ijaers.1010.15>.
- [8] Mc Cowan, J. (1894). On the highest waves of a permanent type, Philosophical Magazine, Edinburgh 38, 5<sup>th</sup> Series, pp. 351-358.
- [9] Komar, P.D. & Gaughan M.K. (1972). Airy Wave Theory and Breaker Height Prediction, Coastal Engineering Proceedings, 1 (13).



# A Comprehensive Review on Intelligence Control for Complex System

Md Jubair<sup>1</sup>, Hossain MD Sabbir<sup>2</sup>, Ngulube Lazarous<sup>2</sup>, Hantosh Ali Hasan Abdulkarem<sup>2</sup>, Shimul Paul<sup>2</sup>, Muhammad Sabeeh khan<sup>2</sup>, Mohammed Arfan<sup>2</sup>, Abdullah al Rakib<sup>3</sup>

<sup>1</sup> Department of Computer Science, Hunan University, China

<sup>2</sup> Department of Mechatronic Engineering Jiangsu normal University, China

<sup>3</sup> Department Microelectronics Science and Engineering, Yangzhou University, China

Received: 08 Dec 2023,

Receive in revised form: 12 Jan 2024,

Accepted: 21 Jan 2024,

Available online: 29 Jan 2024

©2024 The Author(s). Published by AI Publication. This is an open access article under the CC BY license

(<https://creativecommons.org/licenses/by/4.0/>)

**Keywords**— *intelligence control, complex system, AI, fuzzy Control PID*

**Abstract**— *Control system intellectualization issues are observed. The need for intellectualization of a diverse variety of systems and control approaches is supported. The hierarchy of intellectual control levels is examined, and various artificial intelligence methods are compared. Intelligence control for complex systems involves using advanced algorithms and techniques, such as artificial intelligence and machine learning, to effectively manage and manipulate complex systems. This includes creating models and simulations to understand the system's behavior, sensing and acquiring real-time data, preprocessing and analyzing the data, making decisions based on the analyzed data and system models, adapting control strategies in real-time, facilitating human-machine interaction, monitoring performance, and optimizing control strategies. The goal is to improve efficiency, safety, reliability, and overall performance of complex systems in various domains.*

## I. INTRODUCTION

Artificial intelligence (AI) evolved and developed along with the idea of automatic control, beginning around the 1950s, with the first major applications in computing and information science, and later in automated control [1]. The first commercial and industrial applications of AI can be traced back to the 1980s [2]. AI has attained a certain level of stability and maturity throughout this time. The significant development in computer technology's capabilities, including hardware implementation of logical and other AI means, is a key aspect that can lead to a reassessment of today's successes and new ups of AI theory and practice. The phrase "intellectual control system" refers to any combination of hardware and software that is linked by a general information process and capable of synthesizing the control objective and finding rational solutions to attain the control goal (in the presence of motivation and knowledge includes environmental and internal status information) [1,3]. Human-machine

interaction now enables the capacity to synthesize the control goal, and autonomous control systems capable only of finding reasonable solutions to fulfill the control goal are referred to as "intelligent control systems." Currently, the science and practice of control are very interested in the integration of traditional automatic control methods with AI approaches, as well as AI applications in the field of control for complicated weakly structured objects and processes. Especially when the information, system state, control criteria, and control goals vary over time and become hazy and occasionally contradictory. The report considers a hierarchy of levels of intellectual control as well as a comparative analysis of various AI methods. Because there has been a significant increase in the number of theoretical and applied research in the field of fuzzy controllers over the last decade, the main objective of the study is to examine the important achievements in this area. Unfortunately, even this field does not allow for a thorough review free of the writers' preferences.

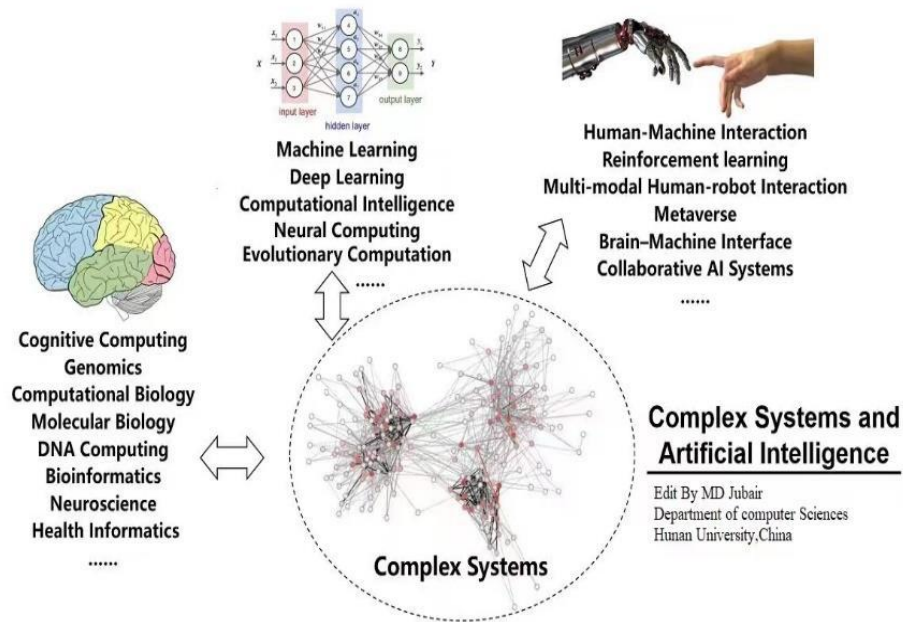


Fig 1: Complex System

Intelligence control for complex systems refers to the ability to effectively manage and manipulate a complex system using intelligent algorithms and techniques. This involves utilizing artificial intelligence, machine learning, and other computational methods to optimize the functioning of complex systems.

## II. Intelligence Control For Complex Systems

There are several key components of intelligence control for complex systems:

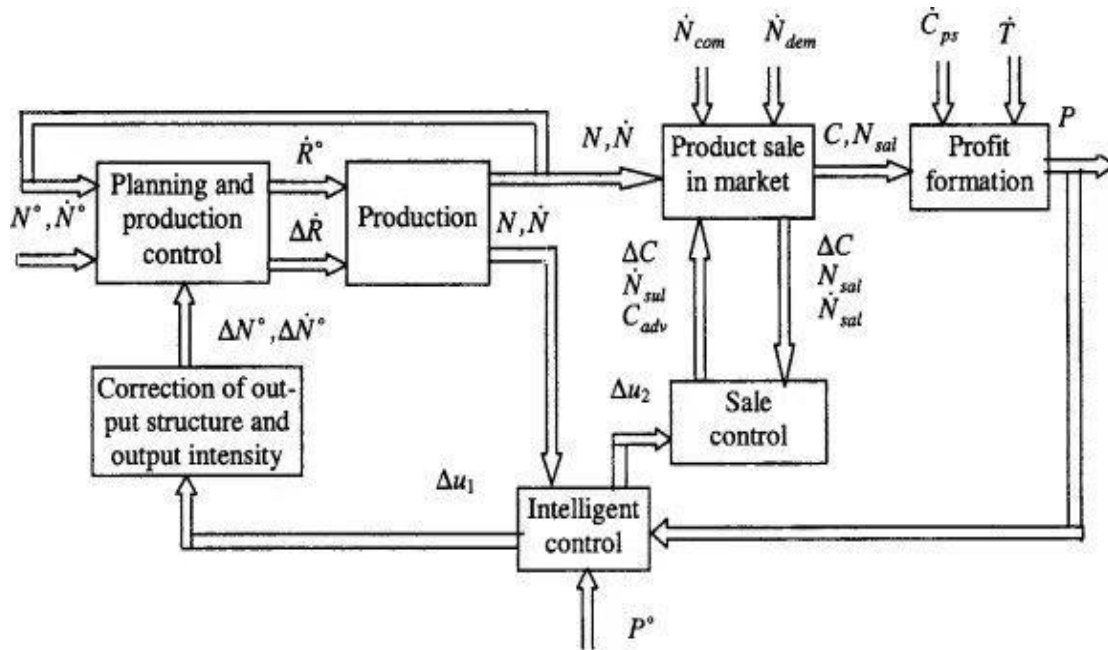


Fig 2: Intelligent Control

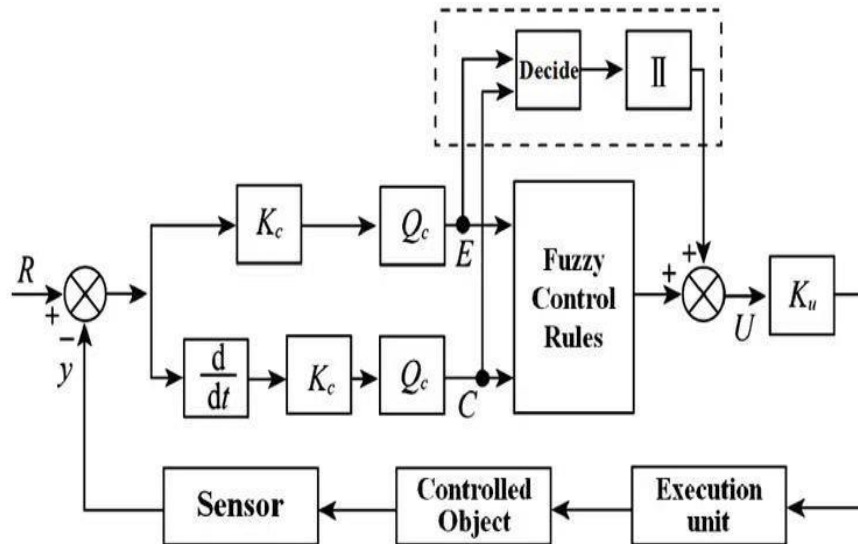


Fig 3: Fuzzy Control System

**1. Modeling and simulation:** Creating accurate and detailed models of the complex system is essential to understand its behavior and dynamics. These models can then be used to simulate different scenarios and assess the impact of various control strategies.

**2. Sensing and data acquisition:** Gathering real-time data and information from the complex system is crucial for intelligence control. This can involve using sensors, IoT devices, and other data collection methods to obtain information about the system's state, performance, and environment.

**3. Data preprocessing and analysis:** Raw data collected from the complex system needs to be preprocessed and analyzed to extract meaningful insights. This involves techniques such as data cleaning, feature extraction, and statistical analysis to transform raw data into relevant information.

**4. Decision-making and control algorithms:** Intelligent control algorithms are developed to make decisions based on the analyzed data and system models. These algorithms can range from simple rule-based systems to sophisticated machine learning algorithms that adapt and optimize control strategies over time.

**5. Feedback and adaptation:** Complex systems often exhibit dynamic and evolving behavior, requiring adaptive control strategies. Feedback mechanisms are incorporated into the control algorithms to continuously monitor the system's performance and make necessary adjustments in real-time.

**6. Human-machine interaction:** While the intelligence control algorithms automate many tasks, the involvement of human operators is still critical. Effective human-machine

interaction interfaces are developed to facilitate collaboration and decision-making between humans and intelligent control systems.

**7. Performance monitoring and optimization:** Monitoring the performance of the complex system and the effectiveness of the intelligence control is essential. Performance metrics and optimization techniques are used to evaluate the control strategies and identify areas for improvement.

Intelligence control for complex systems is applicable in various domains, such as manufacturing, transportation, energy, healthcare, and finance. It can help improve efficiency, safety, reliability, and overall performance of these complex systems.

**General control system intellectualization issues**

The efficacy of control systems and technologies being developed is critical to the successful resolution of problems to ensure the state's technological independence in the sphere of civil and military purpose complex technical object creation and application. There is adequate theory and control technology. Taking into consideration the possibility of a lack of specific (depending on the application) required resources: information, timing, energy, money, material, human, and so on. Accidents and disasters in transportation, industry, and energy are frequently related with the so-called "human factor" (HF), including operator overwork. HF frequently happens as a result of quality issues in control system design, particularly in controllability emergencies. Human errors, as well as the exhaustion of technical resources of objects and control systems, are all too typical in today's Russian environment. They urgently demand guaranteed control dependability and quality, as well as updates to project, operational, and

modernization control capacities. Under the following conditions, methodologies and technologies for evaluating control systems and ensuring their optimality, functional and operational dependability, efficiency, fault tolerance, and survival are required:

- a lack of prior knowledge about the control object and its external environment of operation, even in opposition conditions;
- a large number of stationarity elements that are difficult to account for due to their subjective nature;
- Degeneration (due to failures or accidents) or the requirement for focused reconfiguration (revitalizing or developmental control).

Control systems get significantly more difficult as functional burden increases. Among the complexity factors of modern and advanced control systems are:

- multilevel controls, heterogeneity in subsystem description by quantitative and qualitative models, different scales of processes in space and time, multimodality, multilink, decentralization, ramified nature, and general structural complexity of modern control systems and their control objects,
- presence of uncontrolled coordinate-parametrical, structural, regular, and singular impacts, including active counteraction in a conflict environment,
- Use of the non-linearity, dispersed parameters, delay in control or object dynamics, impulsive impacts, high model size, and other factors.

Adaptive, robust, predictive, and other control approaches established in control theory are meant to account for dynamics' incompleteness by receiving missing information during the training stage or in real time. The use of AI involves extending the capability of complicated control systems by addressing tasks that are unknown or quantifiable. Models that are no longer valid as of some point in time, as well as tasks where quantitative models are less efficient than using AI models (such as in action planning tasks) or can be used in conjunction with AI models [1]. For action planning tasks and control in general, a range of artificial intelligence approaches neuronal, evolutionary, logical, and others - can be applied.

Adaptive, robust, predictive, and other control approaches established in control theory are meant to take into account. Each of these classes has advantages and limitations, particularly in terms of real-time requirements, and ensures the implementation of higher levels of heterogeneous control over complex systems. The intensive development of technical

systems and technological processes (networking, miniaturization of sensors, controlling devices, and calculators, improving their performance, and so on) places new demands on modern control systems and opens up new opportunities, both at the level of embedded control systems of various scales and at the level of group interaction of decentralized multi-agent systems. The shift from robots operating in an unpredictable environment yet equipped with an operator interface. Current research and development is focused on the transition from robots operating in an unpredictable environment but equipped with an operator interface (supervisory UAVs) to intelligent robots. At that point, less expensive robots based on a modular concept of construction and miniaturization are required to solve sensitizing, environment modeling, robot control team goals, and application scope extension difficulties. Even in agricultural and road construction, drastic standards transformation demands robots with high-precision navigation and cognitive control.

Large-scale infrastructure systems in the electric power industry are examples of critically essential technological processes and intellectual control objects. In this situation,

- an inefficient structure of electrical grids and producing capacity,
- a lack of energy savings in electricity usage,
- technological and commercial losses in electric networks,
- technological lag and excessive equipment wear,
- a high level of monopolization in power markets,
- Vulnerability of electric power networks to terrorist and cyber attacks,

And other factors necessitate the development of models of complex infrastructure dynamic systems and the development of efficient solutions and highly dependable intelligent control systems for smart grids [4-6].

Control based oenological-reactive (production) knowledge model in the so-called expert, recommender or systems that help decision-making that need to be improved with new features:

- collaborating with other intellectualization techniques for control systems (artificial neural networks, genetic algorithms, and adaptive, resilient, and predictive control algorithms),
- By combining methods of symbolic and multimedia presentation and knowledge processing,

- operating with partially formalized and natural language texts, abductive and inductive knowledge updating,
- Integrating quantitative and qualitative models with ontologies of various subject domains that characterize the problem situation, logical control systems' interface complexity with the outside physical world can be reduced.

There are numerous methods to combine various AI techniques. For instance, the 1-st order logical techniques of intellectual control from [1,7] can be linked with the neuro-reactive and logical-reactive (productional) AI means. While the first two strategies promote "reasonable" conduct, the latter methods can address a wider range of information. Based on giving the control system's simplest heuristic responses for changes to the environment or the controlled object. Verification of knowledge presentation is especially important at the logical-reactive level (sometimes with its many "if-then" rules). The verification of a knowledge base can be reduced to the dynamic analysis of automata networks in the case of production rules of the Boolean type and constructive semantics. This analysis is further condensed in the class of monotonous automata with respect to the state the state by application of method of mathematical model's properties transfer [8].

The important problem in AI is the problem of automatic estimation of irrelevance of knowledge, because not only a deficit but also a surplus of information causes degradation of intellectual control systems. Recent advances in the field of intellectual control include the automation of searching for ways to achieve the control goal given externally, while the automation of goal-setting and revision of control quality criteria is not sufficient yet. It is now also recognized that improvement of only "machine components" in developed human machine systems is not enough for the desired essential increase of their use the efficiency. This goal in creating anthropocentric systems can be achieved by directing the efforts of engineers and scientists on improving the intellectual component of the "system-core" in anthropocentric system as built-in set of algorithms for embedded computers together with algorithms of operator activity, referred to as "on-board intelligence" [8,9]. First and foremost the on-board intelligence is required in aviation, especially in combat situations, typical for fighters, i.e. in the circumstances of the most aggressive external environment and tight timing constraints for the crew. On-board intelligence is a functionally integral complex, aimed at the fulfillment of all aircraft tasks [9]. Scientific and technological advances in this field will be useful also in other applications of AI in the conditions of a multicriticality, uncertainty and risk to improve control quality in a situation of information overloading the

operator, limited time or stress. Development of practically useful on-board decision-making support expert systems, including those based on fuzzy logic and case-based reasoning by analogy, has reached the practical stage of building the models and prototypes. They are intensively developed in the world in favor of the creation of the manned combat aircraft of the 4++ and 5th generations, as well as combat UAVs. Their fragments already appear on the modernized fighters of 4++ generation. In foreign developments, they are planned to be used, first of all, on board of the new USA fighters F-22, F-35, modernized F-16, F-15, F/A-18 and helicopters, which have a number of on-board intellectual systems of tactical decision making [9]. The results of the research, the improvement of on-board computers, cockpit displays and controls as well as other avionics give the constructors of next generation aircraft / helicopter an opportunity to design and realize a-board computer systems of a new type. These systems will be capable to support tactical decisions making (the prompt appointment of the current purpose of flight and choice of a rational way of achieving the goal). Solving such tasks on past generations aircraft could be only completed by the efforts of the crew. Further we consider in details some questions of intellectualization of automatic control systems in the form of fuzzy regulators and combining them with other AI means. Note that the first regulators developed in Greece in the 3rd century BC partly can be considered as the fuzzy controllers described linguistically with logical operations. Today, a huge number of practical applications of fuzzy control systems in the industry, transport, energy, oil and gas, metallurgy, medicine and other industries and household appliances can be observed in Japan, China, USA Germany, France, Britain, Russia and other countries. We consider four basic types of regulators: logical-linguistic, analytical, learned and proportional-integral differential (PID) fuzzy controllers [1, 7, 11-17]. Since the information about them is not systematized and is scattered in many publications, our analysis will help a specialist to orient himself in this field.

### III. CONCLUSION

intelligence control for complex systems involves employing advanced algorithms and techniques, including artificial intelligence and machine learning, to effectively manage and manipulate complex systems. The key components of intelligence control include modeling and simulation, data acquisition and preprocessing, decision-making and control algorithms, feedback and adaptation, human-machine interaction, and performance monitoring and optimization. By using intelligence control, we can better understand the behavior of complex systems, make

informed decisions based on real-time data and system models, and adapt control strategies in real-time. This can lead to improved efficiency, safety, reliability, and overall performance of complex systems in various domains.

Intelligence control is a vital area of research and development as we continue to face increasingly complex systems in our modern world. With advancements in technology and the availability of large amounts of data, intelligent algorithms have the potential to greatly enhance the management and control of these complex systems, leading to better outcomes and more efficient operations.

## REFERENCES

- [1] Yev SN, Zherlov AK, Fedosov EA, Fedunov BE. Intelligent control of dynamical systems. M.: Fizmatlit; 2000. 352 p.
- [2] Russell SJ, Norvig P. Artificial Intelligence: A Modern Approach. Prentice-Hall, Inc., 1995.
- [3] Pupkov KA. Some results of development of scientific-technical program "Intellectual systems" of FKP "Universities of Russia" // Proceedings of the 2 International. Symp. "Intellectual systems" (INTELS'96). 1996; 1:5-9.
- [4] Vassilyev SN, Yadykin IB, Morgin YuI., Voropai NI, Efimov DN. Intelligent operating and emergency control technologies in Russia CD Proceedings of the 2th IEEE PES International conference and Exhibition on «Innovative Smart Grid Technologies – Europe» (ISGT 2011 Europe, Manchester). Manchester: University of Manchester, 2011. p. 1-7.
- [5] Berdnikov RN, Bushuev VV, Vassilyev SN, etc. The concept of intellectual power system of Russia with actively adaptive network. Ed. by V. E. Fortov, A. A. Makarov. M.: JSC "FGC UES"; 2012. 235 p.
- [6] Vassilyev SN, Voropai NI, Rabinovich MA, Yadykin IB. Unified energy system of Russia: intellectual solutions. Energy of development. 2012; 2: 48-57.
- [7] Vassilyev SN. Formalization of knowledge and control on the basis of positively-formed languages. Information technologies and computing systems 2008; 1: 3-17.
- [8] Fedunov BE. On-board operatively advising expert systems of tactical level for manned aircraft. International aerospace magazine "Aviapanorama" 2016; 1: 9-20.
- [9] Zheltov SYu, Fedunov BE. Operational goal-setting for anthropocentric objects from the point of view of the conceptual model "Etap", I, II Izv. Russian Academy of Sciences. TiSU. 2015; 3: 57-71; 2016; 3, 55-69.
- [10] Aliev RA, Abdikeev NM, Shakhnazarov MM, Production system with artificial intelligence. M.: Radio and communication; 1990. 264 p.
- [11] Kudinov YI. Fuzzy control system, Izv. USSR ACADEMY OF SCIENCES. Technical Cybernetics. 1990; 5: 196-206.
- [12] Kuzmin VB, Travkin SI. Theory of fuzzy sets in control problems and principles of the device of fuzzy processors: a Review of foreign literature. Automatics and telemechanics. 1992; 11: 3-36.
- [13] Zakharov VN, Ulyanov SV. Fuzzy models of intelligent industrial controllers and control systems. I. Scientific-organizational, technical, economic and applied aspects, Izv. Russian Academy of Sciences. Technical Cybernetics. 1992; 5: 171-96.
- [14] Zakharov VN, Ulyanov SV. Fuzzy models of intelligent industrial controllers and control systems. II. Evolution and principles of construction, Izv. Russian Academy of Sciences. Technical Cybernetics. 1993; 4: 189-205.
- [15] Zakharov VN, Ulyanov SV. Fuzzy models of intelligent industrial controllers and control systems. III. Design methodology, Izv. Russian Academy of Sciences. Technical Cybernetics. 1993; 5: 197-220.
- [16] Zakharov VN, Ulyanov SV. Fuzzy models of intelligent industrial controllers and control systems. IV. Simulation modeling, Izv. Russian Academy of Sciences. Technical Cybernetics. 1994; 5: 169-211.
- [17] Zadeh LA. The Concept of linguistic variable and its application to making approximate decisions. M.: Mir, 1976. 165 p.

# Technical and Economic Assessment of the Integration of Refrigeration Concepts into the Proceeding Extension of Solar Energy Systems in Brazil

Christopher Wiencke<sup>1</sup>, Giovani Ávila<sup>1,\*</sup>, Katja Biek<sup>2</sup>

<sup>1</sup>Universidade Federal do Rio de Janeiro, Brasil, christopher.wiencke@poli.ufrj.br

<sup>2</sup>Berlin University of Applied Sciences and Technology, biek@bht-berlin.de

\* Correspondence: giovani@poli.ufrj.br

Received: 11 Dec 2023,

Receive in revised form: 15 Jan 2024,

Accepted: 25 Jan 2024,

Available online: 04 Feb 2024

©2024 The Author(s). Published by AI Publication. This is an open access article under the CC BY license (<https://creativecommons.org/licenses/by/4.0/>)

**Keywords**— solar energy; self-generation; solar powered cooling

**Abstract**— Electricity is the main source used in the refrigeration process of environments and machines. Global warming and the expansion of the tropical belt increase the demand for refrigeration. The use of solar-assisted air conditioning has a great potential, especially in subtropical regions with high solar radiation contributing to demand's fulfillment and reducing electricity from non-renewable sources. It has cooling potential in buildings reducing electricity's peak demand, ecological footprint reducing carbon emissions and building's thermal load using ecological refrigerants. Also benefits the urban microclimate absorbing solar irradiation into the rooftop. The objective of this article is to survey the factors that influence the selection of components for a solar-assisted cooling system in buildings under different climatic conditions using an exploratory methodology based on the bibliography and on a survey of the state of the art describing the fundamental aspects and components of this technology, its function, and benefits. Non-thermally driven applications were also considered, such as conventional steam compression chiller, driven by electricity and compression cycle by photovoltaic energy. Different cooling systems at full load are compared. The research was applied in a school building in the city of Rio de Janeiro, concluding that solar-assisted refrigeration is an energetic and environmentally competitive alternative compared to compressors powered by electricity in conventional refrigeration systems.

## I. INTRODUCTION

The cooling process of environments present an increasing energy demand due to global warming, desertification, and the expansion of the tropical belt as Figure 1. In subtropical regions, a high supply of solar radiation and a high demand for cooling occur simultaneously.

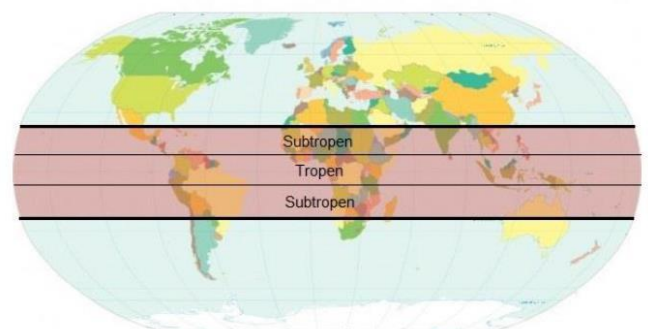


Fig.1. Tropical Belt.

The solar cooling provides a significant potential of an electrical energy reduction for air-conditioning in buildings, arranges fossil fuel savings and decreases peak demands of electrical energy.

Furthermore, solar cooling decreases the ecological footprint of tropical cities due to achieving carbon emission reduction and using environmentally friendly refrigerants. The solar array yields thermal load reduction of the building.

Finally, it impacts in a positive way the urban microclimate through absorbing the solar irradiation on the roof as in Figure 2.



Fig.2. Thermal Solar Array and Split Coolers with Compressor Operation.

Solar cooling systems (SCS) have the advantage that the maximum solar radiation corresponds to the maximum cooling demand in residential buildings.

SCS offer potential to reduce electricity consumption for building cooling and environmental footprint due to reduction in carbon emissions and use of ecological

refrigerants. In addition, the technology has a positive impact on peak electricity demand associated with conventional cooling, the need for transmission and distribution networks, and the ability to cool at night using thermal storage.

The following are factors that influence the selection of components for a solar-assisted cooling system in buildings.

The basic characteristics of equipment supported by solar energy in buildings, conventional compression equipment powered by electricity and photovoltaic energy.

### 1.1. Solar Energy

Brazil receives solar energy in the order of  $10^{13}$  MWh per year, which is about 50.000 times the country's annual consumption of electricity, as in Figure 3 [2].

The country has an average solar radiation of 5 kWh/(m<sup>2</sup> day) and a cooling demand up to 200 W/m<sup>2</sup>.

In Europe, where the most solar cooling systems are in operation, the average solar radiation is around 3 kWh/m<sup>2</sup>/day.

## II. KNOWLEDGE BASE

In system modeling the recommendation of the technology is a function of the characteristics and survey of which techniques are available and are more efficient for the specific case. It is necessary to determine the correlation between solar energy supply and cooling demand. Solar energy can be converted into cooling using two principles: (1) Heat generated by solar thermal collectors can be converted into cooling using thermally driven chiller using physical sorption phenomena in a thermodynamic cycle; (2) electricity is produced in photovoltaic modules and can be converted into cooling using steam compression cycles. Figure 4 shows the first principle, heat-driven cooling systems that are usually applied for residential comfort cooling and so-called LowEx concepts. The second principle – solar electricity driven cooling (PV cooling) – is not commercially widespread, but frequently used to run solar driven refrigerators for cooling medicine in remote, sunny regions [2].



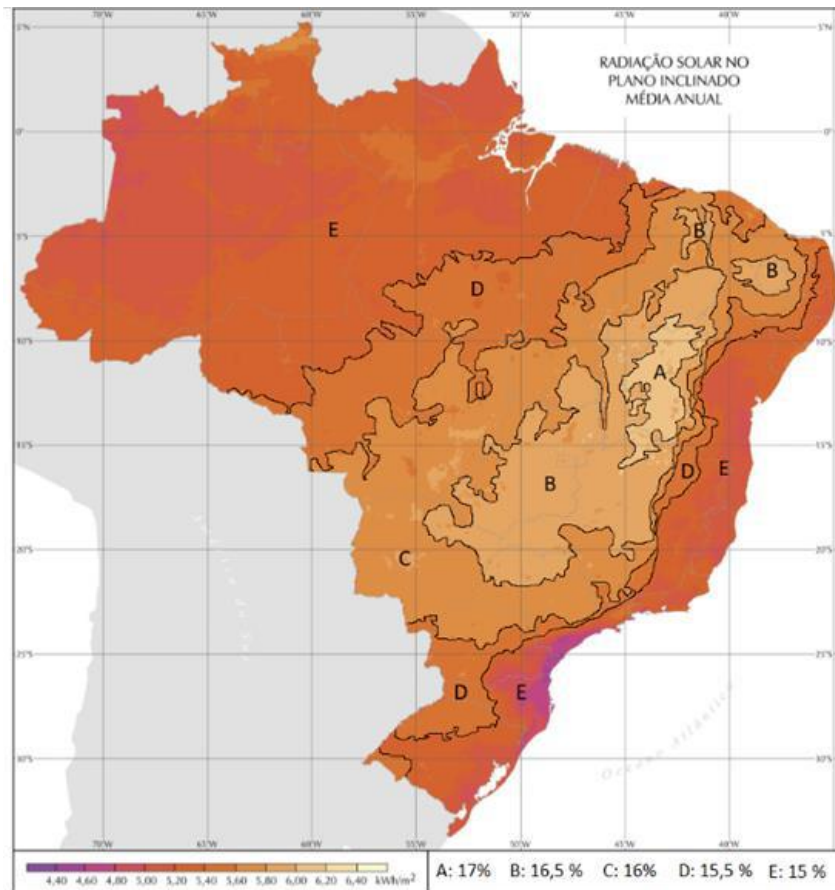


Fig.3. Annual average solar irradiance in Brazil.

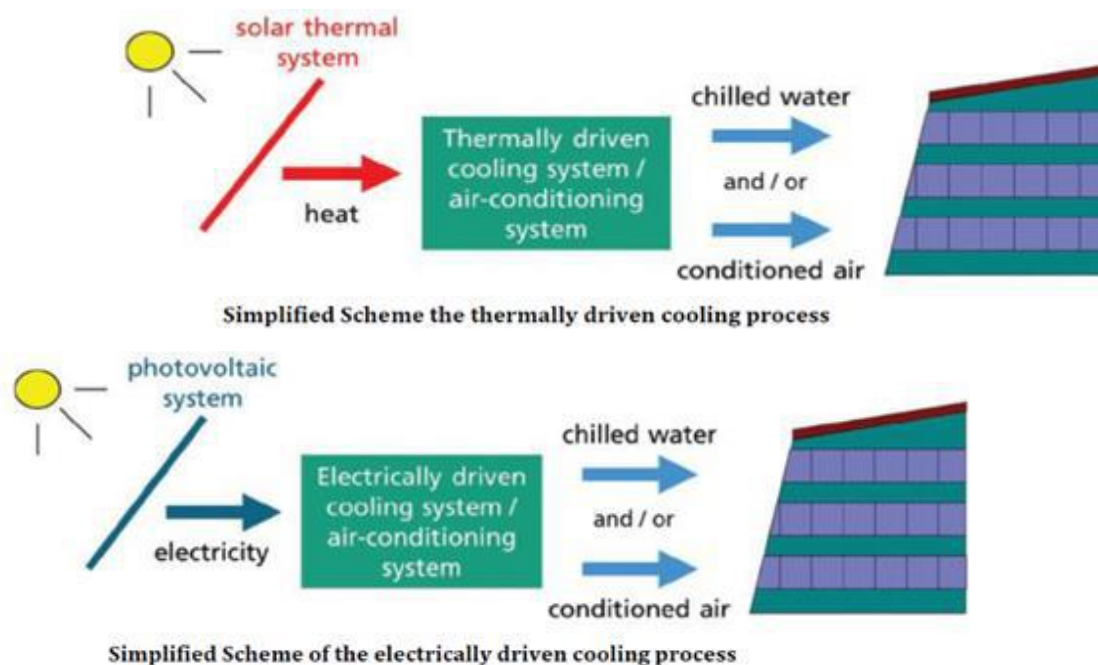


Fig.4. Schemes of SCS driven thermally and electrically [1], [8], Adapted.

Brazil’s National Electric Energy Agency has passed a law requiring energy distributors to inject generated

electricity into the grid. Brazil receives solar energy in the order of 1013 MWh per year, which is about 50,000 times

its annual electricity consumption. Its average solar radiation is 5 kWh/(m<sup>2</sup>day) and a cooling demand of up to 200 W/m<sup>2</sup>. In Europe, the average solar radiation is about 3 kWh/(m<sup>2</sup>day) and the cooling demand is only 40-70 W/m<sup>2</sup>. These data show the good conditions for solar refrigeration applications in Brazil [3].

2.1. Solar Thermal Collector

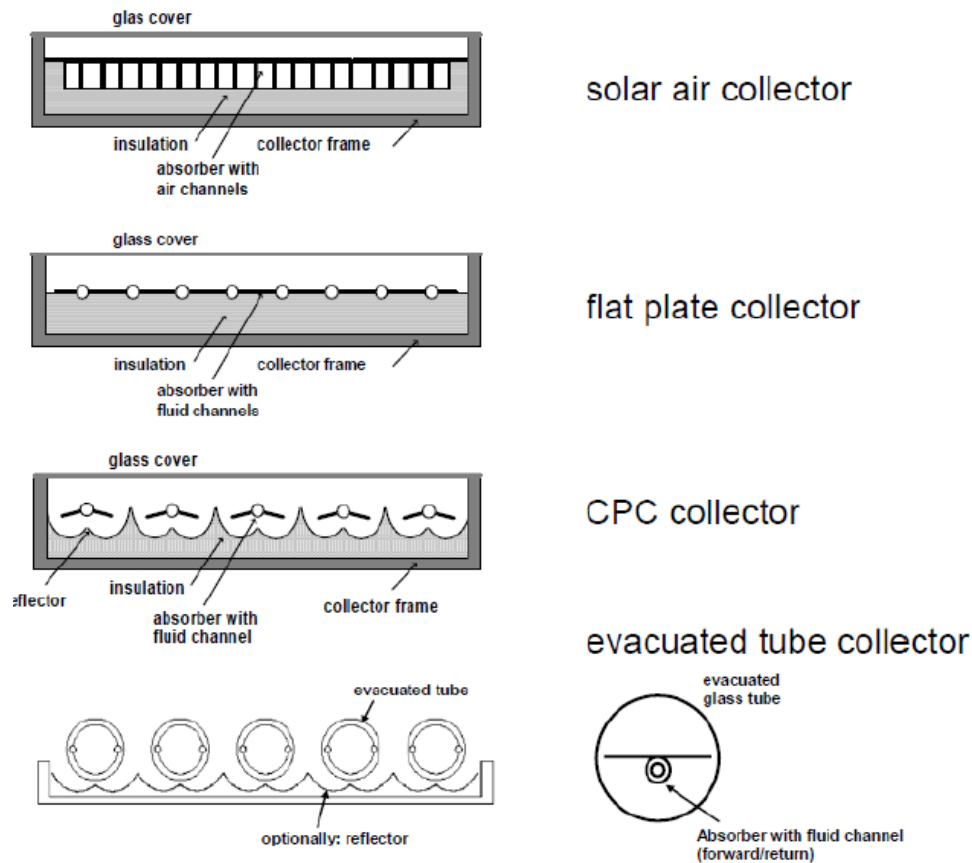


Fig.5. Types of stationary solar collectors, applicable in refrigeration [1].

The flat collector is applicable in the temperature range of up to 90°C. Heat losses are minimized by enhanced insulation and an additional convection barrier (Teflon sheet) between the glass cover and the absorber. The use of solar air collectors in the construction of flat plates is limited to descant cooling systems since this technology requires the lowest driving temperatures (from approx. 50°C) and allows under special conditions the operation without thermal storage. To operate thermally driven chillers with solar heat, high-quality flat plate collectors (selective

In Brazil a variety of solar thermal collectors is available in the market, and several are used in refrigeration systems. The appropriate type of collector depends on the selected cooling technology and local conditions, especially radiation availability. The general types of stationary collectors are shown in Figure 5

coating, improved insulation, high stagnation safety) [3]. Figure 6 shows two principles of vacuum tube collectors. On the left, the classic principle is shown, requiring a vacuum-tight seal. In the center, the principle of the thermos is shown [1]. On the right the application of the heat tube principle. The tube is protected from freezing and stagnation. There is a variety of vacuum tube collectors, for example, collectors with direct flow of the collector fluid through the absorber tube. The glass tube can follow the traditional principle, sealed at both ends, or the thermos principle. [4].

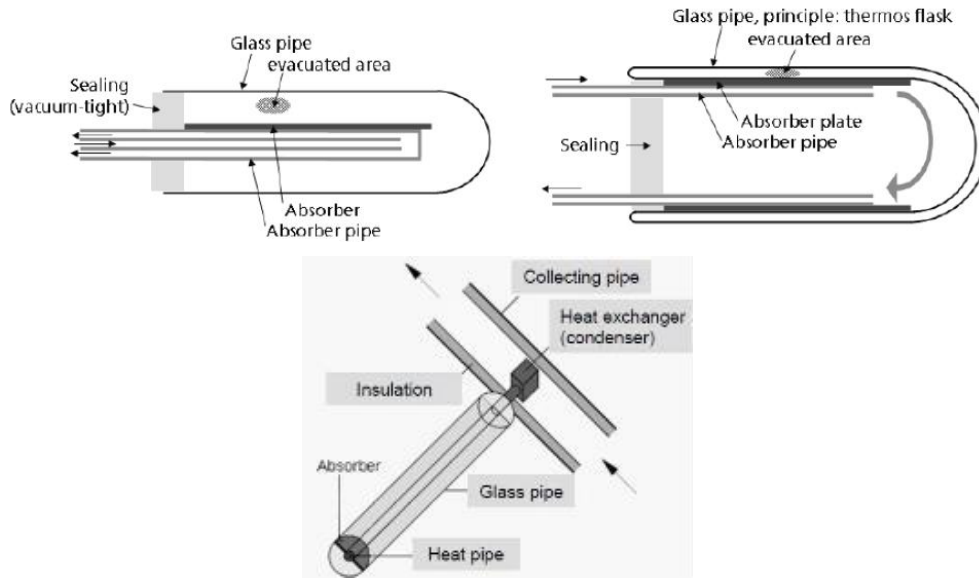


Fig.6. Different constructions of vacuum tube collectors [1].

Henning [5] raised the characteristics and Reichhardt [3], the costs of thermally driven refrigerators in the Brazilian market.

2.2. Photovoltaic

A photovoltaic (PV) system consists of an arrangement of components to absorb and convert sunlight into electricity. The largest PV systems are connected to the network while the small ones normally don't. It is possible to operate a cooling system using a PV system. Two technical solutions can be used for SCS with photovoltaic systems: (1) Electricity-based system, connected to the grid, for indirect operation of the chiller with energy compensation. The

investment cost is about €3,000/kW (material only, 2017); (2) Electricity-based system for direct coupling with chiller for cooling food and medicines being sometimes the only solution in remote areas [3]. Figure 7 shows a comparison between a direct coupling photovoltaic system and a solar thermal system, indicating the COP (performance coefficient) and the efficiency of each system. The COP of the solar system/sorption can be increased using a collector with greater efficiency, for example, some special types of vacuum tube collectors have a maximum efficiency of 60% to 90°C of water temperature. Normal flat plate collectors with selective coating have efficiency at this temperature level of only 40% [3].

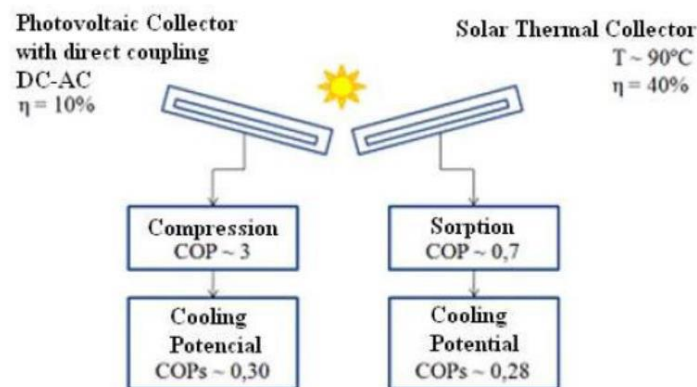


Fig.7. COP comparison and efficiency between a direct coupling photovoltaic system and a solar thermal system [6].

2.3. Cooling Systems

SCS uses heat in a heat-driven cooling process. Within SCS, there are two main processes: (1) closed cycles, where thermally driven absorption and adsorption produce chilled water for use in ambient conditioning equipment (air

handling units, fan coils, chilled beams, etc.); Open cycles, also called desiccant evaporative cooling systems (DEC), typically use water as a refrigerant and a desiccant as a sorbent for direct air treatment in a ventilation system. For closed cycle systems, Figure 8, there are two types of

sorption processes: adsorption and absorption-based systems. Based on closed cycle sorption; the basic physical process that underpins both technologies consist of two chemical components, serving as refrigerant and sorbent.

The water from the chiller is produced and transferred to the decentralized units such as fan coils, chilled ceiling, or AHU [1]. The efficiency of closed cycle systems may vary depending on the driving temperature.

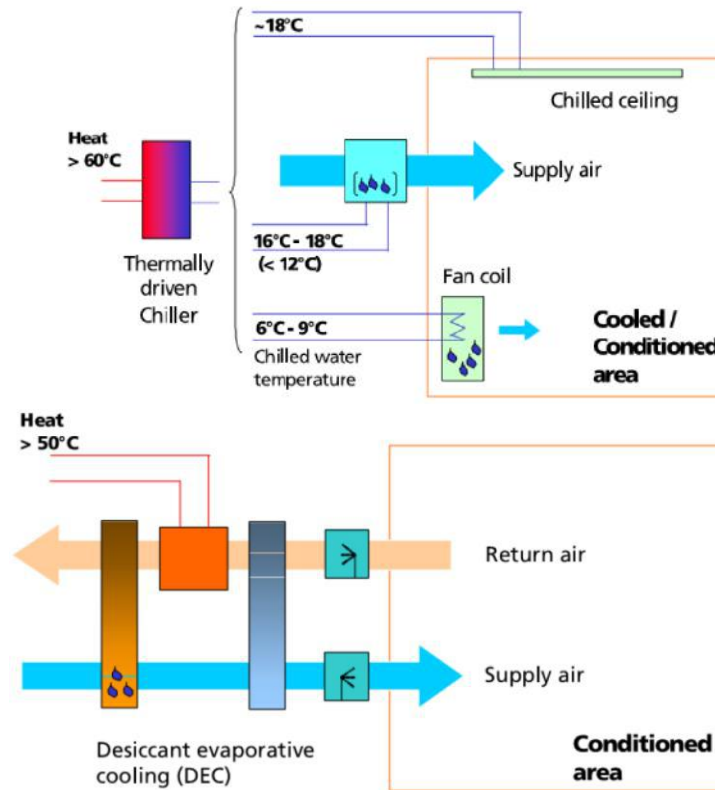


Fig.8. Closed cycle system at the left and open cycle system at the right.

While closed cycle systems produce chilled water open cooling cycles produce air conditioning directly. Thermally driven open cooling cycles are based on a combination of evaporative cooling and air dehumidification by a desiccant (a hygroscopic material that absorbs moisture), Figure 6. The supply air is cooled and dehumidified directly in an air handling unit (AHU) [7]. Desiccant cooling systems are an option with centralized ventilation systems offering the ability to pre-condition the air that enters a room. Open cycle SCS offers humidity management as well as space cooling. Solar thermal cooling does not use refrigerants (CFCs and HCFCs, used in electric compression chillers). Recent technology is desiccant cooling (DEC) where air is conditioned directly, e.g., cooled, and dehumidified, exploit the potential of sorption materials for air dehumidification - such as silica gel. In an open cooling cycle, this dehumidification effect is used for two purposes: to control the

humidity of the ventilation air in air-handling units and reduce the supply temperature of ventilation air by evaporative cooling [5].

2.3.1. Absorption Chiller

Absorption chillers use heat to provide cooling. Thermal compression of the refrigerant is obtained using a liquid refrigerant/sorbent solution and a heat source, thus replacing the electrical energy consumption of a mechanical compressor. For chilled water above 0°C, as it is used in air conditioning, a liquid H<sub>2</sub>O/LiBr solution is applied with water as a refrigerant. Most systems use an internal pump that consumes little electricity. The main components of absorption chillers are shown in Figure 9. Absorption cycles are originating from the fact that the boiling point of a mixture is higher than of a pure liquid.

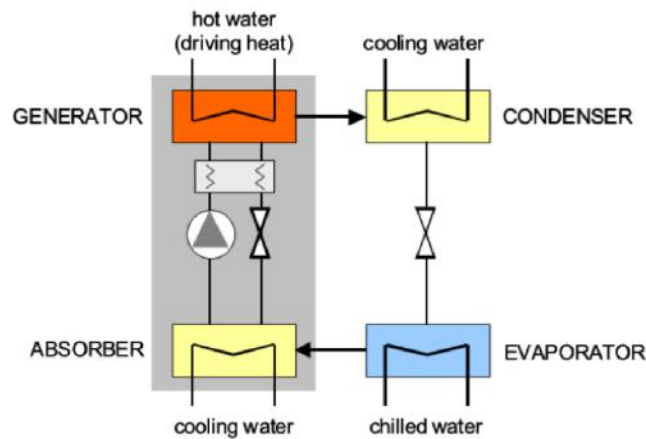


Fig.9. Scheme of an absorption chiller [1].

The thermal coefficient of performance (COP<sub>th</sub>) is the useful cold ratio per heat unit:

$$COP_m = Q_{cold}/Q_{drive} \quad (1)$$

Where  $COP_m$  = thermal coefficient of performance,  $Q_{cold}$  is the useful cold, and  $Q_{drive}$ , driving heat.

An absorption cycle includes the following steps [1]:

The refrigerant evaporates in the evaporator, thereby extracting heat from a low-temperature heat source. This results in the useful cooling effect.

The refrigerant vapor flows from the evaporator to the absorber, where it is absorbed in a concentrated solution. Latent heat of condensation and mixing heat must be extracted by a cooling medium, so the absorber is usually water-cooled using a cooling tower to keep the process going.

The diluted solution is pumped to the components connected to the driving heat source, desorber, where it is heated above its boiling temperature, so that refrigerant vapor is released at high pressure. The concentrated solution flows back to the absorber.

The desorbed refrigerant condenses in the condenser, whereby heat is rejected at an intermediate temperature

level. The condenser is usually water-cooled using a cooling tower top reject the "waste heat".

The pressure of the refrigerant condensate is reduced and the refrigerant flows to the evaporator through an expansion valve.

Figure 10 shows the processes of the thermal absorption cycle.

The left arrangement presents the steam pressure as a function of the steam temperature in an absorption cooling cycle process [1]. On the right we can see the detailed functional scheme of a single-effect absorption chiller "Carrier" [9].

The required temperature of the heat source is usually above 85°C and typical COP values are between 0.6 and 0.8. Until a few years ago, the smallest machine available was a Japanese product with a cooling capacity of 35 kW (10 TR).

Recently, refrigeration products in the small and medium capacity range have entered the market. In general, they are designed to operate with low driving temperatures and therefore applicable to stationary solar collectors.

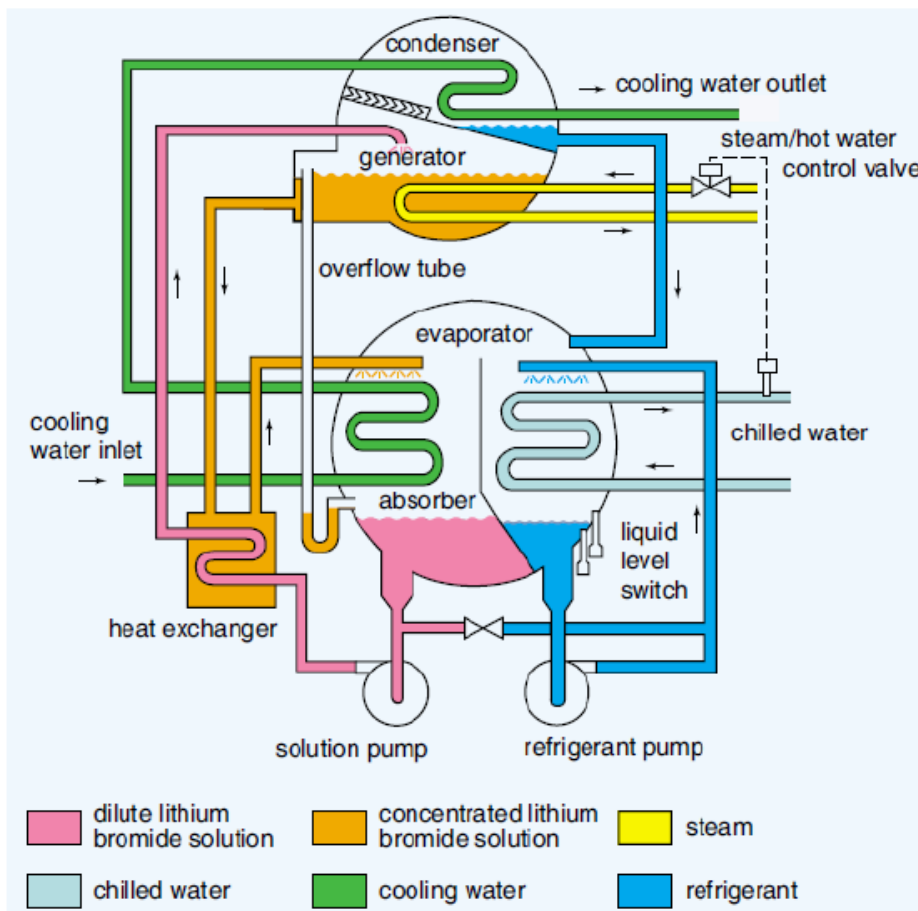
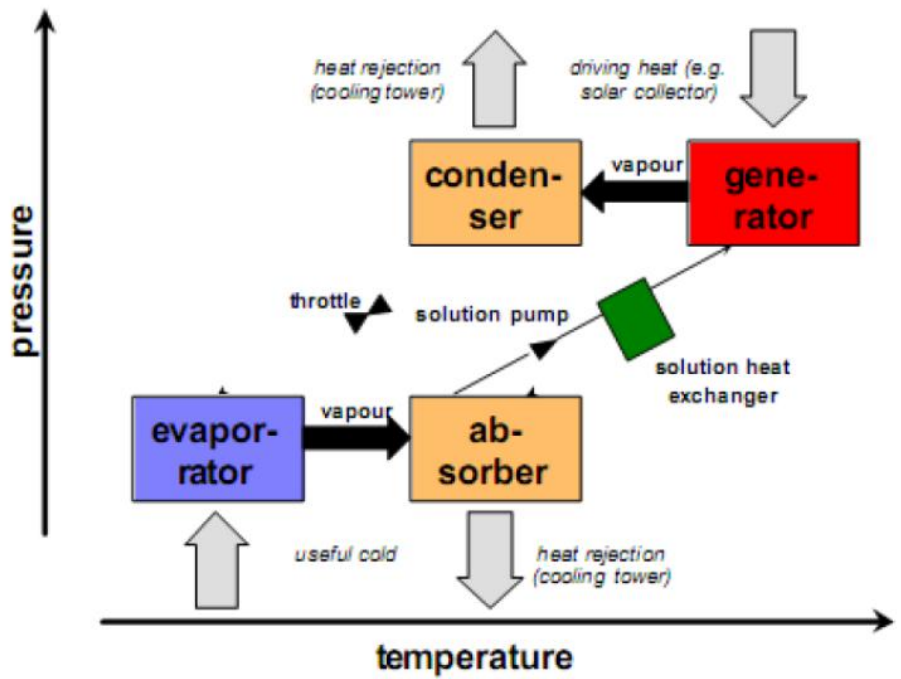


Fig.10. Thermal absorption cycle [9].

2.3.2. Conventional Compression Chiller

The most common cooling process applied in air conditioning is the steam compression cycle. The process

employs a chemical refrigerant, for example, R134a. A system's schematic drawing is shown in Figure 11.

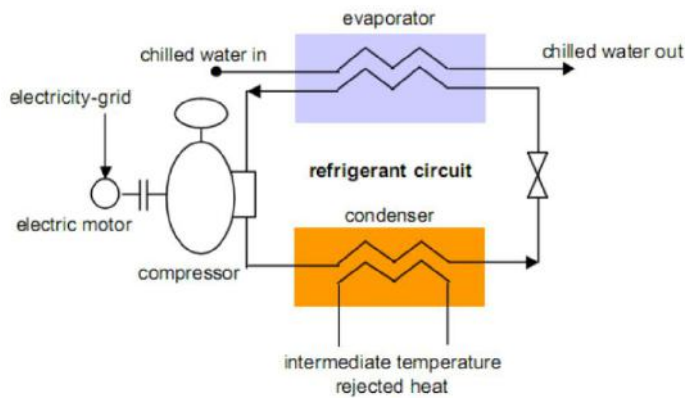


Fig.11. Schematic design of a steam compression chiller [7].

In the evaporator refrigerant evaporates at low temperature. Heat extracted from the external water supply is used to evaporate the refrigerant from the liquid phase to the gaseous phase.

External water is cooled than cooling energy becomes available. The key component is the compressor, compressing the refrigerant from a low to a higher pressure and temperature in the condenser [8].

For a conventional electrically charged steam compression chiller (COP) it is defined as follows:

$$COP = Q_c / P_{el} \tag{2}$$

Where  $Q_c$  = cooling capacity [kW] and  $P_{el}$  = electricity input [kW].

### 3. Case Study "Escolinha Tia Percila"

It is intended to equip the spaces of an elementary school with an air conditioning system assisted by solar energy. The school was founded in 1991 by the Street Children Foundation, a Swedish organization founded in 1993 to finance projects for needy children in several countries and in Rio de Janeiro, the favelas of Babilônia and Chapeu-Mangueira.

This case study was carried out within an NGO “Revolusolar” to obtain environmental benefits from solar energy, together with GIZ (German Corporation for International Cooperation) whose mission in Brazil is to strengthen the role of renewable energy sources.

At first, the technical and structural conditions of the school building were verified and then data was collected. The solar coverage rate was calculated using the HVAC Load software [14] determining the cooling load supporting the analysis of different SCS systems, the inventory and budget for the installation enabling the technical, economic, and environmental evaluation and the return on investment.

The building analysis provided information on energy efficiency potential. At the same time, measures were identified to reduce electricity consumption. The city of Rio de Janeiro is in Brazil’s southeastern with geographic coordinates 22°48’43" S and 45°11’40" W. It has a tropical savannah climate bordering a tropical monsoon climate. It presents long periods of heavy rain from December to March. Temperatures above 27°C are normal throughout the year and above 40°C are common during summer [10] as Table 1.

Table 1. Climate data for Rio de Janeiro.

| Month          | Temperature [°C] | Humidity [%] | Pressure [mb] | Precipitation [mm] | Sunshine-hours [h] |
|----------------|------------------|--------------|---------------|--------------------|--------------------|
| January        | 30,2             | 79           | 950,5         | 137,10             | 211,9              |
| February       | 30,2             | 79           | 951,4         | 130,4              | 201,3              |
| March          | 29,4             | 80           | 951,9         | 135,8              | 206,4              |
| April          | 27,8             | 80           | 953,8         | 94,9               | 181                |
| May            | 26,4             | 80           | 955,1         | 69,8               | 186,3              |
| June           | 25,2             | 79           | 957,0         | 42,7               | 175,1              |
| July           | 25,0             | 77           | 957,9         | 41,9               | 188,6              |
| August         | 25,5             | 77           | 965,5         | 44,5               | 184,8              |
| September      | 25,4             | 79           | 955,2         | 53,6               | 146,2              |
| Oktober        | 26,0             | 80           | 952,6         | 86,5               | 152,1              |
| November       | 27,4             | 79           | 951,5         | 97,8               | 168,5              |
| Dezember       | 28,6             | 80           | 950,3         | 134,2              | 179,6              |
| <b>Average</b> | <b>27,3</b>      | <b>79,1</b>  | <b>953,6</b>  | <b>89,10</b>       | <b>181,82</b>      |

The building has five floors with a terrace that offers space for solar thermal installations. The eleven rooms have a usable area of 240 m<sup>2</sup> and an average ceiling height of 2.8 m. The façade is southeast oriented and has a large window

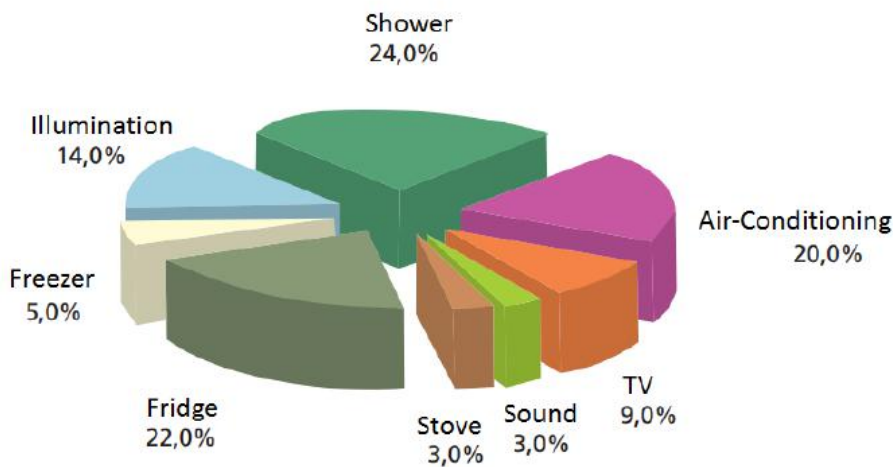
area. The canteen is located on the first floor and the perforated bricks allow convection heat to leak through via stack-effect during meals. Figure 12.



Fig.12. “Escolinha Tia Percilia”, canteen and classrooms.

All equipment and characteristics of the school's building materials were inventoried and classified by age, condition and energy consumption using specific catalogues, making it possible to determine the building's energy efficiency. Classrooms and administration rooms have

windows, air conditioning and fans. The annual electricity consumption is 15,700 kWh and the annual cost is around €2,000 (2017). Refrigeration costs represents 61% as can be seen in Figure 13. Table 2 lists air conditioners installed and monthly consumption.





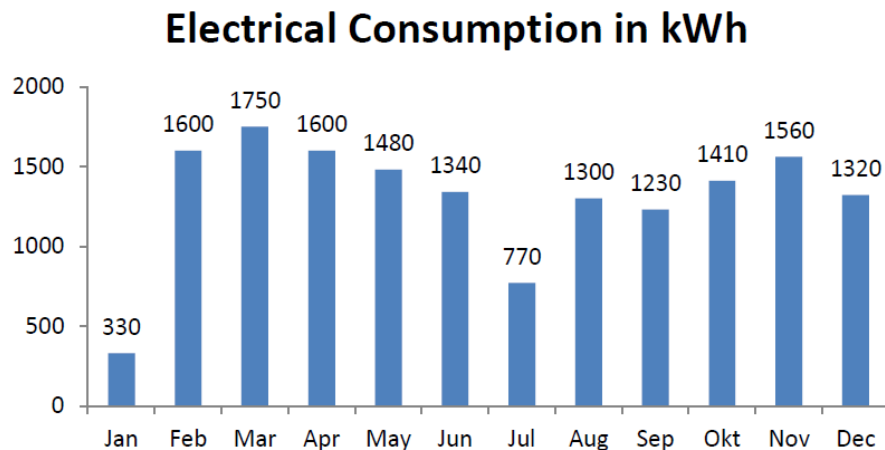


Fig.13. Electrical consumption by device in school and monthly Eletrical Consumption in kWh over the year in School Tia Percila.

Table 2. Air conditioning units installed and power consumption.

| Room  | Brandt | Model    | COP (*) | Power (kW)* | Consumption (kWh)** | Service (h/m)*** | Service (h)*** | Consumption (kWh/month) |
|-------|--------|----------|---------|-------------|---------------------|------------------|----------------|-------------------------|
| -2.1  | Elgin  | ERF30000 | 2.72    | 2.3         | 67.8                | 22.0             | 6              | 298                     |
| -1.1  | Elgin  | ERF30000 | 2.72    | 2.3         | 67.8                | 22.0             | 6              | 298                     |
| -1.2  | Consul | CCO10B   | 3.02    | 0.7         | 20.4                | 22.0             | 6              | 90                      |
| 0.1   | Gree   | GJE10AB  | 3.03    | 0.7         | 21.4                | 22.0             | 7              | 110                     |
| 0.2   | Elgin  | ERF30000 | 2.72    | 2.3         | 67.8                | 22.0             | 6              | 298                     |
| 2.1   | Consul | CCM12D   | 3.08    | 0.8         | 23.9                | 22.0             | 7              | 123                     |
| Total |        |          |         |             |                     |                  |                | 1217                    |

\*Manufacturer's technical data sheet; \*\*Energy consumption researched "Procel" [11]; \*\*\*Daily operating time.

Weather and operating time impact electricity consumption which is low in January and July due to school holidays. In winter consumption is low. Cooling a dense environment in compliance with the NBR 16401-3 standard is a challenge. The users' misbehaviours leads to the waste of energy, hence education and awareness are needed. There must be a renewal of the air to avoid the concentration of toxic gases and odors. Due to the lack of resources to install exhaust fans, the programmed opening of the windows was adopted, and the consequent thermal loss was considered in

the calculation of the cooling load. In the canteen, the air is renewed through perforated bricks. Analysing the building's thermal behaviour, the calculation obtained information about the maximum cooling demand during the hottest average day. The thermal load was calculated using the building simulation program "HVAC Load Explorer" [14]. The input data for the external and internal cooling load must be defined and added. The main influencing factors are shown Figure 14.

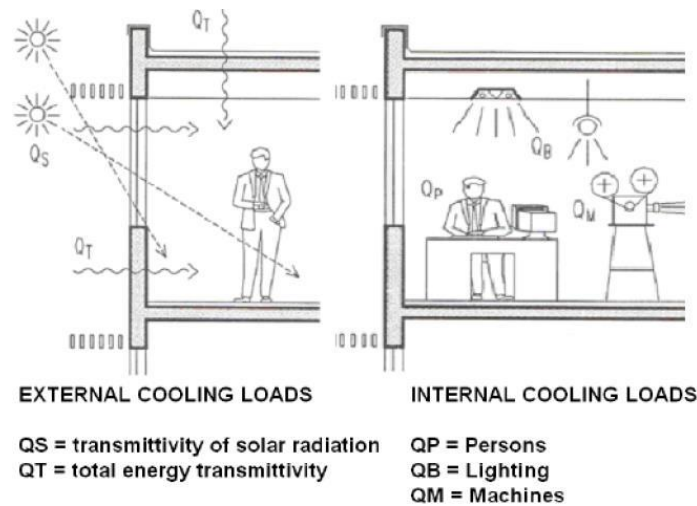


Fig.14. External and internal cooling loads [12].

Table 3 lists the dimensions of the spaces considered. Table 4 shows information for the case of 0.4% of unattended days corresponding to the worst probability [7] of meteorological data input “Escolinha Tia Percila”, Rio de Janeiro.

Table 3. Relevant spaces for the cooling load calculation and, meteorological data input [7].

| No.  | Room       | a(m) | b(m) | h(m) | A(m <sup>2</sup> ) | V(m <sup>3</sup> ) | Latitude              | 29,695          |
|------|------------|------|------|------|--------------------|--------------------|-----------------------|-----------------|
| -2.1 | Classroom  | 6    | 6    | 2.4  | 36.0               | 86.4               | Longitude             | 43,17W          |
| -1.1 | Classroom  | 6    | 6    | 2.9  | 36.0               | 104.4              | Altitude              | 50m             |
| -1.2 | Classroom  | 4.4  | 6    | 2.9  | 26.4               | 76.6               | Pressure              | 101,22kPa       |
| 0.1  | Office     | 4.4  | 3.3  | 2.85 | 14.5               | 41.4               | Average Wind Velocity | 4,8m/s          |
| 0.2  | Laboratory | 5.7  | 6    | 2.85 | 34.2               | 97.5               | Wind Direction        | 150° (0 N; 50W) |
| 2.1  | Office     | 4.3  | 6    | 2.7  | 25.8               | 69.7               | Dry-Bulb Temperature  | 37,3°C          |
|      |            |      |      |      |                    |                    | Wet-Bulb Temperature  | 25,4°C          |
|      |            |      |      |      |                    |                    | Relative Humidity     | 79%             |

The total floor space of 170 m<sup>2</sup> and the average ceiling height of 2.76m was considered. The school has 5 floors covered by external walls with thermal transmission factor of 1,8 W/(m<sup>2</sup>K) and windows of 2,7 W/(m<sup>2</sup>K). The windows are obstructed mainly North and South; have no curtains. The following data was set within the HVAC Load Explorer, Table 4.

Table 4. Software extract "HvacLoadExplorer" - Layers of the outer wall.

| Layer         | Sp Heat<br>(Btu/(Lb.F)) | Conductivity<br>(Btu.in/(hr.ft <sup>2</sup> .F)) | Thickness (In) | Density (Lb/Ft <sup>3</sup> ) |
|---------------|-------------------------|--|----------------|-------------------------------|
| Plaster       | 0,64                    | 0,24   | 0,050          | 124,9                         |
| ceramic brick | 0,52                    | 0,22   | 0,12           | 99,9                          |
| Plaster       | 0,64                    | 0,24   | 0,050          | 124,9                         |

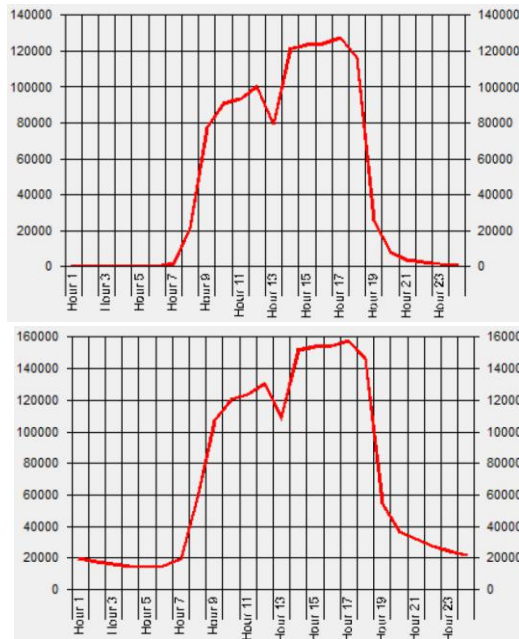
The ground floor has a constant temperature of 20°C. Solar installations on the terrace and a tree provide shade. Considering the air renewal of 30 m<sup>3</sup>/h per person, 110 students demand 3,300 m<sup>3</sup>/h. With a total volume of 469 m<sup>3</sup> in the spaces, air renewal is 7.0 l/h. The classrooms are occupied from 7h30-11h00 a.m. and 1h30-5h30 p.m. The two offices from 7h30-5h30 p.m. Considering an emission of 97 W per person, 110 people produce at a thermal load of 10.7

kW, lighting 15 W/m<sup>2</sup> in 170 m<sup>2</sup> producing 2.6 kW. Other devices produce 3.6 kW totalizing 17 kW. In Brazil the temperature is set between 18- 20 °C. The simulation was performed with two internal temperatures, 20 °C and 26 °C. The projected internal temperature of 26 °C. The high cooling load between the two temperatures stands out according to Table 5. The internal air temperature (Ti) is the most obvious indicator of thermal comfort [7].

Table 5 - Conditions of internal thermal comfort in relation to summer ambient temperatures [13].

| Internal Conditions  | Relative Humidity (%)     | 62    56    50    44    66    60    54    48    70    64    58    52 |    |      |    |      |      |      |      |      |    |      |    |  |  |
|----------------------|---------------------------|--|----|------|----|------|------|------|------|------|----|------|----|--|--|
|                      |                           | Wet-bulb Temperature (°C)  |    |      |    |      |      |      |      |      |    |      |    |  |  |
| External Temperature | Dry-bulb Temperature (°C) | 19,5   | 19 | 18,5 | 18 | 20,5 | 20   | 19,5 | 19   | 21,5 | 21 | 20,5 | 20 |  |  |
|                      | Dry-bulb Temperature (°C) | 24,5   | 25 | 25,5 | 26 | 25   | 25,5 | 26   | 26,5 | 25,5 | 26 | 26,5 | 27 |  |  |
|                      | Dry-bulb Temperature (°C) | 29   |    |      |    | 32   |      |      |      | 35   |    |      |    |  |  |

Figure 15 shows the daily thermal behaviour of the building in the worst-case scenario: Total cooling load (Btu/h) with Ti=26 °C and 20 °C during 24 h. summer. With an internal temperature of Ti = 26 °C, the maximum cooling load is 125,560.2 BTU/h (~36.8 kW; with Ti=20 °C, 157. 687.9 BTU/h (~46.2 kW). At the end, the total cooling load is compared with Ti = 26 °C and Ti=20 °C.



**Total Cooling (kW)**

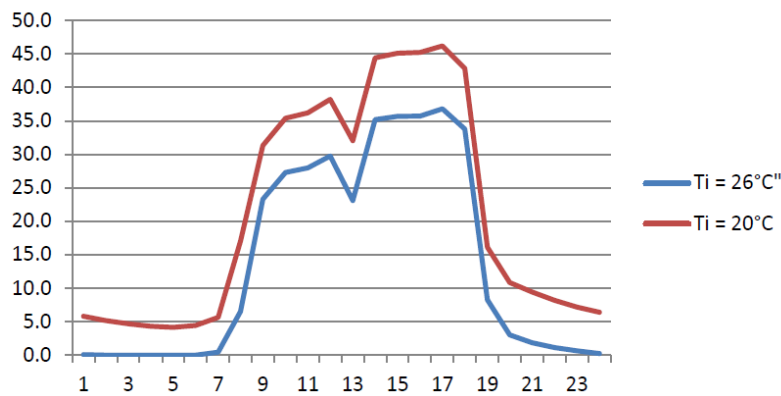


Fig.15. HVAC Load Explorer Output.

The Simulation for the different indoor air temperatures shows that the total cooling load increases up to 9.6 kW for a temperature variation  $\Delta T_i = 4^\circ\text{C}$ . Figure 16 shows the different thermal behavior of both indoor air temperatures during a summer day (worst-case scenario). Table 6 shows the results of the maximum cooling loads for the two ambient temperatures.

Table 6. Maximum cooling loads to the two ambient temperatures.

| Indoor Set Point Temperature<br>$T_i$ [ $^\circ\text{C}$ ] | Maximum Cooling Load [kW] | Specific Cooling Load [ $\text{kW}/\text{m}^2$ ] |
|--|---------------------------|--|
| 20   | 46.2                      | 272  |
| 26   | 36.8                      | 216  |

The applied system is like an auditorium at the University of Guaratinguetá [3]. It is a closed cycle process combining different subsystems as shown in Figure 13 and technical characteristics related to the simulated cooling load for a  $T_i=26^\circ\text{C}$ .

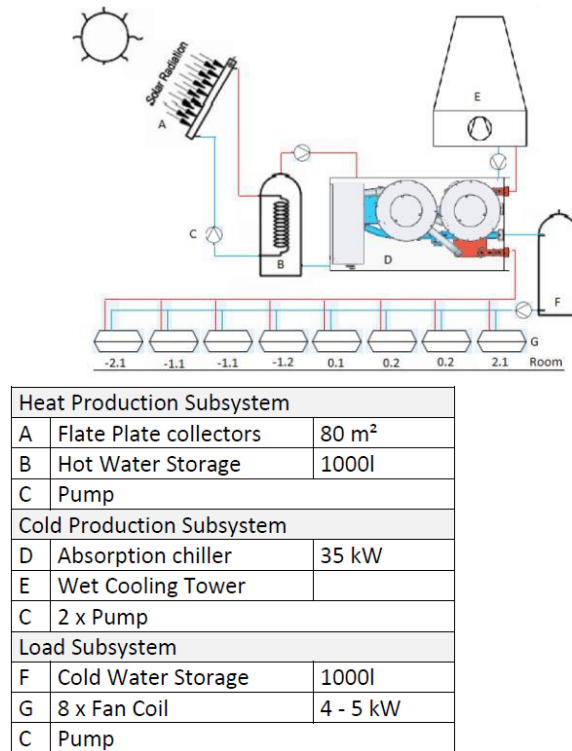


Fig.16. Schematic diagram of the system selected for the school and technical components of the different subsystems.

The heat production subsystems mainly consist of 80 m<sup>2</sup> solar thermal collector fields, which serve the hot water tank with inlet and outlet temperatures of 88 °C and 83 °C. The cold production system contains a 35-kW absorption chiller and a cooling tower. The thermal compressor of the absorption chiller is served by the heat provided by the hot

water tank. The load subsystem consists of a cold-water tank, the distribution system and 8 fan coil units. Figure 17 shows that cooling throughput meets demand during the day. At 12:00 the cooling capacity is almost twice as high as the demand. During the day the cooling load and solar gain occur simultaneously.

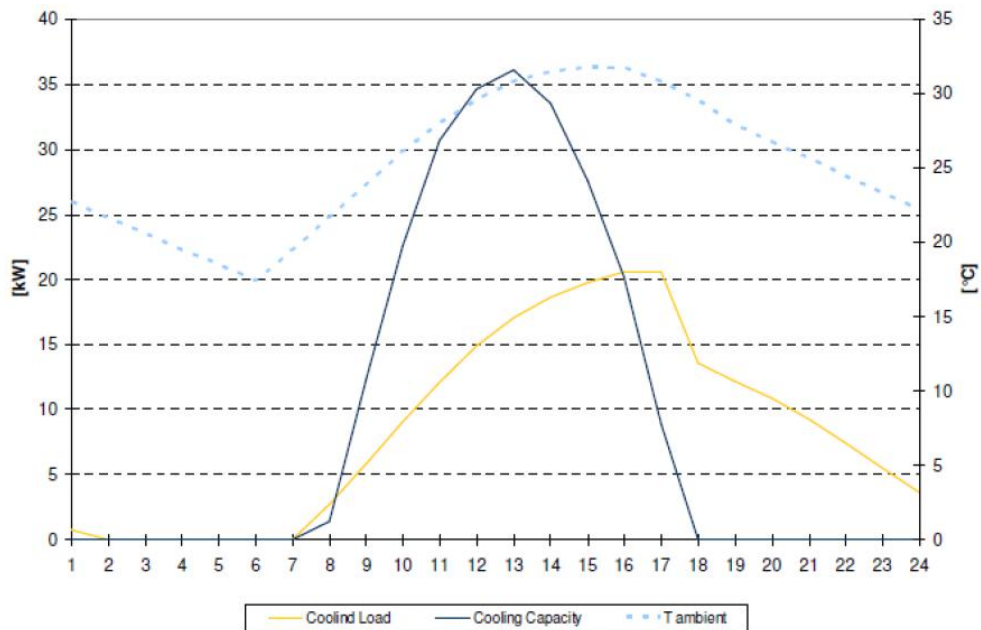


Fig.17. Expected correlation between cooling demand and yield in summer [3].

Figure 18 shows the total monthly demand for expected cooling and available thermal energy production (8760 h) in the case of the University of Guaratinguetá. The

solar yield was calculated with a constant average daily collector efficiency of 0.38 m<sup>2</sup> and a constant chiller COP of 0.7 [3].

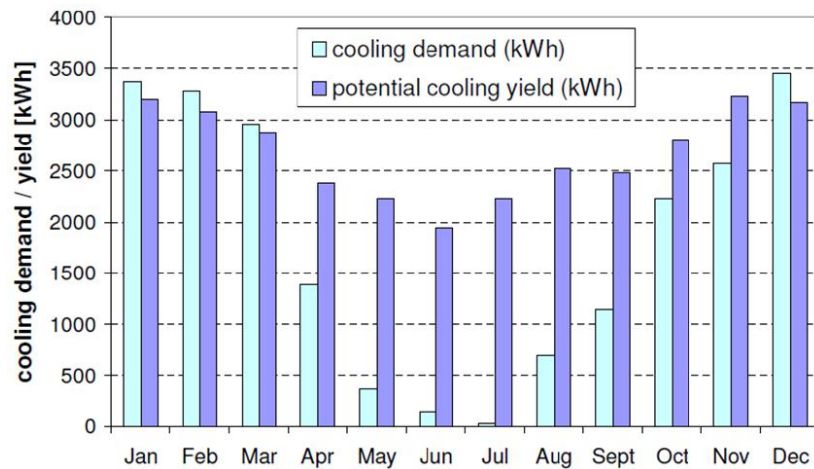


Fig.18. Total monthly cooling demand.

Predicted total monthly cooling demand and available yield of thermal energy (8760 h). Solar yield is calculated with a constant daily average collector efficiency of 0,38 m<sup>2</sup> collector array and a constant Chiller COP of 0,7 [4].

From table 7, the investment cost for the cooling system studied is R\$ 3,000/kW. The cooling system has been sized to cover a thermal load of 35 kW. R\$ 105,500 were the total investment costs. The return on investment is 15.8 years to 20 years.

Table 7. Electricity consumption and operating cost between the existing and the proposed system.

| Electricity Consumption & Operation Cost      |                       |                         |
|---|-----------------------|-------------------------|
| Component                                     | Solar Assisted System | Existing Cooling System |
| 4 x Water Pumps                               | 360 W                 |                         |
| Wet Cooling Tower Fan                         | 280 W                 |                         |
| 35 kW Absorption Chiller                      | 210 W                 |                         |
| 8 Fan Coil Units                              | 600 W                 |                         |
| 5 x Window Air-Conditioner                    |                       | 35.8 kW                 |
| Total   | 1450 W                | 35.8 kW                 |
| Total (1 Year)                                | 2152 kWh*             | 9577 kWh**              |
| Operation Cost (1 Year) by 0.898 R\$/kWh (RJ) | 1930 R\$              | 8600 R\$                |

To estimate emissions of CO<sub>2</sub> per kWh of cold produced, a conversion factor of 0.28 kg CO<sub>2</sub> per kWh of electricity was applied [1], Table 8.

Table 8. CO<sub>2</sub> savings per year calculated with conversion factor of 0.28 kg CO<sub>2</sub> per kWh of electricity.

| Electricity Consumption per Year (kWh) | CO <sub>2</sub> – Emissions (kg) |
|--|----------------------------------|
| Solar Assisted System                  | 603                              |
| Existing System                        | 2682                             |
| CO <sub>2</sub> Saving per Year        | 2079                             |

The substitution for a SCS system presents an environmental gain in the emission of CO<sub>2</sub> and elimination of greenhouse gases by ecological refrigerants. Water consumption of the wet cooling tower, in this case 50 l/d can be gotten by treated rainwater.

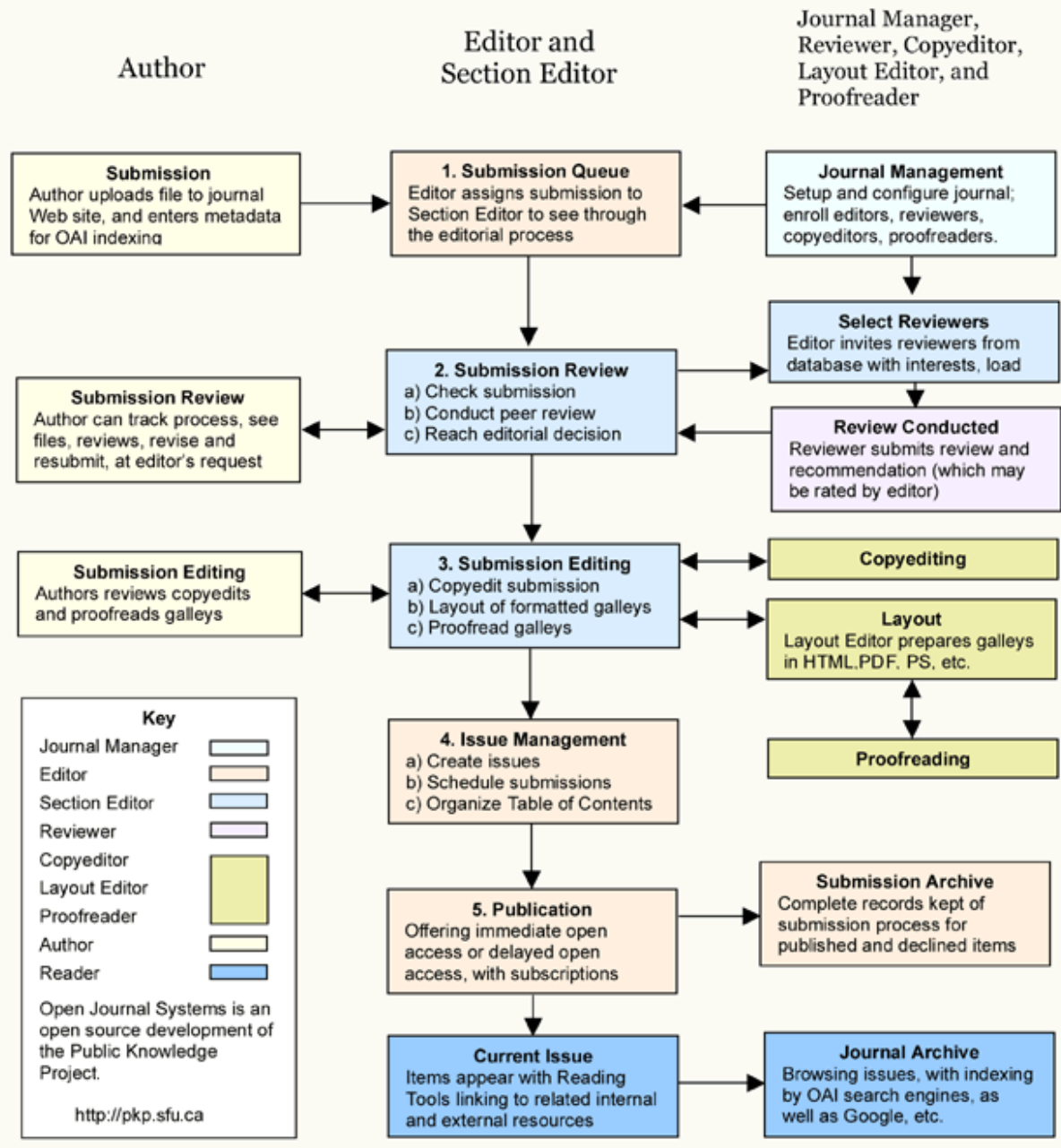
### III. RESULTS

The low operating cost of SCS compensates for investment in cooling buildings and contributes to reducing the consumption of electricity from non-renewable sources by increasing its share in the energy grid, encouraging the Government to practice sustainable public policies in accordance with ESG standards. In this way, SCS proves to be a sustainable energy alternative in providing environmental conditioning of buildings using solar energy. SCS and PV systems combined make up one of the furthered technologies, as the current trend is directed towards electrical supply in all facilities. Furthermore, the need of back systems is in high demand and will expand to general building technologies [15].

### REFERENCES

- [1] Fraunhofer Institute for Solar Energy Systems ISE. Solar Cooling in Brazil - Technology study. Freiburg, Germany, 2009.
- [2] IEA. Solar Heating & Cooling Program, Available online: <https://www.iea-shc.org/solar-academy>, Webinar, (accessed on 11/10/2023).
- [3] Felix, R. Technical and Economic Assessment of Solar-Assisted Air-Conditioning in Brazil. M.Sc. Thesis, PUC, Brazil, 2010.
- [4] Solair, Requirements on the design and configuration of small and medium sized solar air-conditioning applications – Guidelines, Available online: <https://www.solair-project.eu> (accessed on 11/10/2023).
- [5] Hans-Martin, H. TASK 38 - Solar Air Conditioning and Refrigeration, IEA SHC, Germany. 2012.
- [6] Douglas, R., Estudo Teórico da Otimização de Refrigeradores Térmicos por Adsorção. Ph.D., Thesis, UFPB, Brasil, 2008.
- [7] ASHRAE, ASHRAE Terminology of HVAC&R, Available online: <https://www.ashrae.org/technical-resources/authoring-tools/terminology> (accessed on 11/10/2023).
- [8] Uli, J.; Daniel, M., Keeping cool with the sun, *International Sustainable Energy Review*, 2012, Volume 6, p.p. 28-30.
- [9] Carrier United Technologies, Lithium Bromide Absorption Chiller, Technical Data Sheet 16JLR. T-16JL/R-0710-01(E)-CHK, 2023.
- [10] INMET, Dados meteorológicos médios, Brasil, Available online: <https://portal.inmet.gov.br>. (accessed on 11/10/2023).
- [11] Procel, Participação dos eletrodomésticos no consumo de eletricidade, Eletrobras, Brasil, 2023.
- [12] ABNT, Instalação de ar-condicionado – Sistemas centrais e unitários, Standard NBR16401, Brasil, 2008.
- [13] Arone, H. Análise computacional da demanda energética de climatização de edifício, B.Sc., Thesis, UNB, Brasil, 2005.
- [14] CEAT. HVAC Load Explorer, Available online: <https://hvac.okstate.edu/hvac-load-explorer.html> (accessed on 11/10/2023).
- [15] Wey, Z; Chengz, L; Lin, L; Hongxing, Y. Current status of research on optimum sizing of stand-alone hybrid solar-wind power generation systems; *Applied Energy*, V. 87, Issue 2, February 2010, pp. 380-389. <https://doi.org/10.1016/j.apenergy.2009.08.012>

# OJS Editorial and Publishing Process



~JJAERS Workflow~



## Important links:

### Paper Submission Link:

<https://ijaers.com/submit-paper/>

### Editorial Team:

<https://ijaers.com/editorial-board/>

### Peer Review Process:

<https://ijaers.com/peer-review-process/>

### Publication Ethics:

<https://ijaers.com/publication-ethics-and-publication-malpractice-statement/>

### Author Guidelines:

<https://ijaers.com/instruction-to-author/>

### Reviewer Guidelines:

<https://ijaers.com/review-guidelines/>

---

## Journal Indexed and Abstracted in:

- Qualis-CAPES (A2)-Brazil
- Normatiza (Under Review- Ref.020191511)
- NAAS Score: 3.18
- Bielefeld Academic Search Engine(BASE)
- Aalborg University Library (Denmark)
- WorldCat: The World's Largest Library Catalog
- Semantic Scholar
- J-Gate
- Open J-Gate
- CORE-The world's largest collection of open access research papers
- JURN
- Microsoft Academic Search
- Google Scholar
- Kopernio - powered by Web of Science
- Pol-Index
- PBN(Polish Scholarly Bibliography) Nauka Polaska
- Scilit, MDPI AG (Basel, Switzerland)
- Tyndale University College & Seminary
- Indiana Library WorldCat
- CrossRef DOI-10.22161/ijaers
- Neliti - Indonesia's Research Repository
- Journal TOC
- WIKI-CFP
- Scinapse- Academic Search Engine
- Mendeley-Reference Management Software & Researcher Network
- Dimensions.ai: Re-imagining discovery and access to research
- Index Copernicus Value(ICV): 81.49
- Citeseerx
- Massachusetts Institute of Technology (USA)
- Simpson University (USA)
- University of Louisville (USA)
- Biola University (USA)
- IE Library (Spain)
- Mount Saint Vincent University Library ( Halifax, Nova Scotia Canada)
- University Of Arizona (USA)
- INDIANA UNIVERSITY-PURDUE UNIVERSITY INDIANAPOLIS (USA)
- Roderic Bowen Library and Archives (United Kingdom)
- University Library of Skövde (Sweden)
- Indiana University East (campuslibrary (USA))
- Tilburg University (The Netherlands)
- Williams College (USA)
- University of Connecticut (USA)
- Brandeis University (USA)
- Tufts University (USA)
- Boston University (USA)
- McGill University (Canada)
- Northeastern University (USA)
- BibSonomy-The blue social bookmark and publication sharing system
- Slide Share
- Academia
- Archive
- Scribd
- ISRJIF
- Cite Factor
- SJIF-InnoSpace
- ISSUU
- Research Bib
- infobaseindex
- I2OR
- DRJI journal-repository



### AI Publication

International Journal of Advanced Engineering Research and Science (IJAERS)

104/108, Sector-10, Pratap Nagar, Jaipur, India